

---

Masters Theses

Student Theses and Dissertations

---

Fall 2010

## Modeling and analysis of high-speed sources and serial links for signal integrity

Siming Pan

Follow this and additional works at: [https://scholarsmine.mst.edu/masters\\_theses](https://scholarsmine.mst.edu/masters_theses)



Part of the [Electrical and Computer Engineering Commons](#)

Department:

---

### Recommended Citation

Pan, Siming, "Modeling and analysis of high-speed sources and serial links for signal integrity" (2010). *Masters Theses*. 6859.

[https://scholarsmine.mst.edu/masters\\_theses/6859](https://scholarsmine.mst.edu/masters_theses/6859)

This thesis is brought to you by Scholars' Mine, a service of the Missouri S&T Library and Learning Resources. This work is protected by U. S. Copyright Law. Unauthorized use including reproduction for redistribution requires the permission of the copyright holder. For more information, please contact [scholarsmine@mst.edu](mailto:scholarsmine@mst.edu).



MODELLING AND ANALYSIS OF HIGH-SPEED  
SOURCES AND SERIAL LINKS FOR SIGNAL INTEGRITY

by

SIMING PAN

A THESIS

Presented to the Faculty of the Graduate School of the  
MISSOURI UNIVERSITY OF SCIENCE AND TECHNOLOGY

In Partial Fulfillment of the Requirements for the Degree

MASTER OF SCIENCE IN ELECTRICAL ENGINEERING

2010

Approved by

Dr. Jun Fan, Advisor

Dr. James L. Drewniak

Dr. David J. Pommerenke

© 2010  
Siming Pan  
All Rights Reserved

## ABSTRACT

As the computer and electronics industry moves towards higher data rates, signal integrity and electromagnetic interference (EMI) problems always present challenges for designers for high-speed data communication systems. To characterize the entire link path between transmitters and receivers, accurate models for sources, passive link path (such as traces, vias, connectors, etc), and terminations should be built before simulations either in frequency or time domain. Due to the imperfection of model, data corrections are preferred before time-domain simulations to ensure stability. Moreover, data obtained from models should be compared with measurement results to judge the level of agreement for validations.

This thesis presents a new approach to model via structures to help design signal link path while maintaining a low insertion loss and minimizing crosstalk, borrowing the concepts from the transmission line theories. For the models of sources, a dipole model is proposed to represent integrated circuit (IC) radiation emissions while a circuit model for I/O current source is proposed for IC conductive emissions.

Passivity and causality are two important properties for passive networks. This thesis also presents detailed algorithm to check passivity and causality for networks with arbitrary port numbers. Data corrections in term of passivity and causality enforcement are applied based on matrix perturbation theory.

Last but not least, Feature Selective Validation (FSV) technique is expanded in this thesis to quantify the comparisons of data sets and provide quantitative standard for data optimization.

## ACKNOWLEDGMENTS

I would like to express my utmost gratitude to my advisor, Dr. Jun Fan, for his constant support and guidance throughout the course of my master's degree program.

I wish also to extend a special thanks to my committee members, Dr. James L. Drewniak and Dr. David J. Pommerenke, for their valuable input on my work.

I would also thank all the students and postdocs in the EMC Laboratory, those that have already left, those that are still here. A special thank goes to Hanfeng Wang, Jingook Kim, Songping Wu, Fan Zhou, Zhenwei Yu, Arun Chada, Ketan Shringarpure and Liehui Ren for valuable discussions, assistance and moral support.

Finally, I thank my parents, for their constant emotional support and encouragement. I wish to dedicate this work to them.

## TABLE OF CONTENTS

	Page
ABSTRACT.....	iii
ACKNOWLEDGMENTS .....	iv
LIST OF ILLUSTRATIONS.....	viii
LIST OF TABLES.....	xii
SECTION	
1. INTRODUCTION.....	1
2. MULTILAYERED VIA DESIGN AND OPTIMIZATION BASED ON EQUIVALENT TRANSMISSION LINE MODEL .....	3
2.1. INTRODUCTION OF VIA MODELING TECHNIQUES.....	3
2.2. EQUIVALENT COUPLED MTL MODEL FOR VIA STRUCTURES	5
2.2.1. Equivalent Transmission Line Model for Thru-hole Vias. ....	5
2.2.2. Transmission-Line Model for Vias Connected to Striplines.....	11
2.3. DESIGN CRITERIA FOR VARIOUS SIGNAL VIA TYPES BASED ON EQUIVALENT TRANSMISSION LINE MODEL .....	19
2.3.1. Single-ended Signal Via. ....	19
2.3.2. Differential-Signal Vias. ....	20
2.3.3. Multiple-Signal Vias. ....	22
2.4. VALIDATION OF EQUIVALENT TRANSMISSION LINE MODEL	24
2.5. DESIGN AND OPTIMIZATION OF DIFFERENTIAL SIGNAL VIAS IN MULTILAYERED PCB.....	33
2.5.1. Design Objective. ....	33
2.5.2. Design Guidelines for Differential Signal Vias for High-Speed Signal Transmission. ....	33
2.5.3. Example of Differential-Signal Via Structure Designed According To Guidelines Proposed in Section 2.5.2. ....	35
2.6. SUMMARY OF EQUIVALENT TRANSMISSION-LINE VIA MODEL .....	40
3. IC RADIATION AND CONDUCTIVE EMISSION MODELS.....	41
3.1. INTRODUCTION OF IC EMISSION MODELS.....	41

3.2. RADIATED EMISSION MODEL BASED ON TEM CELL MEASUREMENT .....	42
3.2.1. Dipole Model, Approach Details, and Key Issues. ....	42
3.2.2. Test Board Design.....	46
3.2.3. Measurement and Far Field Validations. ....	46
3.2.4. Incorporating Dipole Models into HFSS Modeling.....	53
3.3. CONDUCTED EMISSION MODEL FROM THE 1/150 OHM METHOD .....	56
3.3.1. Method Overview, Details, Key Issues. ....	56
3.3.2. Test Board Design. ....	69
3.3.3. Test Board Measurement.....	70
3.4. SUMMARY AND CONCLUSIONS .....	80
4. LINK PATH ANALYSIS .....	82
4.1. INTRODUCTION OF LINK PATH ANALYSIS .....	82
4.2. CASCADE OF S-PARAMETER BLOCKS .....	82
4.3. CAUSALITY CHECK AND ENFORCEMENT FOR S-PARAMETER DATA .....	86
4.4. PASSIVITY CHECK AND ENFORCEMENT FOR S-PARAMETER DATA .....	90
5. APPLICATIONS OF FEATURE SELECTIVE VALIDATION TECHNIQUE.....	95
5.1. APPLY FSV TO COMPARE DATA SETS WITHOUT STANDARD.....	95
5.1.1. Introduction. ....	95
5.1.2. Comparison Among Data Sets Without a Known Standard Reference.....	97
5.1.3. Applying FSV Techniques to Validate Different Via Modeling Approaches. ....	99
5.1.4 Summary. ....	104
5.2. APPLY FSV TO DATA OPTIMIZATION .....	104
5.2.1. Introduction. ....	104
5.2.2. Applying FSV as an Objective Function in Causality Enforcement. ....	105



5.2.3. Genetic Algorithm and Data Optimize for Causality Enforcement. ....	106
5.2.4. Summary. ....	110
BIBLIOGRAPHY.....	111
VITA.....	116

## LIST OF ILLUSTRATIONS

Figure	Page
2.1. Multiple-signal and ground vias in multilayered circuit board.....	6
2.2. Physics-based equivalent circuit model for multi-via structure between one parallel plane pair.....	7
2.3. Capacitance between via and plane in one cavity.....	9
2.4. Equivalent coupled MTL model for the multi-signal via structure between one parallel plane pair.....	10
2.5. Illustration of ports and voltages.....	13
2.6. Single-ended signal via connected to a single-ended stripline .....	14
2.7. Equivalent circuit model for the structure shown in Fig. 2.6.....	15
2.8. Simplified equivalent circuit model including the via stub effect for the structure shown in Fig. 2.6.....	16
2.9. Two differential-signal vias connected to two coupled striplines. ....	18
2.10. Equivalent differential-transmission-line model, including the via stub effect for the structure shown in Fig. 2.9.....	18
2.11. A simplified model using an equivalent transmission line with terminations for both single-ended and differential cases .....	19
2.12. Single-ended signal via with two ground vias .....	25
2.13. $ S_{11} $ of the via structures with trace connections shown in Fig. 2.12.....	26
2.14. $ S_{21} $ of the via structures with trace connections shown in Fig. 2.12.....	26
2.15. Geometry under study with different ground via patterns .....	27
2.16. Top view of the region within the dashed line in Fig. 2.15 .....	28
2.17. Magnitudes of NEXT and FEXT for the geometry shown in Fig. 2.16 .....	29
2.18. Phases of NEXT and FEXT for the geometry shown in Fig. 2.16 .....	30
2.19. Via structures with microstrip and edge-launch connectors .....	31
2.20. Real parts of characteristic impedance of via structures in Fig. 2.19, obtained from equivalent transmission line model. ....	32
2.21. TDR results for the three test via structures in Fig. 2.19.....	32
2.22. Demonstration of design guideline effectiveness .....	36
2.23. $ S_{dd11} $ of two differential-signal via structures shown in Fig. 2.22 .....	37

2.24. $ S_{dd21} $ of two differential-signal via structures shown in Fig. 2.22 .....	37
2.25. Real part of the equivalent differential $Z_0$ of two differential-signal via structures shown in Fig. 2.22 .....	38
2.26. Real part of the equivalent differential $Z_0$ of two differential-signal via structures shown in Fig. 2.22 .....	38
2.27. Setup for time-domain simulation of the differential-signal via structures shown in Fig. 2.22 .....	39
2.28. Time-domain simulation results for differential voltage at launch point .....	40
3.1. Typical dimensions of IC and its emission model using three equivalent dipole moments .....	43
3.2. Three TEM cell measurements necessary to extract the proposed IC emission model using (3.2) .....	44
3.3. TEM cell measurement with a hybrid.....	45
3.4. Test PCB geometry with a PLL chip .....	46
3.5. TEM cell terminations .....	47
3.6. Output power measured using a spectrum analyser for the test board placed in three different positions. ....	48
3.7. Equivalent dipole moments extracted from the TEM cell measurements for the PLL chip under test. ....	49
3.8. Far-field measurement in a semi anechoic chamber.....	50
3.9. Gain of the measurement setup and antenna factor. ....	51
3.10. Comparisons of the radiated fields from measurements with those calculated from the extract IC emission model. ....	52
3.11. Electric dipole approximated with a short wire antenna.....	54
3.12. Magnetic dipole approximated with a small loop antenna. ....	54
3.13. A combined source with one wire antenna and two loop antennas .....	55
3.14. Comparison of the radiated electric field results between analytical calculations and HFSS simulations. ....	56
3.15. Illustration of Power and GND current that needs to be measured .....	57
3.16. Configuration of 1- $\Omega$ Probe Method.....	58
3.17. Schematics of 1- $\Omega$ Probe in IEC 61967.....	59
3.18. Footprint of the 1- $\Omega$ probe with special circular-shape .....	59
3.19. Current probe with test board .....	60
3.20. Experimental setup for measuring S11 of the probe using a network analyzer.....	62

3.21. Experimental setup for measuring S21 of the probe using a trace and a network analyzer .....	62
3.22. Measured S11 result of the probe .....	63
3.23. Measured frequency response using a 50 Ohm trace.....	64
3.24. An equivalent circuit of the H-field probe.....	65
3.25. Comparison of S21 between “probe above trace” measured result and SPICE model result.....	65
3.26. Flow chart of the deconvolution function.....	67
3.27. Equivalent circuit model with cabling network.....	68
3.28. Thevenin equivalent source model for noise voltage at I/O pins.....	68
3.29. Schematics of the test board for IC conductive emission model and measurement .....	69
3.30. Layout of the test board for IC conductive emission model and measurement.....	70
3.31. Current probe used to measure IC conductive current.....	71
3.32. Transfer impedance of the current probe shown in Fig. 3.31 .....	71
3.33. Measurement results for the conductive current at GND pin using 1 Ohm probe and current probe .....	72
3.34. Equivalent circuit model for active probe.....	73
3.35. Setup of the calibration for active probe.....	73
3.36. Calibration factor (S21) of active probe .....	74
3.37. Setup of time-domain measurement of active probe .....	74
3.38. Comparison between measured signal from active probe and original signal.....	75
3.39. Comparison between measured signal from active probe and original signal.....	76
3.40. Comparison between measured signal from active probe and original signal in frequency domain.....	77
3.41. Voltage waveform at output pin with 3 different loads .....	78
3.42. Spectrum of the voltage at output pin with 3 different loads.....	78
3.43. Source voltage, resistance and inductance of the PLL IC .....	79
3.44. Comparison of I/O pin voltages from calculation of the model and measurement	80
4.1. Traditional methods for cascading S-parameter blocks.....	83
4.2. Cascading two n-port S-parameter blocks .....	85
4.3. Results comparison of cascaded methods.....	86

4.4. Configuration of a 4-port network representing a via structure in a printed circuit board .....	89
4.5. Time-domain responses of the original non-causal data and the enforced causal data. ....	90
4.6. Norm 2 of the S-parameter matrices before and after passivity enforcement .....	94
5.1. Differential via in multilayer structure with four ground via .....	99
5.2. $S_{DD21}$ .....	101
5.3. $S_{DD21}$ .....	103
5.4. The GA optimization procedures for causality enforcement.....	107
5.5. Deviation among individuals in each generation.....	108
5.6. Comparison between the original and the enforced imaginary parts of the S parameters. ....	109
5.7. FSV results of the original and the enforced data shown in Fig. 5.6.....	109

**LIST OF TABLES**

Table	Page
5.1. FSV results using average value as reference.....	100
5.2. FSV results using new weighted average value as reference .....	102

## 1. INTRODUCTION

Nowadays, the state of the art of the digital electronic system design pushes the high-speed system toward a high data rate, low voltage swing, and high density of interconnects. Some unwanted effects, previously negligible, start to play an important role in terms of quality of the waveform launched on the Print Circuit Board(PCB) interconnects. Therefore, to model the performance of the signal path from transmitter to receiver is becoming more and more difficult. Via structures are necessary in PCBs and packages to connect traces and planes in different layers. A via always generates mismatch in the signal link path causing discontinuity between via and trace. Furthermore, strong crosstalk may occur in adjacent signal vias as high-speed current flowing on the vertical via barrel excites propagating parallel plane modes of a power/ground pair. Thus, the performance of via structures can significantly affect the signal and power integrity for high-speed circuits.

In the other hand, Integrated circuit (IC) devices are the ultimate noise sources that contribute to many component- and system-level electromagnetic compatibility (EMC) issues, which become increasingly critical for high-speed digital circuit designs due to the constant increase of clock speeds, power consumption, circuit density and complexity. Thus, the interest in evaluating IC modeling of the IC sources in both radiation emission and conductive emissions has grown in recent years since the reduction of the electromagnetic emissions (EME) at IC level brings to a mitigation of system level emissions making needless expensive filtering and shielding components.

Either models for active sources or passive signal links cannot be perfectly accurate. Problems such as instability always appear in time-domain simulation when the models violate causality and passivity. Thus, causality and passivity checks are important before the models are applied in simulations. Efficient algorithms for causality and passivity enforcement are proposed based on matrix perturbation theory.

To validate the model, multiple results from other models and measurement are desired for comparison. However, result from each approach has its own imperfection compared to the real word situations, so it is difficult to compare the accuracy of each method by analyzing the theoretical processes. An improved Feature Selective

Validation (FSV) procedure is developed to validate different uncertain approaches without knowing a standard reference. Moreover, the application of the FSV technique is extended to determine objective functions in the data optimization process to correct the original model.



## 2. MULTILAYERED VIA DESIGN AND OPTIMIZATION BASED ON EQUIVALENT TRANSMISSION LINE MODEL

### 2.1. INTRODUCTION OF VIA MODELING TECHNIQUES

Via structures are important portions in the signal path to connect traces and planes in different layers. A via always generates mismatch in the signal link path causing discontinuity between via and trace. Various methods of modeling the vias structures in the high-speed link paths for better signal integrity has been extensively studied before.

In past years, quasi-static approaches have been commonly used to analyze via-plane interactions [1]-[4], as the evanescent waves are localized near the via as capacitive energy. A simple  $\pi$ -type RLC circuit model was built using numerical or analytical approaches. However, when high-speed current flows along the vertical via, not only evanescent waves but also propagating parallel plane modes are excited. Thus, vias through a plain pair may be difficult to deal with using quasi-static numerical computation.

Full-wave numerical computation is also effective to model vias with small cavities, such as finite differences time domain [5] and method of moments [6]. Rigorous three-dimensional electromagnetic modelling of each full-wave method requires inclusion of the complete power and ground planes to in the computational domain, and thus consumes significant computational resources.

At present, there are two primary approaches to deal with vias in a plane pair. The Foldy-Lax multiple scattering method is one algorithm proposed for analysis of via arrays in a plane pair [7]-[9]. The method adopts magnetic frill current as the source. The via barrel is modeled as a perfect electric conductor (PEC) boundary, and Green's function between two PEC planes is used to calculate the fields in the plane pair. Adoption of the addition theorem of cylindrical waves permits consideration of the multiple scattering effects among vias. On the other hand, a physics-based circuit model has been proposed to characterize the via behaviors in circuit boards and packages [10]-[13]. Since the via is usually electrically short, the via can be modeled as a lumped circuit with two via-plane capacitances at the ends of the via barrel. The impedance of the parallel plane,  $Z_{pp}$ , is used to represent propagating parallel plane modes.

Although via performance can be characterized by many existing via modeling techniques, no existing approach provides a simple straightforward way to design and optimize via structures in PCBs. This paper proposes an equivalent coupled multiconductor transmission line (MTL) model to characterize multi-via structures. It borrows the well-known concepts such as characteristic impedances and propagation constants from MTL theory for via design and optimization. In addition, it derives the per-unit-length parameters of the equivalent transmission line model based on geometry. Use of this parameters may provide physical insights to associate via behaviour with practical geometry.

The section is organized as follow: Section 2.2.2 first discusses an equivalent MTL line model to approximate multiple-signal via structures; it then derives the analytical formulas for the per-unit-length parameters. It also extends the equivalent transmission-line model for the via structures connected to striplines based on the modal decomposition approach inside a parallel plane cavity.

Section 2.2.3 discusses design criteria for various signal via types using the equivalent transmission line model. For single-ended and differential-signal vias, the easy-to-understand transmission line parameters can be adopted to minimize both dielectric loss and mismatch at via-trace junctions. This section also uses MTL to analyze crosstalk among multiple-signal vias in a via array.

Section 2.2.4 provides three examples to validate the equivalent transmission line model. The first example compares results from the transmission line model with those from a full-wave simulation for a single-ended-signal via transition from microstrip to stripline in a multilayered circuit board. The second example investigates crosstalk among via arrays in a complex geometry. It validates the equivalent MTL model comparing the crosstalk value with the original physics-based equivalent circuit model. The third example compares characteristic impedances obtained from the equivalent transmission line and time-domain reflectometry (TDR) measurements for three test coupons to validate the concept of via impedance.

Section 2.2.5 discusses the process of optimizing differential-signal vias in a multilayered PCB using the equivalent transmission line model. To demonstrate the

competence of the design guidelines proposed here, it provides simulation results from both the time and frequency domains for a practical design example.

## **2.2. EQUIVALENT COUPLED MTL MODEL FOR VIA STRUCTURES**

**2.2.1. Equivalent Transmission Line Model for Thru-hole Vias.** Figure 2.1 shows a typical via structure including multiple signal and ground vias in a multilayered circuit board. When a current flows on the vertical via barrel, both the ground vias and the multilayer parallel planes provide its return path. Thus, the transverse magnetic modes along the vertical via direction can propagate between the parallel planes. The shunt capacitances between the signal via and each plane should be taken into account as well, therefore, the via structure strictly speaking is not a transmission line, and the per-unit-length parameters cannot be directly extracted from two-dimensional cross-sectional analytical tools.

Figure 2.1 shows a typical via structure including multiple signal and ground vias in a multilayered circuit board. When a current flows on the vertical via barrel, both the ground vias and the multilayer parallel planes provide its return path. Thus, the transverse magnetic modes along the vertical via direction can propagate between the parallel planes. The shunt capacitances between the signal via and each plane should be taken into account as well, therefore, the via structure strictly speaking is not a transmission line, and the per-unit-length parameters cannot be directly extracted from two-dimensional cross-sectional analytical tools.

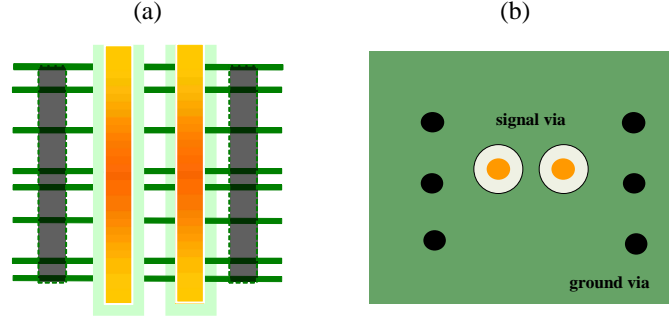


Fig. 2.1 Multiple-signal and ground vias in multilayered circuit board.

(a) Side view and (b) Top view.

Figure 2.2 shows a physics-based circuit model for the via structure, including the fields between the planes and the capacitive coupling between the via and the planes. The fields between two parallel planes are modeled as an impedance matrix,  $\mathbf{Z}_{pp}$ , which has been extensively studied in the previous publications [14]-[16]. When the spacing between two metal planes is less than a half wavelength at the highest frequency of interest, only the electric field in the  $Z$  direction and the magnetic field in the  $\Phi$  direction have nonzero components [17]. Neither of those fields has any variations in the  $Z$  direction. Thus, the impedance between port  $i$  and  $j$  in a parallel-plane pair can be defined as

$$\mathbf{Z}_{pp}(i, j) = \frac{V_i}{I_j} = -\frac{h \int_{l_i} E_z dl_i}{l_i \int_{l_j} H_\phi dl_j} \quad (2.1)$$

where  $l_{i(j)}$  denotes the circumference of port  $i$  ( $j$ ) and  $h$  denotes the height of the parallel-plane pair.

For a rectangular plane pair, the impedance matrix  $\mathbf{Z}_{pp}$  can be obtained by solving the two-dimensional Helmholtz equation with perfect magnetic boundary condition on the periphery of the cavity [13]:

$$Z_{pp}(i, j) = \frac{j\omega\mu h}{ab} \sum_{m=0}^{\infty} \sum_{n=0}^{\infty} \frac{C_m \cdot C_n \cdot f_{boundary} \cdot f_{port}}{\left(\frac{m\pi}{a}\right)^2 + \left(\frac{n\pi}{b}\right)^2 - k^2} \quad (2.2)$$

where  $\omega$  is the angular frequency,  $\mu$  is the permeability of the dielectric material,  $h$  is the plane height,  $a$  and  $b$  are plane dimensions and  $k$  is complex waveguide number. In addition,

$C_m$  and  $C_n$  are equal to 1 when  $m$  and  $n$  are equal to 0; they are equal to  $\sqrt{2}$  otherwise. The term  $f_{boundary}$  and  $f_{port}$  in equation (2.2) can be represented as:

$$f_{boundary} = \cos\left(\frac{m\pi x_i}{a}\right) \cos\left(\frac{n\pi y_i}{b}\right) \cos\left(\frac{m\pi x_j}{a}\right) \cos\left(\frac{n\pi y_j}{b}\right)$$

$$f_{port} = \sin c\left(\frac{m\pi L_{xi}}{2a}\right) \sin c\left(\frac{n\pi L_{yi}}{2b}\right) \sin c\left(\frac{m\pi L_{xj}}{2a}\right) \sin c\left(\frac{n\pi L_{yj}}{2b}\right)$$

In both of the latter expressions,  $x_i$ ,  $y_i$ ,  $x_j$ , and  $y_j$  are port locations,  $L_{xi}$ ,  $L_{yi}$ ,  $L_{xj}$ , and  $L_{yj}$  are port dimensions.

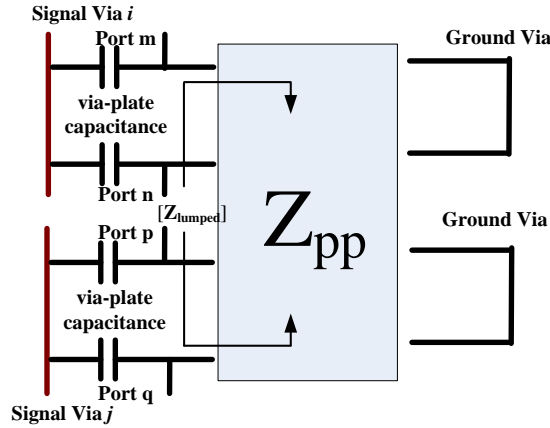


Fig. 2.2 Physics-based equivalent circuit model for multi-via structure between one parallel plane pair.

To derive the parameters of the equivalent MTL for a multi-via structure, the impedance matrix  $Z_{lumped}$  is defined as input impedance looking into the parallel planes at

all of the signal via ports, with shorting vias at all ground via ports. For simplicity, all the ports for signal vias are numbered in front of those for ground vias in the parallel plane admittance matrix  $\mathbf{Y}_{pp}$ . Thus, this matrix can be written as

$$\mathbf{Y}_{pp} = \begin{bmatrix} \left[ \mathbf{Y}_{pp\_ss} \right]_{m \times m} & \left[ \mathbf{Y}_{pp\_sg} \right]_{m \times n} \\ \left[ \mathbf{Y}_{pp\_gs} \right]_{n \times m} & \left[ \mathbf{Y}_{pp\_gg} \right]_{n \times n} \end{bmatrix} \quad (2.3)$$

where  $m$  is the number of signal vias,  $n$  is the number of ground vias and

$$\mathbf{Y}_{pp} = \mathbf{Z}_{pp}^{-1} \quad (2.4)$$

Thus, the impedance matrix can be expressed as

$$\mathbf{Z}_{lumped} = \mathbf{Y}_{pp\_ss}^{-1} \quad (2.5)$$

The via-plate capacitance can be divided into two parts: the coaxial capacitance  $C_a$  and the barrel-plate capacitance  $C_b$ , as shown in Fig. 2.3. The coaxial capacitance is due to the transverse electromagnetic (TEM) mode when the finite plate thickness is considered. The barrel-plate capacitance is caused by high-order parallel plate  $\text{TM}_z$  modes. The analytical expressions of both coaxial and barrel-plate capacitance are provided in [18]. The capacitive couplings among various vias can usually be disregarded. Thus, the admittance matrix  $\mathbf{Y}_{lumped}$  for multiple-signal vias has only diagonal terms, with

$$\mathbf{Y}_{lumped} = \begin{bmatrix} 2j\omega(C_a + C_b) & & 0 \\ & \ddots & \\ 0 & & 2j\omega(C_a + C_b) \end{bmatrix}_{m \times m} \quad (2.6)$$

Both the impedance matrix and the admittance matrix are physically distributed parameters along the via barrel, because they are functions of via length  $h$ . The per-unit-length impedance  $\mathbf{Z}$  and admittance matrices  $\mathbf{Y}$  of the equivalent multiconductor transmission line shown in Fig. 2.4 can be calculated, respectively, as

$$\begin{aligned} \mathbf{Z} &= \frac{d\mathbf{Z}_{lumped}}{dh} \\ \mathbf{Y} &= \frac{d\mathbf{Y}_{lumped}}{dh} \end{aligned} \quad (2.7)$$

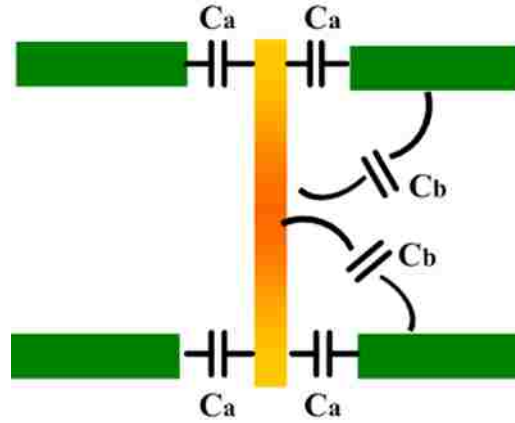


Fig. 2.3 Capacitance between via and plane in one cavity.

Equations (2.1), (2.4) and (2.5) indicate that the impedance matrix is approximately proportional to the via length. Thus, the per-unit-length impedance has almost no variation along the via length.

Although the per-unit-length admittance is a function of the via length, the variation along via length is small because the via barrel is coupled to both the top and bottom planes. Thus, the admittance can still be considered approximately constant along the via barrel.

So (2.6) can be simplified as

$$\mathbf{Z} = \frac{\mathbf{Z}_{\text{lumped}}}{h} \quad (2.8)$$

$$\mathbf{Y} \approx \frac{\mathbf{Y}_{\text{lumped}}}{h}$$

The per-unit-length impedance can be also expressed in terms of per-unit-length resistance  $\mathbf{R}$  and inductance  $\mathbf{L}$  as

$$\mathbf{R} = \text{Re}(\mathbf{Z}) \quad (2.9)$$

$$\mathbf{L} = \text{Im}(\mathbf{Z}) / 2\pi f$$

The per-unit-length resistance represents the loss between the parallel plane, including both the dielectric and skin-effect loss. The per-unit-length inductance represents electromagnetic wave coupling among all the vias.

As long as the via length is electrically small, the MTL model in Fig. 2.3 and the physics-based circuit model in Fig. 2.4 are equivalent because the magnitude of impedance matrix is much smaller than the magnitude of the admittance matrix. In reality, vias behave as a slow-mode structure because the equivalent phase velocity of wave propagation is slower than the speed of light in that medium [19]. The slow-mode property of vias decreases the frequency range over which the physics-based circuit model is valid.

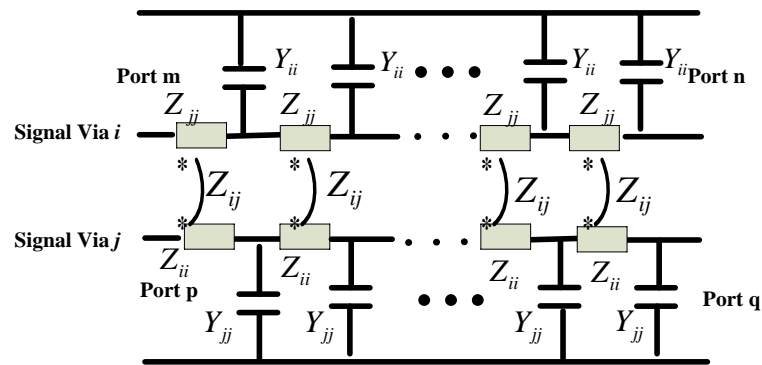


Fig. 2.4 Equivalent coupled MTL model for the multi-signal via structure between one parallel plane pair.

For multilayer via structures, the equivalent MTL for the portion between each plane pair can be connected, as noted above. However, as long as a via is electrically short, discontinuities at every layer interface can be neglected.



Thus, a multilayer via structure can be considered a single MTL when the via length is electrically small, with

$$\begin{aligned} \mathbf{Z} &= \sum \mathbf{Z}_{\text{lumped}} / h_{\text{total}} \\ \mathbf{Y} &= \sum \mathbf{Y}_{\text{lumped}} / h_{\text{total}} \end{aligned} \quad (2.10)$$

where  $\sum \mathbf{Z}_{\text{lumped}}$  is the sum of the input impedances at signal via ports in every layer,  $\sum \mathbf{Y}_{\text{lumped}}$  is the sum of all the corresponding admittance, and  $h_{\text{total}}$  is the total height of the multilayered circuit board.

**2.2.2. Transmission-Line Model for Vias Connected to Striplines.** The equivalent transmission line model for vias can be extended to include traces connecting vias for single-end and differential signals. Figure 2.5 provides a cross-sectional view of a typical geometry with coupled striplines connected to signal vias. The thickness of the strip conductors is assumed to be negligible. The distance from the strip conductors to the top and bottom planes respectively, is  $h_1$  and  $h_2$ . When the top and bottom planes are at the same potential level, only the TEM waves can propagate in the striplines inside of the plane pair, and the striplines can be modeled as a coupled MTL. The TEM waves propagated along striplines are denoted stripline mode waves and shown as Fig. 2.5(a).

As noted above, voltages and currents can be defined at the parallel-plane ports between two planes, as shown in Fig. 2.5(b). These parallel-plane voltages and currents are related by parallel-plane impedance defined in (2.1).

The stripline and parallel-plane modes can be demonstrated to be orthogonal. In other words, the physical voltages and currents defined in Fig. 2.5(c) can be expressed as the supposition of the stripline mode and the parallel-plane mode voltages and currents:

$$\begin{bmatrix} V_{st1} \\ \vdots \\ V_{st\frac{n}{2}} \\ V_{sb1} \\ \vdots \\ V_{sb\frac{n}{2}} \end{bmatrix} = [T_v] \cdot \begin{bmatrix} V_{stripl} \\ \vdots \\ V_{strip\frac{n}{2}} \\ V_{pp1} \\ \vdots \\ V_{pp\frac{n}{2}} \end{bmatrix}, \quad (2.11)$$

and

$$\begin{bmatrix} I_{st1} \\ \vdots \\ I_{st\frac{n}{2}} \\ I_{sb1} \\ \vdots \\ I_{sb\frac{n}{2}} \end{bmatrix} = [T_i] \cdot \begin{bmatrix} I_{strip1} \\ \vdots \\ I_{strip\frac{n}{2}} \\ I_{pp1} \\ \vdots \\ I_{pp\frac{n}{2}} \end{bmatrix}, \quad (2.12)$$

where

$$[T_v] = \begin{bmatrix} 1 & \cdots & 0 & k & \cdots & 0 \\ \vdots & \ddots & \vdots & \vdots & \ddots & \vdots \\ 0 & \cdots & 1 & 0 & \cdots & k \\ 1 & \cdots & 0 & 1+k & \cdots & 0 \\ \vdots & \ddots & \vdots & \vdots & \ddots & \vdots \\ 0 & \cdots & 1 & 0 & \cdots & 1+k \end{bmatrix},$$

$$[T_i] = \begin{bmatrix} 1+k & \cdots & 0 & -1 & \cdots & 0 \\ \vdots & \ddots & \vdots & \vdots & \ddots & \vdots \\ 0 & \cdots & 1+k & 0 & \cdots & -1 \\ -k & \cdots & 0 & 1 & \cdots & 0 \\ \vdots & \ddots & \vdots & \vdots & \ddots & \vdots \\ 0 & \cdots & -k & 0 & \cdots & 1 \end{bmatrix},$$

and,  $k = \frac{-h_1}{h_1 + h_2}$ .

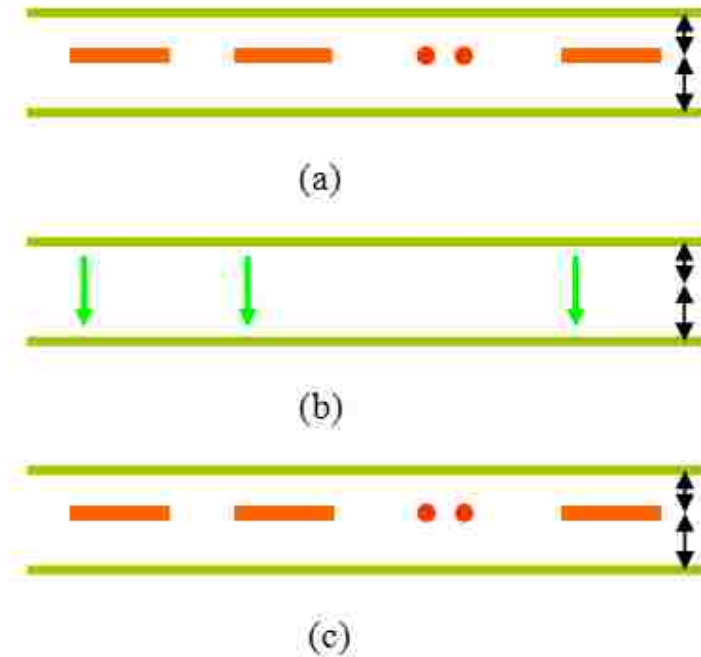


Fig. 2.5. Illustration of ports and voltages for (a) stripline mode, (b) parallel-plane mode, and (c) physical geometry.

For single-ended signal transition from a signal via to a stripling between a pair of parallel planes, as shown in Fig. 2.6, (2.11) and (2.12) can be reduced to the following equation set:

$$\begin{aligned}
 V_{st} &= V_{strip} - k_1 \cdot V_{pp} \\
 V_{sb} &= V_{strip} + k_2 \cdot V_{pp} \\
 I_{st} &= k_1 I_{strip} + I_{pp} \\
 I_{sb} &= k_2 I_{strip} - I_{pp}
 \end{aligned}
 \tag{2.13}$$

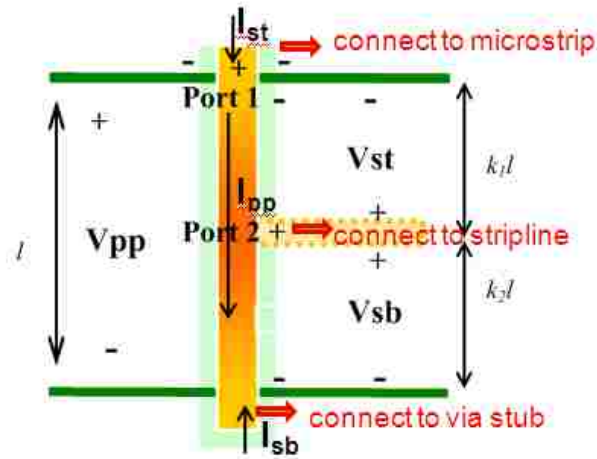


Fig. 2.6. Single-ended signal via connected to a single-ended stripline.

The equivalent circuit model for the structure shown in Fig. 2.6 is illustrated in Fig. 2.7. All the ports are clearly defined in Fig. 2.6. The signal via inside the cavity is first modelled as an equivalent transmission line, with per-unit-length impedance  $Z$  and admittance  $Y$  obtained from equation (2.8). Considering modal decomposition for a via-stripline connection, two additional current sources are added to the model so that all the voltages and currents can satisfy equation (2.13).

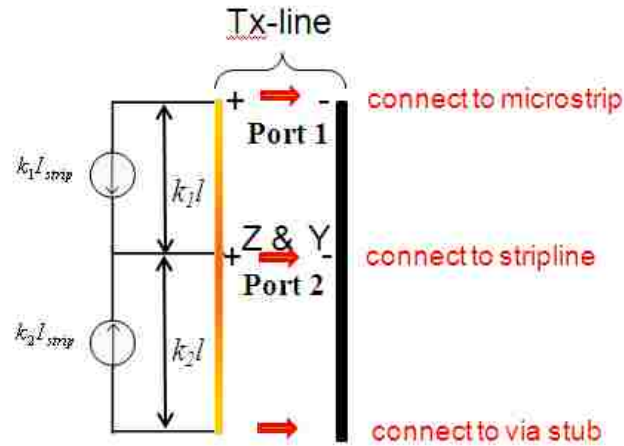


Fig. 2.7. Equivalent circuit model for the structure shown in Fig. 2.6.

The circuit model in Fig. 2.7 can be further simplified to the circuit model in Fig. 2.8 by converting the current sources to two parallel impedances and treating the via stub underneath Port 2 as a load,  $Z_{load}$ . The value of the load is the input impedance of the via stub at Port 2, which can be calculated using the analytical expression given in [24]. The analytical expressions of two parallel impedances  $Z_1$  and  $Z_2$  in Fig. 2.8 are written as

$$\begin{aligned} Z_1 &= \frac{k_1 Z_l (Z_c + k_1 (Z_{load} // (k_1 l / Y)))}{k_2 ((Z_{load} // (k_1 l / Y)) + k_2 Z_l)} \\ Z_2 &= \frac{-k_2 Z_l (Z_c + k_1 (Z_{load} // (k_1 l / Y)))}{k_1 ((Z_{load} // (k_1 l / Y)) + k_2 Z_l)} \end{aligned} \quad (2.14)$$

where  $Z_c$  is the characteristic impedance of the stripline.

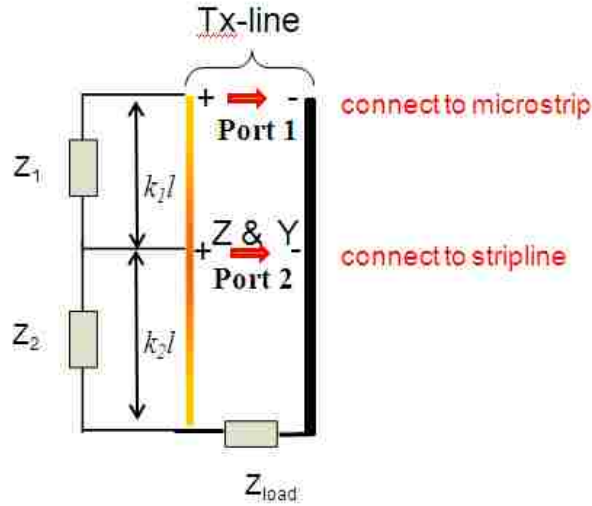


Fig. 2.8. Simplified equivalent circuit model including the via stub effect for the structure shown in Fig. 2.6.

Figure 2.9 shows the geometry of the differential case considered here with a differential signal flowing through two symmetric signal vias to two coupled striplines. For differential signals, equations (2.11) and (2.12) become

$$\begin{bmatrix} V_{st1} \\ V_{st2} \\ V_{sb1} \\ V_{sb2} \end{bmatrix} = \begin{bmatrix} 1 & 0 & -k_1 & 0 \\ 0 & 1 & 0 & -k_1 \\ 1 & 0 & k_2 & 0 \\ 0 & 1 & 0 & k_2 \end{bmatrix} \cdot \begin{bmatrix} V_{strip1} \\ V_{strip2} \\ V_{pp1} \\ V_{pp2} \end{bmatrix} \quad (2.15)$$

$$\begin{bmatrix} I_{st1} \\ I_{st2} \\ I_{sb1} \\ I_{sb2} \end{bmatrix} = \begin{bmatrix} k_2 & 0 & -1 & 0 \\ 0 & k_2 & 0 & -1 \\ k_1 & 0 & 1 & 0 \\ 0 & k_1 & 0 & 1 \end{bmatrix} \cdot \begin{bmatrix} I_{strip1} \\ I_{strip2} \\ I_{pp1} \\ I_{pp2} \end{bmatrix} \quad (2.16)$$

For differential signals of balanced signal paths,

$$I_{pp1} = -I_{pp2} \quad (2.17)$$

Similar to the single-ended case, the equivalent circuit model for the geometry shown in Fig. 2.9 is developed as shown in Fig. 2.10. Only the differential mode is considered in deriving the circuit parameters.

The differential-mode input impedance  $Z_{\text{load\_diff}}$  at the via stubs, if any, beneath the bottom plane can also be obtained using the expression given in [24]. Similar to the single-ended case, in Fig. 2.11, the equivalent circuit for the differential case is first obtained by extracting an equivalent differential transmission-line model with per-unit-length impedance matrix  $\mathbf{Z}$  and admittance matrix  $\mathbf{Y}$  from [8]. To enforce the relationship between voltage and current at each port for modal decomposition, additional impedances must be added to both the self and the mutual term of per-unit-length impedance matrix.

In Fig. 2.12, the impedances  $Z_{\text{up}}$  and  $Z_{\text{down}}$  paralleled to the self terms of per-unit-length impedance are converted from the extra current sources, as in the single-ended model shown in Fig. 2.7. These impedances can be written as

$$\begin{aligned} Z_{\text{up}} &= \frac{k_1 Z_{11} l (Z_{dd} + k_1 ((Z_{\text{load\_diff}} / 2) // (k_1 l / Y_{11})))}{k_2 ((Z_{\text{load\_diff}} / 2) // (k_1 l / Y_{11})) + k_2 Z_{11} l} \\ Z_{\text{down}} &= \frac{-k_2 Z_{11} l (Z_{dd} + k_1 ((Z_{\text{load\_diff}} / 2) // (k_1 l / Y_{11})))}{k_1 ((Z_{\text{load\_diff}} / 2) // (k_1 l / Y_{11})) + k_2 Z_{11} l} \end{aligned} \quad (2.18)$$

where  $Z_{dd}$  is the differential-mode characteristic impedance of the coupled striplines.

To satisfy equations (2.15) and (2.16), the mutual impedance of the via above and below the stripline changes from  $Z_{12}$  to  $Z_{\text{up}12}$  and  $Z_{\text{bottom}12}$  respectively, with

$$\begin{aligned} Z_{\text{up}12} &= \frac{-k_1 Z_{12} l (Z_{dd} + k_1 ((Z_{\text{load\_diff}} / 2) // (k_1 l / Y_{11})))}{1 - k_2 ((Z_{\text{load\_diff}} / 2) // (k_1 l / Y_{11})) + k_2 Z_{11} l} \\ Z_{\text{bottom}12} &= \frac{Z_{12} l (-Z_{dd} + k_1 ((Z_{\text{load\_diff}} / 2) // (k_2 l / Y_{11})))}{-Z_{dd} + k_1 (2((Z_{\text{load\_diff}} / 2) // (k_2 l / Y_{11})) + k_2 Z_{11} l)} \end{aligned} \quad (2.19)$$

The per-unit-length self-impedance of the via remains the same as the diagonal terms in the impedance matrix  $\mathbf{Z}$ . Differential port 2 is assumed to be matched with differential striplines. The equivalent transmission line model shown in Fig. 2.12 satisfies equation (2.8), (2.15), (2.16), and (2.17).

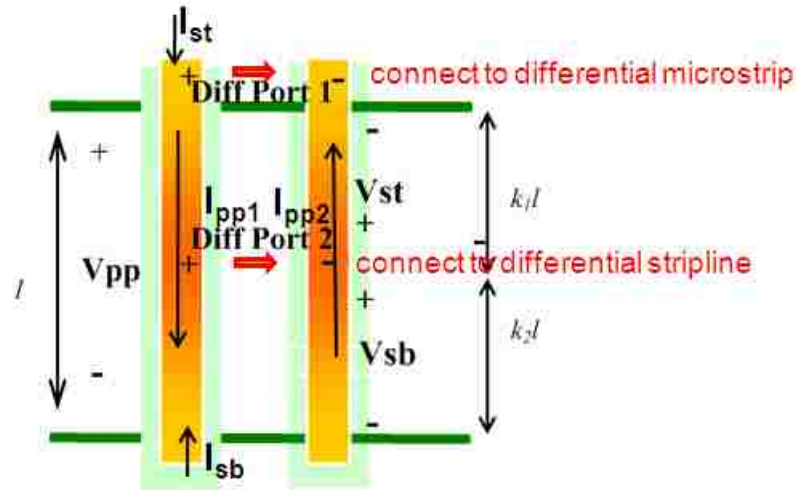


Fig. 2.9. Two differential-signal vias connected to two coupled striplines.

For both the single-ended and the differential cases, the equivalent circuit models developed above can be further simplified using an equivalent transmission line terminated with a load, as shown in Fig. 2.10.

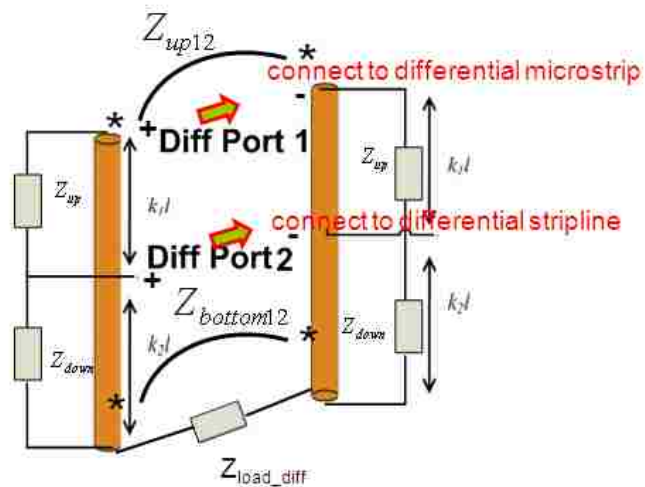


Fig. 2.10. Equivalent differential-transmission-line model, including the via stub effect for the structure shown in Fig. 2.9. The reference plane is omitted.



For the single-ended case shown in Fig. 2.8, the per-unit-length impedance  $Z'$  and admittance  $Y'$  in the simplified model in Fig. 2.13 can be calculated as

$$\begin{aligned} Z' &= Z // (Z_1 / (k_1 l)) \\ Y' &= Y \end{aligned} \quad (2.20)$$

The value of  $Z_{load\_port2}$  in Fig. 2.11 can be calculated from the circuit parameters in Fig. 2.8 as

$$Z_{load\_port2} = (Z_2 // Z k_2 l + Z_{load} // (k_2 l / Y)) \quad (2.21)$$

Similar derivations can be applied for the via-stripline model of differential case in Fig. 2.10:

$$Z_{diff\_load\_port2} = 2(Z_{down} // Z_{11} k_2 l - Z_{down12} + (Z_{load\_diff} / 2) // (k_2 l / Y_{11})) \quad (2.22)$$



Fig. 2.11. A simplified model using an equivalent transmission line with terminations for both single-ended and differential cases. For differential cases, the reference plane is omitted

## 2.3. DESIGN CRITERIA FOR VARIOUS SIGNAL VIA TYPES BASED ON EQUIVALENT TRANSMISSION LINE MODEL

**2.3.1. Single-ended Signal Via.** Smooth transitions between traces and vias, in terms of small insertion loss, small return loss, and linear phase, are desirable for high-speed signal transmissions in multilayer PCBs and packages. Using the concepts from the equivalent transmission line model, the characteristic impedance of a single-ended signal via should be designed to match the trace impedance, which is normally 50 ohms for most practical systems. Additionally, the frequency-dependent loss of the equivalent transmission line model should be small, which demands that the imaginary part of the equivalent characteristic impedance be closed to zero. Furthermore, board resonance

from the parallel plane waveguide may also significantly impact signal transition at particular frequencies.

A one-conductor transmission line model can be used to approximate one single-ended signal via with multiple ground vias. For such a model, the per-unit-length parameter expression in equation (2.8) can be simplified as

$$\begin{aligned} Z &= \frac{1}{h \cdot Y_{pp}(1,1)} \\ Y &= 2j\omega h(C_a + C_b) \end{aligned} \quad (2.23)$$

The equivalent characteristic impedance  $Z_0$  can be calculated as

$$Z_0 = \sqrt{\frac{Z}{Y}} \quad (2.24)$$

When the distance between the ground via and the signal via is electrically small compared to the wavelength, based on (2.2) and (2.21), the per-unit-length impedance becomes demonstrably smaller when the ground via is closer to the signal via. Thus, the dielectric and skin-effect loss, which can be reflected by the imaginary part of  $Z_0$ , can be reduced by shorting the distance between the ground and signal vias.

The parallel plane impedance,  $Z_{pp}$ , shows high Q value at its resonant frequencies. But the Q value for the per-unit-length impedance can be minimized when ground via ports are added to the parallel plane matrix. In other words, the surrounding ground vias are effective at shielding board resonances for the signal via.

The value of the per-unit-length admittance is related to the via-plate capacitance. By changing the sizes of anti-pad and via drill, the characteristic impedance of signal vias can be adjusted.

**2.3.2. Differential-Signal Vias.** Differential signal vias in multi-layered circuit board are modelled here as coupled two-conductor transmission lines. The per-unit-length parameters for the differential transmission line model can be written as

$$\begin{aligned} \mathbf{Z} &= \begin{bmatrix} Y_{pp}(1,1) & Y_{pp}(1,2) \\ Y_{pp}(2,1) & Y_{pp}(2,2) \end{bmatrix}^{-1} / h \\ \mathbf{Y} &= \begin{bmatrix} 2j\omega h(C_a + C_b) & 0 \\ 0 & 2j\omega h(C_a + C_b) \end{bmatrix} \end{aligned} \quad (2.25)$$

When  $Y_{pp}(1,1)$  is not equal to  $Y_{pp}(2,2)$ , differential-mode signals flowing through differential vias are converted to common-mode signals, which are importance sources of electromagnetic interference.

Modal composition is adopted here to analyze the equivalent transmission line model for differential signal vias. First, modal voltages  $\mathbf{V}_m$  and currents  $\mathbf{I}_m$  are defined as

$$\begin{aligned} \mathbf{V}_m &= \mathbf{T}_v \mathbf{V} \\ \mathbf{I}_m &= \mathbf{T}_i \mathbf{I} \end{aligned} \quad (2.26)$$

where the complex matrices  $\mathbf{T}_v$  and  $\mathbf{T}_i$  are the transforms between the actual phasor line and the modal voltages and currents, respectively.

The transformation matrices  $\mathbf{T}_v$  and  $\mathbf{T}_i$  should satisfy

$$\mathbf{T}_i^t = \mathbf{T}_v^{-1} \quad (2.27)$$

where  $\mathbf{T}_i^t$  is the transpose of the matrix  $\mathbf{T}_i$ . The modal propagation constant  $\gamma$  and characteristic impedance  $\mathbf{Z}_0$  can be denoted as [20]

$$\begin{aligned} \gamma &= \sqrt{\mathbf{T}_i \mathbf{Y} \mathbf{Z} \mathbf{T}_i^{-1}} \\ \mathbf{Z}_0 &= \mathbf{Y}^{-1} \mathbf{T}_i^{-1} \gamma \mathbf{T}_i \end{aligned} \quad (2.28)$$

Equation (2.25) demonstrates that the admittance matrix is a diagonal matrix, because the weak capacitive coupling between two signal vias can be disregarded in this model. However, the per-unit-length impedance matrix has off-diagonal terms since the via ports are all coupled through the parallel-plane  $TM_{z0}$ -mode electromagnetic waves. Thus, multiplication of the per-unit-length impedance and admittance matrices,  $\mathbf{ZY}$ , is not diagonal.

Generally speaking, although the multiplication is not diagonal, there always exists a set of similarity transformation matrices, composed by the eigenvectors of  $\mathbf{ZY}$ , which could make the propagation constant and characteristic impedance diagonal. In other words, the physical voltages and currents can always be decomposed into two orthogonal modes.

In practical digital circuit design, the two modes of particular interest are the odd (differential) and even (common) modes. The corresponding similarity transformation matrices  $\mathbf{T}_v$  and  $\mathbf{T}_i$  for these two modes are defined as

$$\begin{aligned} \mathbf{T}_v &= \begin{bmatrix} 0.5 & 0.5 \\ 1 & -1 \end{bmatrix} \\ \mathbf{T}_i &= \begin{bmatrix} 1 & 1 \\ 0.5 & -0.5 \end{bmatrix} \end{aligned} \quad (2.29)$$

When the self parameters of the two signal conductors in the coupled multiconductor transmission line are exactly the same, the differential- and common-mode voltages and currents are orthogonal. In other words, the propagation constant and characteristic impedance matrices are diagonal when the two signal conductors are symmetric, and the similarity transformation matrices defined in equation (2.29). Mapping back to the differential signal via structure considered here, two symmetric signal conductors in the equivalent coupled MTL mean two identical signal vias with the same via-plate capacitances, symmetric surrounding ground vias, and symmetric locations on the board. Consequently, mode conversions between the differential and common modes vanish when perfectly symmetric signal vias are designed.

When the similarity transformation matrices  $\mathbf{T}_v$  and  $\mathbf{T}_i$  in (2.29) are used as the two orthogonal bases for mode composition, the mode impedance matrix can be written as

$$\mathbf{Z}_m = \begin{bmatrix} Z_{11} + Z_{12} & 0 \\ 0 & Z_{11} - Z_{12} \end{bmatrix} \quad (2.30)$$

where  $Z_m(1,1)$  is common-mode impedance and  $Z_m(2,2)$  is differential-mode impedance.

As noted above, when the value of impedance become small, the board resonance as well as the loss will both be small. Equation (2.30) indicates clearly that the differential-mode impedance  $Z_m(2,2)$  is just the difference between self and mutual term of single-end impedance. Thus, differential signalling is effective to reduce loss and board resonance because the differential-mode impedance  $Z_m(2,2)$  is reduced compared to the impedance  $Z_{11}$  of a single-ended via.

**2.3.3. Multiple-Signal Vias.** Crosstalk among multiple-signal vias is an important problem in high-speed digital circuits. It may distort signal integrity and increase jitter, especially when via density is high. Crosstalk among signal vias can be analysed based on the equivalent transmission line model, borrowing the crosstalk concepts from

multiple transmission line theory. The via length is usually electrically short in a practical print circuit board and the coupling among different vias can be considered weak. The equivalent transmission line derived from multi-via structure should also be electrically short. Besides, the second-order induced currents and voltages in the aggressor can be disregarded due to weak coupling. Therefore, the near-end and far-end crosstalk can be decoupled into superposition of inductive coupling and capacitive coupling as [21]

$$\begin{aligned} V_{NE} &= \frac{R_{NE}}{R_{NE} + R_{FE}} j\omega L_m I_{ag} + \frac{R_{NE} R_{FE}}{R_{NE} + R_{FE}} j\omega C_m V_{ag} \\ V_{FE} &= -\frac{R_{NE}}{R_{NE} + R_{FE}} j\omega L_m I_{ag} + \frac{R_{NE} R_{FE}}{R_{NE} + R_{FE}} j\omega C_m V_{ag} \end{aligned} \quad (2.31)$$

where  $V_{NE}$  and  $V_{FE}$  are near-end and far-end phasor crosstalk voltages and  $R_{NE}$  and  $R_{FE}$  are terminations at the near end and far end. The terms  $L_m$  and  $C_m$  denote mutual inductance and capacitance between aggressor and victim,  $V_{ag}$  and  $I_{ag}$  are voltage and current at aggressor, respectively.

Equation (2.6) demonstrates that the mutual capacitances among different signal vias is zero in the equivalent multi-conductor transmission line model because the capacitive coupling between two vias is much weaker than the via-plane couplings when these two vias do not share a single anti-pad. As a result, crosstalk among vias is dominated only by inductive couplings, and the near-end and far-end crosstalk S parameters between via i and j can be written as

$$\begin{aligned} S_{near} &= \mathbf{Z}(i, j) \cdot l / Z_{ref} \\ S_{far} &= -\mathbf{Z}(i, j) \cdot l / Z_{ref} \end{aligned} \quad (2.32)$$

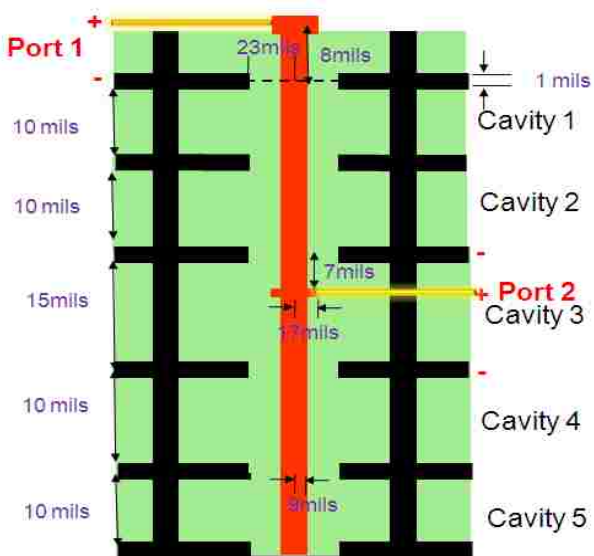
where  $l$  is the length of the via and  $Z_{ref}$  is the reference impedance for the S parameters.

The near-end crosstalk and far-end crosstalk are out of phase, but they have the same magnitude. The crosstalk is proportional to the via coupling length, which is determined by the thickness of each individual dielectric layer and the number of layers in the PCB. Thus, a thin dielectric layer could reduce the crosstalk level. Furthermore, when ground vias are set to surround the two signal vias considered here, the mutual impedance and the crosstalk level decrease.

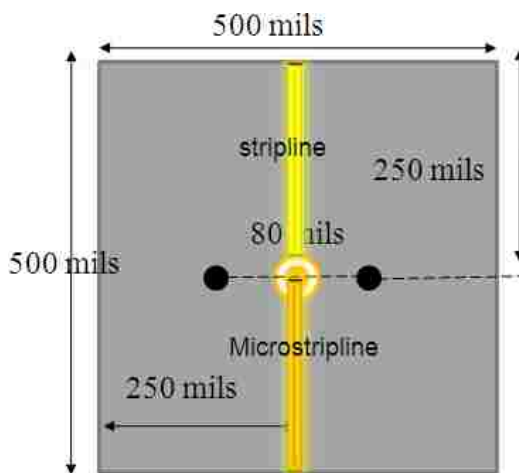
## 2.4 VALIDATION OF EQUIVALENT TRANSMISSION LINE MODEL

Figure 2.12 shows a typical geometry of a single-ended signal via surrounded by two ground vias in a multi-layered PCB. The signal via is used to route the signal from the microstrip line at the top layer to the stripline in the middle of Cavity 3. All the geometrical details can be found in Fig. 2.12. The dielectric layer has a dielectric constant of 4.0 and a loss tangent of 0.02. Perfect magnetic boundary conditions are assigned at the edges of the boards for both the transmission line model and full-wave simulation. The ports are at the edge of microstrip line and stripline.

The equivalent transmission line model with via-stripline connection is applied to the via model in Fig. 2.12. For validation, the finite element method (FEM) from High Frequency Structural Simulator (HFSS) is also used to simulate the same geometry. The return loss of Port 1 and the insertion loss between Port 1 and 2 are shown in Figs. 2.13 and 2.14. The results indicate close agreement between equivalent transmission line model and FEM at frequencies below 20 GHz. The minor discrepancies between full-wave methods and the equivalent transmission line model are mainly a result of disregarding high-order couplings among vias. The computational time for FEM is 4.5 hours while the equivalent transmission line model requires only 3 minutes.



(a) PCB stack up



(b) Top view

Fig. 2.12 Single-ended signal via with two ground vias.

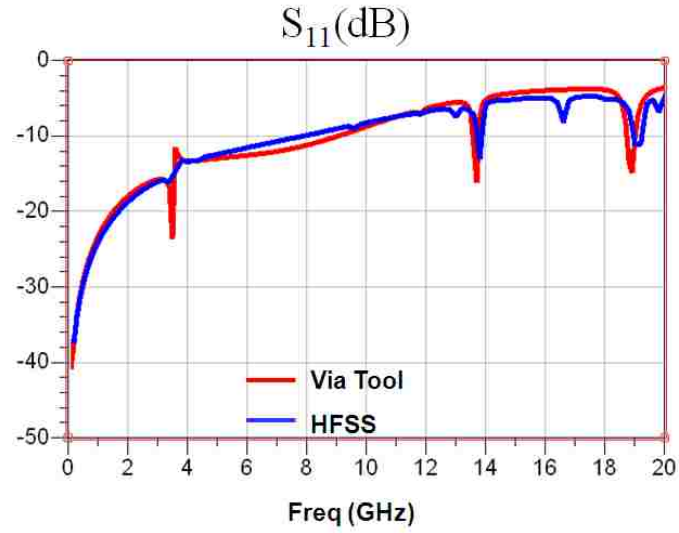


Fig. 2.13  $|S_{11}|$  of the via structures with trace connections shown in Fig. 2.12.

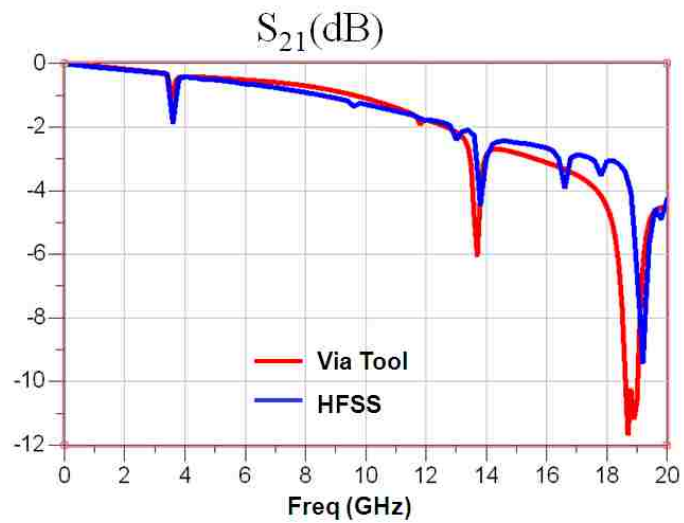


Fig. 2.14  $|S_{21}|$  of the via structures with trace connections shown in Fig. 2.12.



The geometry used as another validation example is extracted from a practical motherboard design, with shapes approximated as shown in Fig. 2.15. This geometry contains one cavity with 108 vias in the region on the board sketched within the dashed line in Fig. 2.13. Fig. 2.14 shows the zoom-in via region bounded by the dashed line in Fig. 2.13. The height of the cavity is 40/mil and the material for the dielectric layer is FR4. The crosstalk occurs are between two signal vias in the centre of the via region. The pitch size of between these two signal vias is 50 mils. Seven ground vias are distributed at the edges of the via region as shown in Fig. 2.16. The approximate distance between each ground via and the center of the signal vias is 180 mils. The remaining vias are terminated with 50 ohm resistors.

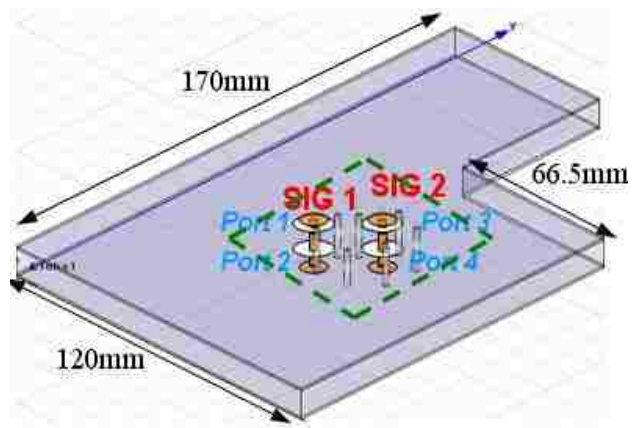


Fig. 2.15 Geometry under study with different ground via patterns.

The magnitudes and phases for near-end cross talk (NEXT) and far-end cross talk (FEXT) of two signal vias in Fig. 2.15 are illustrated in Fig. 2.17 and 2.18, respectively. The crosstalk results based on the equivalent transmission line model are calculated using equation (2.32). Close agreement has been achieved when comparing the results of the equivalent transmission line model with those of the physics-based circuit model. The crosstalk results demonstrate that only inductive couplings are dominant between vias

because the magnitudes of NEXT and FEXT are identical while the phases are opposite. At frequencies above 1 GHz, the phases of NEXT and FEXT deviate from  $\pm 90^\circ$  because the influence of dielectric and skin-effect loss become significant when signal flows through vias at high frequencies.

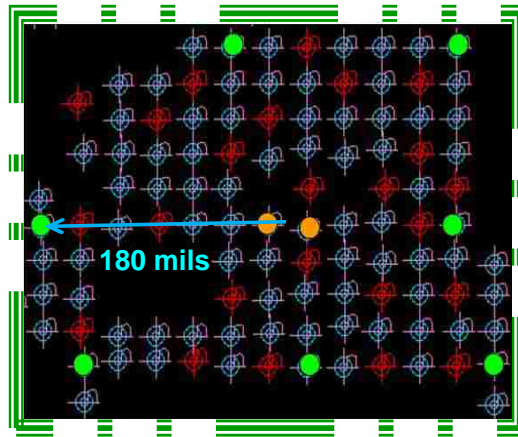


Fig. 2.16 Top view of the region within the dashed line in Fig. 2.15.

The last example validates the concept of via impedance by model-to-hardware correlation. Three differential signal-via structures were designed in the test vehicles, as shown in Fig. 2.19. All three test coupons, A, B and C, had same stack-up and via positions. The dielectric material for all three test vehicles was FR4, with a dielectric constant of 3.78 in the middle cavity and 3.62 in other cavities. The loss tangent was 0.018. All the plane coppers were 1.20 mils thick. The only difference among the three cases was the dimensions of the antipads of the signal vias. The diameters of the antipads for test case A, B and C are 40 mils, 26 mils and 50 mils, respectively.

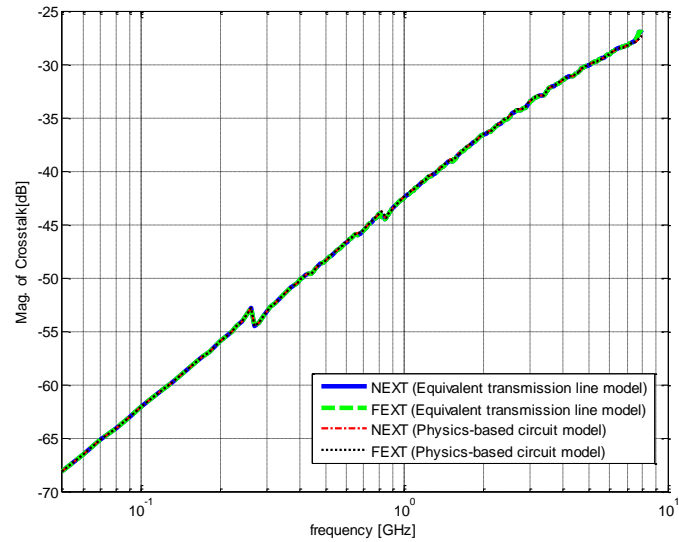


Fig. 2.17 Magnitudes of NEXT and FEXT for the geometry shown in Fig. 2.16.

The real parts of the characteristic impedances of the via structure in Fig. 2.19 were obtained from the equivalent transmission line model, as shown in Fig. 2.20. When the frequency is below 15 GHz, the imaginary parts of the characteristic impedances of the via structures are close to zero because the loss is relatively small. Thus, the impedance mismatches are mainly reflected by the real parts. At frequencies of up to 15 GHz, the impedances of the via structure are nearly a constant. The characteristic impedances of the differential via structures for test cases, A, B and C were designed to be 103 ohms, 93 ohms, and 110 ohms, respectively.

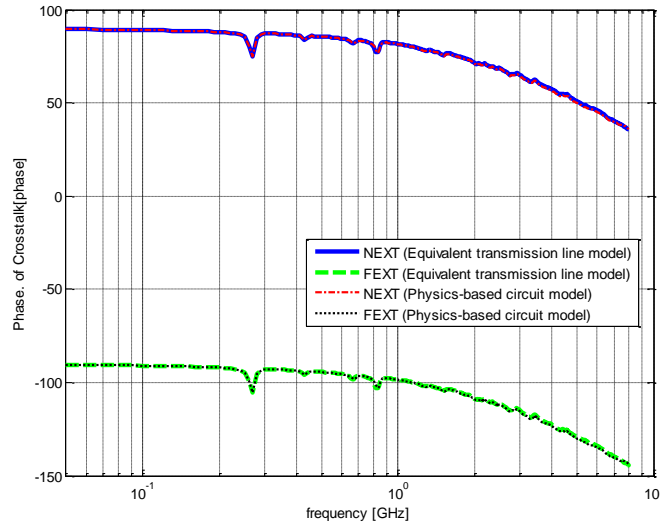
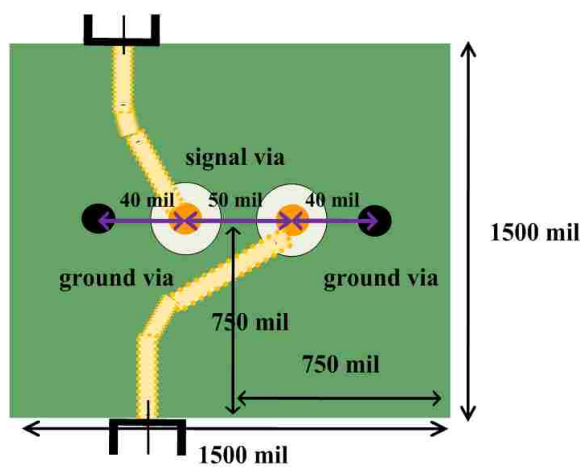
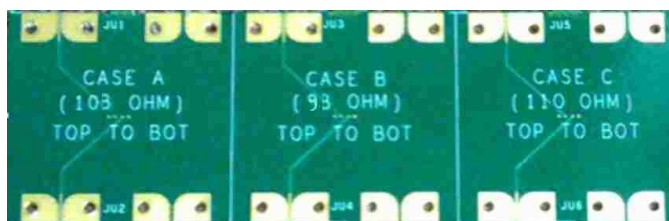
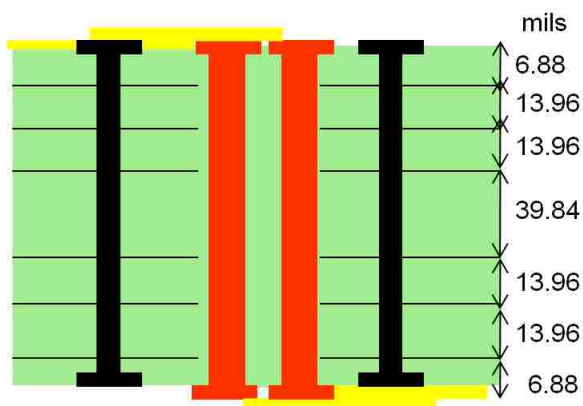


Fig. 2.18 Phases of NEXT and FEXT for the geometry shown in Fig. 2.16

Figure 2.21 shows the TDR results for three via structures in the test vehicles. The TDR had a rise time of 34 ps, indicating that the knee frequency was roughly 15 GHz. The discontinuities at 7.8 ns in Fig. 2.21 indicate the impedance of the via structures. The via impedances measured from TDR were clearly well matched with the values from the equivalent transmission line model. The delay time caused by the via structures was roughly 0.2 ns, which is reasonable for the via length and dielectric properties in the test coupons, considering the slow-mode effect. The differential-mode characteristic impedances of the microstrip on both the top and bottom sides were approximately 106 ohms. The small deeps at 7.5 and 8.1 ns in Fig. 2.21 were caused by the discontinuities of edge-launched SMA connectors.



(a) top view



(b) board cross-section diagram

Fig. 2.19 Via structures with microstrip and edge-launch connectors.

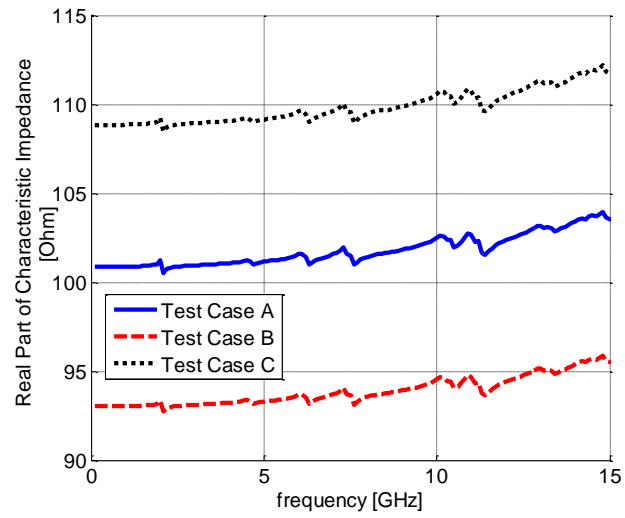


Fig. 2.20 Real parts of characteristic impedance of via structures in Fig. 2.19, obtained from equivalent transmission line model.

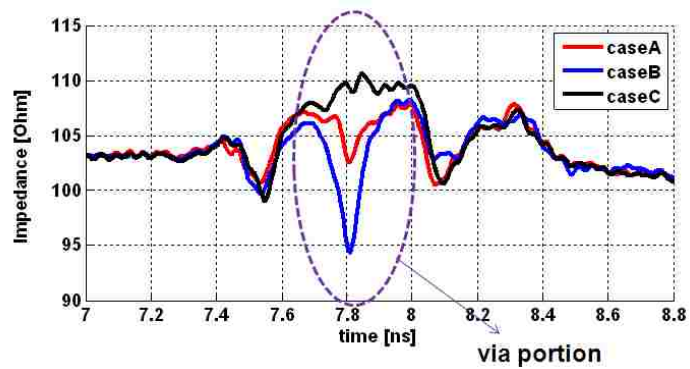


Fig. 2.21 TDR results for the three test via structures in Fig. 2.19.

## **2.5. DESIGN AND OPTIMIZATION OF DIFFERENTIAL SIGNAL VIAS IN MULTILAYERED PCB**

**2.5.1. Design Objective.** Smooth transitions between differential traces and vias are desirable for high-speed signal transmissions in multilayer PCBs and packages. First, mode conversions from differential-mode to common-mode signals should be avoided since common-mode signals could cause potential electromagnetic interference problems. Besides, attenuation in differential signalling during via transition is critical especially for high speed serial differential (HSSD) gigahertz signalling. Since much the return current flows through the dielectric layer at high frequencies, the frequency-dependent dielectric loss results in intersymbol interference, which can reduce the overall error-free bandwidth of a channel. Moreover, the via resonances caused by the reflection wave from the board edge could distort the signal significantly at some specific frequencies. Thus, losses and board resonances should be minimized by proper design of via geometry. Last but not least, impedance match is still critical for return loss for the differential channels. The characteristic impedances of differential traces are normally 100 Ohms for most of the practical systems. Therefore, the differential signal via structure should be designed with an equivalent characteristic impedance of  $100+j0$  ohms.

**2.5.2. Design Guidelines for Differential Signal Vias for High-Speed Signal Transmission.** Due to the limitations of manufacturing processes and other design considerations, some geometrical parameters in the PCB (e.g. board size, dielectric thickness, loss tangent, and drill size) cannot be easily changed, although they can also influence the performances of differential signal vias. On the other hand, some parameters (e.g. the number and locations of ground via and anti-pad sizes) are easier to adjust. The following proposes a general design guideline for differential-signal via pairs based on the equivalent transmission line model. The design parameters focus mainly on the number of ground vias, the location of ground vias and anti-pad sizes. These guidelines are based on frequencies of up to 40 GHz.

Design of differential-signal via pairs must begin with symmetric-signal via structures to minimize mode conversions between common-mode and differential-mode signals. All the parameters for both signal vias should be identical, including the via-plate capacitances and the relative positions of ground vias and the circuit board. In practice,

however, perfectly symmetric signal vias are not always possible. The differential and common modes are not orthogonal, and there are mode conversions due to asymmetric signal vias present in the geometry. To avoid mode conversion, some lumped circuit components can be added to compensate for the differences in two self parameters each for both  $Z$  and  $Y$  matrices in Equation (2.25). Extra capacitances for balancing a via structure that is asymmetric due to different sizes of drill, pad, and anti-pad are effective in a broad band. However, the extra inductive components for balancing a via structure that is asymmetric with respect to ground via location and board are effective only in a narrow band, because the via inductances in (2.9) are frequency-dependant. Similarly, when asymmetric differential traces are connected to signal vias, the surrounding ground vias and via-plate capacitances can be designed asymmetrically so that the differential-signal via pair balances the differences caused by asymmetric traces.

Secondly, loss and board resonance should be considered for HSSD gigahertz signalling. Loss can be evaluated by the attenuator factor or by the imaginary part of the characteristic impedance from the equivalent transmission line model. Further, board resonance is related only to the Q factor of per-unit-length impedance. Since loss and board resonance are particularly analyzed here for differential-signal vias, in particular, by minimizing differential-mode impedance  $Z_m(2,2)$  in (2.30), the via structure can be optimized with respect to loss and board resonance.

The ground vias effectively reduce loss and to shield board resonance. When the distance between ground via and signal via is electrically small compared to the wavelength, the loss and board resonance can be decreased by shorting the distance between ground via and signal via. Thus, as a rule of thumb, a short distance between ground via and signal via is required for ground via design. Furthermore, for a differential signal, the middle line of the differential-signal via pair can be considered a perfect electric conductor wall. Adding ground vias along this middle line has no effect on differential signalling if two signal vias are perfectly symmetric. Therefore, ground vias should be located as far as possible away from the middle line if the same distance from ground via to signal via can be maintained. Last but not least, the more ground vias are added, the smaller the value the differential-mode impedance in (2.32) will be. Meanwhile, the average distance among ground vias should be maximized. In other

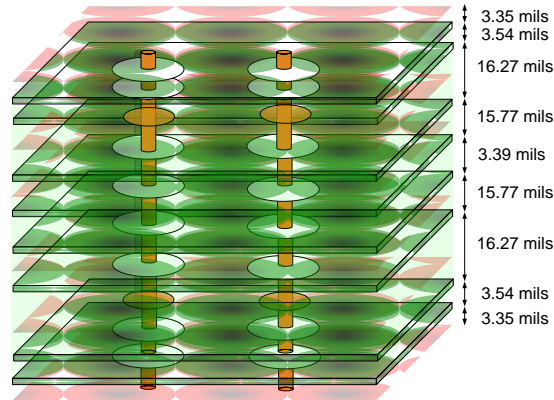


word, ground vias should be symmetrically distributed around the signal via pair to minimize loss and shield board resonance.

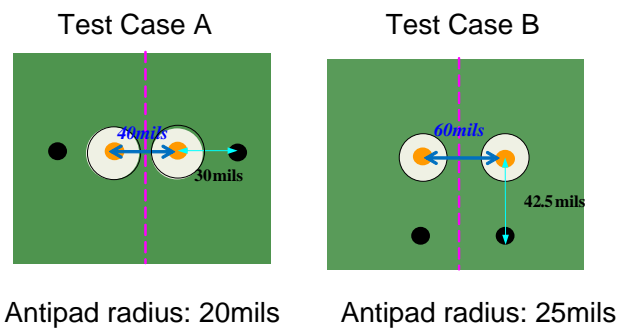
The pitch size of signal vias also plays an important role in loss and resonances during signal transition. When a smaller signal pitch size is selected, the value of single-ended mutual impedance  $Z_{12}$  is closer to self impedance  $Z_{11}$ . Therefore, a smaller value of differential-mode impedance can be obtained, which indicates that the loss will become smaller. Thus, the use of small-signal pitch size is crucial in practical design to shield board resonance and reduce loss.

With suitable ground via pattern and signal via pitch size, loss and board resonance are minimized. The final step is to design matched characteristic impedance for differential signal vias. The equivalent differential characteristic impedance of signal vias should be matched with the characteristic impedance of the traces. The equivalent differential characteristic impedance is monotonic to via-plate capacitance value. The via-plate capacitances are related to the anti-pad dimensions [18], indicating that the differential via characteristic impedance may be designed close to the differential trace impedance by adjusting the sizes of the anti-pads.

**2.5.3 Example of Differential-Signal Via Structure Designed According to Guidelines Proposed in Section 2.5.2.** Figure 2.22 (a) shows a typical multilayered PCB measuring 1.5'' by 1.5''. A pair of differential-signal vias must be designed to route the traces from the top layer to the bottom layer. Two ground vias are allowed to set per signal via pair. The ground via location, signal pitch size, and anti-pad size can be adjusted for high signal path performance. Test case A shown in Fig. 2.22(b) was cautiously designed to obtain the optimized signal performances according to the design guidelines presented above. Test case B was a via structure with arbitrarily chosen practical design parameters. Each copper plane was 0.7 mil thick, and the dielectric layer had a dielectric constant of 4.0 and a loss tangent of 0.02. Figure 2.22 provides other geometrical details.



(a) PCB stack up for a differential-signal via pair



(b) comparison of two test cases

Fig. 2.22 Demonstration of design guideline effectiveness.

Figures 2.23 and 2.24 show the differential-mode  $S$  parameters of the two test structures shown in Fig. 2.22. The differential-mode return loss ( $S_{dd11}$ ) of test case A was much smaller than that of test case B, indicating that the characteristic impedance of the via structure in test case A was closer to the system impedance. Meanwhile, the differential-mode insertion loss ( $S_{dd21}$ ) of test case A was nearly zero, with smaller resonances, illustrating that the effectiveness of ground via locations and pitch size optimized for case A to reduce loss and board resonances. Figures 2.25 and 2.26 demonstrate that the real part of the equivalent differential characteristic impedance for test case A was closer to 100 ohms and the imaginary part was closer to 0 ohms.

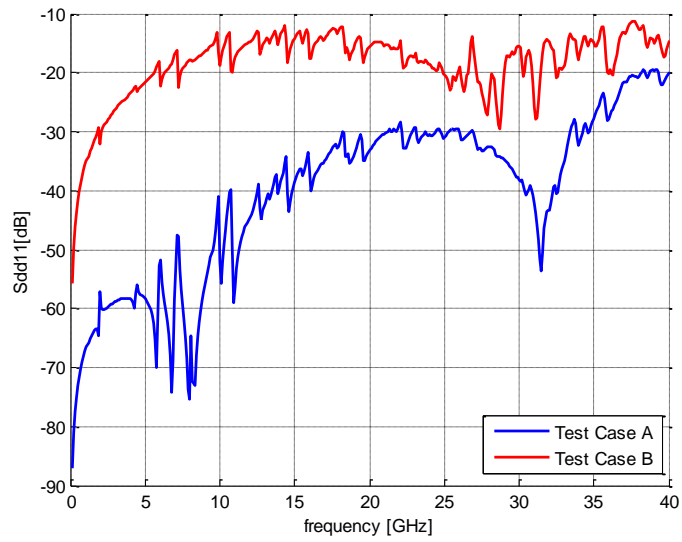


Fig. 2.23  $|S_{dd11}|$  of two differential-signal via structures shown in Fig. 2.22.

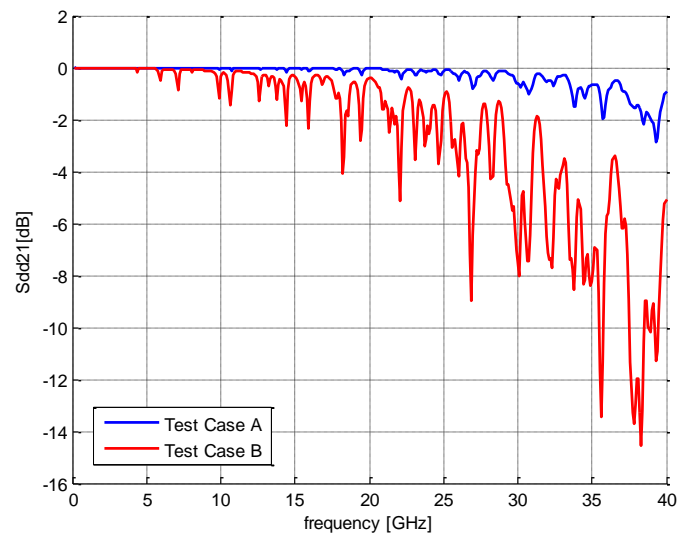


Fig. 2.24  $|S_{dd21}|$  of two differential-signal via structures shown in Fig. 2.22.

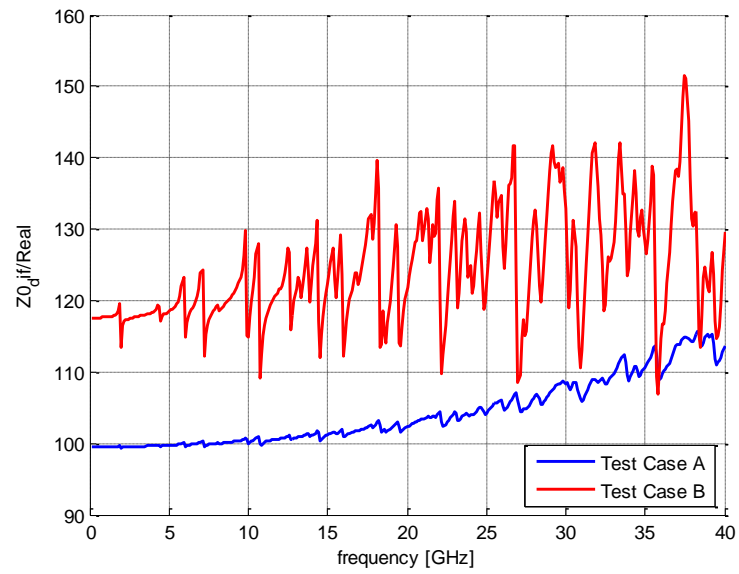


Fig. 2.25 Real part of the equivalent differential  $Z_0$  of two differential-signal via structures shown in Fig. 2.22.

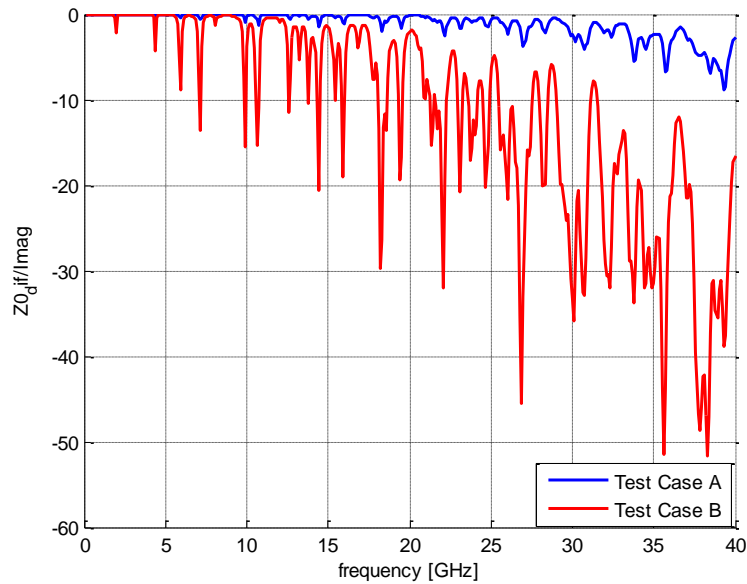


Fig. 2.26 Imaginary part of the equivalent differential  $Z_0$  of two differential-signal via structures shown in Fig. 2.22.

A time-domain simulation using the concept of time-domain reflectometry was also set up to demonstrate the effectiveness of the design guidelines. As shown in Fig. 2.27, a differential ideal lossless transmission line, with characteristic impedance of 100 ohms and delay time of 125 ps connected with a differential via structure with the same configuration as the two test cases shown in Fig. 2.12. The source was a step voltage source with 4 V. The rise time of the step source was 25 ps, meaning that the knee frequency for the input signal was 20 GHz. The source impedance was 100 ohms. Two differential-signal vias were each terminated by a 50 ohm resistor.

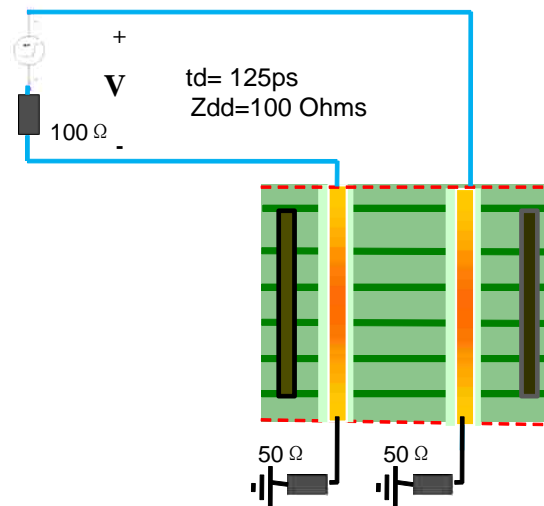


Fig. 2.27 Setup for time-domain simulation of the differential-signal via structures shown in Fig. 2.22.

Figure 2.28 shows the differential voltage waveform at input. The reflected waves propagated back to the launch point after twice the delay time of the transmission line. The deviation voltage from 2V in the curve along the time axis, from .25 ns to .31 ns, indicated that the electrical length of the signal via. For test case A, the impedance of the via structure was closer to the impedance of transmission line because the reflected voltage wave was still nearly 2V. The reflected voltage for test case B indicated that the

differential impedance of its corresponding via structure was higher than that of the transmission line, an observation consistent with the impedance plot shown in Fig. 2.25.

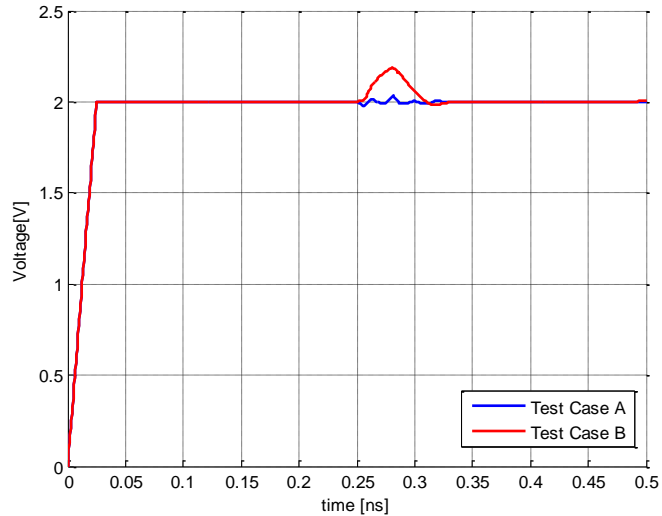


Fig. 2.28 Time-domain simulation results for differential voltage at launch point.

## 2.6. SUMMARY OF EQUIVALENT TRANSMISSION-LINE VIA MODEL

This paper proposed a general equivalent transmission-line model for via structures with closed-form per-unit-length parameters. The mathematic relationships between equivalent transmission-line parameter and via geometry are well established. Via design and optimization in practical circuit board can proceed with the help of MTL theory based on the equivalent transmission line model. As a result, design guidelines are introduced for differential signal vias. These permit efficient optimization of differential via structure to obtain a smooth signal path for gigahertz signalling.

### 3. IC RADIATION AND CONDUCTIVE EMISSION MODELS

#### 3.1. INTRODUCTION OF IC EMISSION MODELS

In the diagnosis and prediction of EMI and RFI problems, the accurate radiation model of chip and chip-package is very important. With these models, manufacturers can predict the electromagnetic radiated emission of their products. In previous work, many methods have been established to model chip radiation. In [25] the chip is modelled as several dipoles, and a set of TEM cell measurements are used to determine both the magnitudes and phases of the dipole moments. In [28], near-field measurement is used to estimate currents in chips. In [29], using near-field measurement, the electronic circuit is modelled as a set of horizontally placed electric or magnetic dipoles with different orientations.

As for the method using TEM cell measurement, the international standard IEC 61967-2 [25] describes a specific procedure to evaluate the component-level EMC performance of ICs from 150 kHz to 1 GHz via TEM cell measurements. However, specific IC emission models are desirable to further simulate and predict the radiated fields from ICs in complex systems. Previous work has established several models for determining the emissions from ICs. Models with mutual capacitance and inductance were extracted from TEM cell measurements to estimate the radiated emissions for simple structures in [26], [27]. A set of dipole arrays was proposed from near-field scanning measurements to model IC emissions in [28], [29]. The TEM cell and open area test site (OATS) measurements of a radiated device were correlated through a set of six electric and magnetic dipole moments in [30], where the extraction of the six dipole moments requires nine TEM cell measurements and, further, special shielding is needed for some of the measurement steps.

In the Section 3.2, it is validated that only three dipole moments out of the six are dominant when there is a large ground plane under the IC under test. Thus, the TEM cell measurement procedure proposed in [30] can be greatly simplified to three measurements instead of nine. Each of these three TEM cell measurements strictly follows the standard procedure proposed in IEC 61967-2. The IC emission model using three equivalent dipole moments is introduced with justifications. This model is validated using the far-

field measurements in a semi anechoic chamber for a test IC. An approach to incorporate the extract dipole moments as equivalent sources in a full-wave tool is developed, in order to model system-level EMI in complex environments.

Other than the radiated emission problems of IC, the interest in evaluating IC conducted emissions has grown in recent years since the reduction of the EME at IC level brings to a mitigation of system level emissions making needless expensive filtering and shielding components. Steep currents and voltage glitches at the power supply and ground pins of an IC and proper signals at its input/output (I/O) pins are considered IC conducted emissions since they drive the electromagnetic emissions (EMEs) of antennas composed of printed circuit board (PCB) traces and/or interconnecting cables of the electronic system, which the IC is part of. In order to characterize ICs in terms of both conducted EME, several measurement methods have been developed until now, some of them are international standards [39]. Section 3.3 will deal with the problems of the conduction emission.

### **3.2. RADIATED EMISSION MODEL BASED ON TEM CELL MEASUREMENT**

An IC emission model is proposed using three dipole moments ( $P_z$ ,  $M_x$ , and  $M_y$ ) extracted from TEM cell measurements. This model is validated using the comparisons between the radiated fields calculated using the extracted dipole moments as equivalent sources and those obtained from the far-field measurements for a PLL test chip. An approach with combined loop and wire antennas to incorporate the dipole moments as sources in commercial full-wave EM tools will also be developed.

**3.2.1. Dipole Model, Approach Details, and Key Issues.** For EMC applications, the maximum emission level is of interest, instead of the radiation nulls or side lobes. Then, it becomes a good approximation to neglect the phase differences between the various moments. Particularly, when the sizes of ICs are electrically small, only the initial dipole terms are dominant to determine the magnitude of the radiated fields [31].

Generally speaking, a complete set of six dipole moments are necessary to represent the emissions of a device under test (DUT), including three electric ones  $P_x$ ,  $P_y$ ,



$P_z$  and three magnetic ones  $M_x$ ,  $M_y$ ,  $M_z$ . The subscript (x, y, or z) indicates the individual direction of each dipole moment. The electric and magnetic dipoles are defined as [32]

$$\begin{aligned}\mathbf{P} &= \int_v \mathbf{J}(\mathbf{r}') dv' \\ \mathbf{M} &= \frac{1}{2} \int_v \mathbf{r}' \times \mathbf{J}(\mathbf{r}') dv'\end{aligned}\quad (3.1)$$

where  $\mathbf{J}$  is the current density distributed over a volume  $v$ , and  $\mathbf{r}'$  denotes the position vector of the source point.

For a typical IC shown in Fig. 3.1, its dimensions in x and y directions are much larger than its z-directional height. When there is a large perfect electric conductor (PEC) ground plane under the IC,  $P_x$ ,  $P_y$ , and  $M_z$  cannot be the dominant dipole moments because their fields cannot satisfy the PEC boundary condition at the ground plane, if the distance between the IC and the ground plane is small enough. Further, the main current loops comprised of the IC traces and the ground reference plane can be sufficiently modelled using  $M_x$  and  $M_y$ . Similarly, most patches in the IC against the ground reference plane can be sufficiently modelled using  $P_z$ . Therefore, for the typical IC structures,  $M_x$ ,  $M_y$  and  $P_z$  are adequate as the equivalent sources of their electromagnetic emissions.

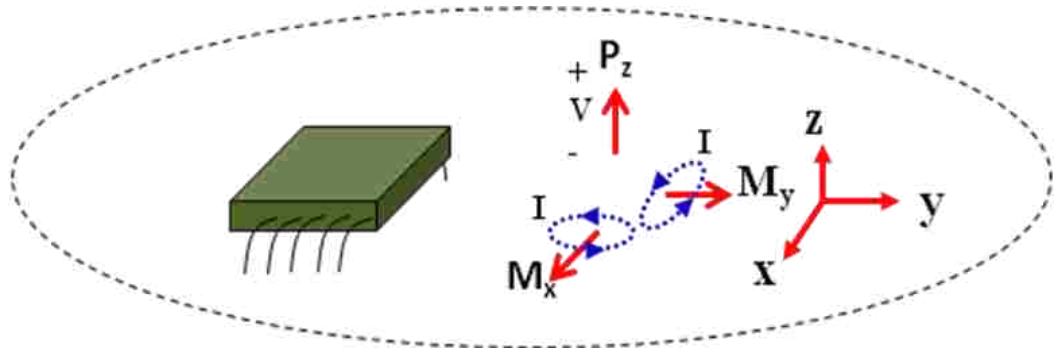


Fig. 3.1 Typical dimensions of IC and its emission model using three equivalent dipole moments.

The three equivalent dipole moments in the proposed IC emission model can be calculated from three TEM measurements as [30]

$$\begin{aligned}
 b_1 &= P_z^2 + k_0^2 M_y^2 \\
 b_2 &= P_z^2 + \frac{1}{2} k_0^2 M_x^2 + \frac{1}{2} k_0^2 M_y^2 - k_0^2 M_y M_x \\
 b_3 &= P_z^2 + k_0^2 M_x^2
 \end{aligned} \tag{3.2}$$

where  $k_0$  is the wave number in the free space; and,  $b_1$ ,  $b_2$ , and  $b_3$  are the normalized power measured using the TEM cell when the IC under test is orientated as in Positions 1, 2, and 3 shown in Fig. 3.2, respectively. The three measurement positions have a rotation of 0, -45, and 90 degrees as illustrated by the white lines in Fig. 3.2.

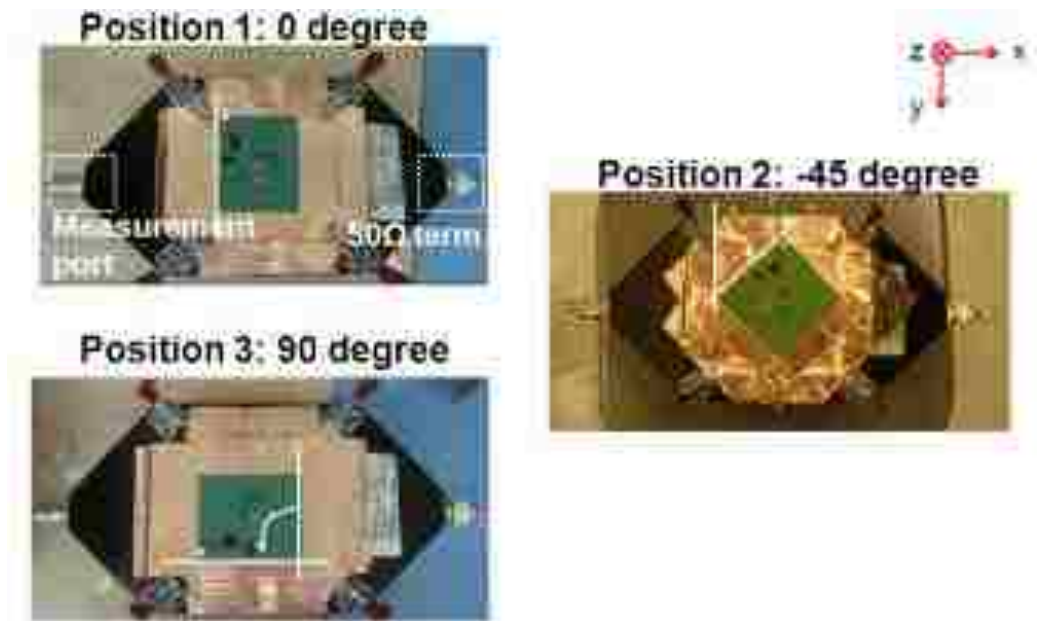


Fig. 3.2 Three TEM cell measurements necessary to extract the proposed IC emission model using (3.2).

An alternative approach is to use a hybrid to separate the contributions of  $P_z$ ,  $M_x$ , and  $M_y$ . A test setup of using a hybrid in the TEM cell measurement is shown in Fig. 3.3. The hybrid can generate signals that are the sum and the difference of the two TEM cell

outputs. The sum of the two output voltages is proportional to the electric field coupling, since the electric field coupling, if the DUT is located in the center of the TEM cell, generate two responses that are in phase and the magnetic field coupling generates two out-of-phase ones. Similarly, the difference of the voltages is proportional to the magnetic field coupling. As a result, the equivalent electric dipole moment  $P_z$  can be obtained from the sum of the voltages as

$$P_z = \sqrt{\frac{(A+B)}{2}} \quad (3.3)$$

And the difference of the voltage gives the magnetic dipole moment as

$$M = \sqrt{\frac{(A-B)}{2k_0^2}} \quad (3.4)$$

Measurements with two DUT positions (0 and 90 degrees) are sufficient to calculate the  $P_z$ ,  $M_x$ , and  $M_y$  using (3.3) and (3.4). Notice that the  $P_z$  value shall be approximately the same at any measurement position.

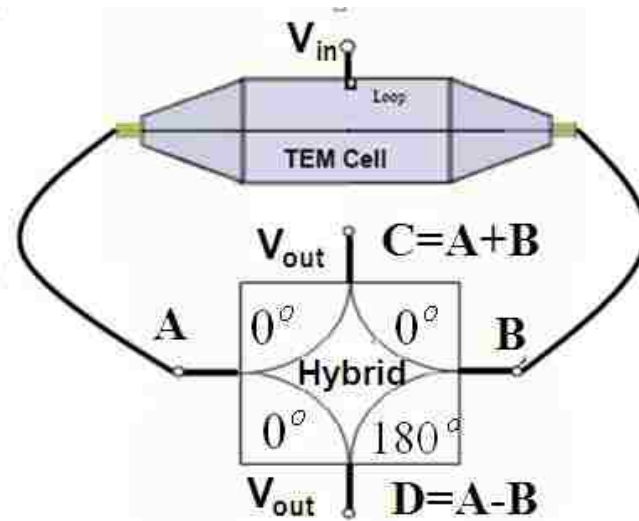


Fig. 3.3 TEM cell measurement with a hybrid.

**3.2.2. Test Board Design.** A phase locked loop (PLL) chip was used as a test IC to illustrate the experimental procedure to obtain the IC emission model proposed in this report. Then, far-field emission measurements were performed to validate the model.

The test print circuit board (PCB) designed according to the requirements of the IEC standard 61967-1 is shown in Fig. 3.4. The input signal of the PLL has a fundamental frequency of 25 MHz while the output signal doubles the input frequency. The PLL chip is the only component on the top side of the board while other components such as power regulator, terminations, and decoupling capacitors are on the bottom side of the board. The board size, stackup, as well as via type followed the specifications in IEC 61967-1.

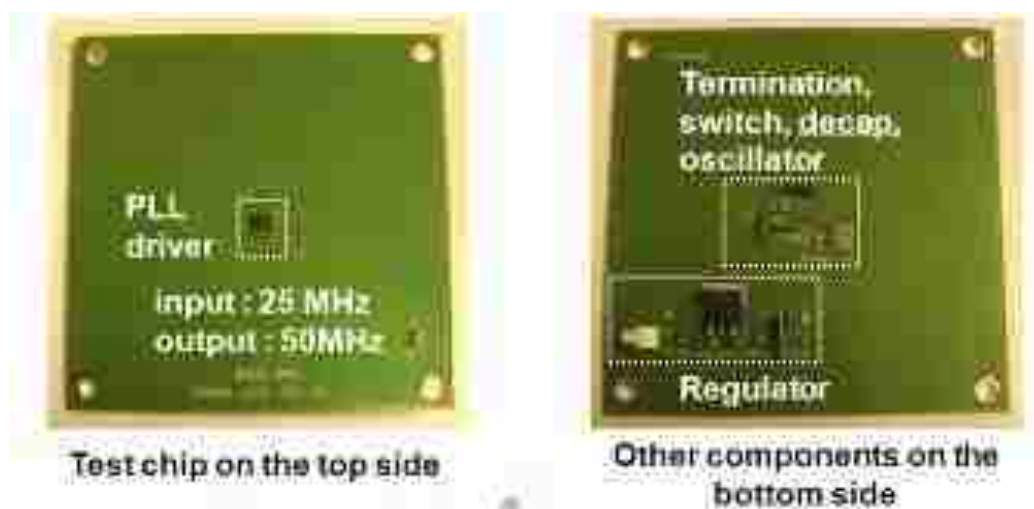


Fig. 3.4 Test PCB geometry with a PLL chip.

**3.2.3. Measurement and Far Field Validations.** As shown in Fig. 3.2, the test board was then measured in 3 different positions by rotating the test board with certain degrees with regard to the TEM cell orientation. The TEM cell terminations are illustrated in Fig. 3.5, with one port terminated with a 50-Ohm matched load and the

other port connected with a spectrum analyser. The output power at the measurement port was measured from 10 MHz to 1 GHz.

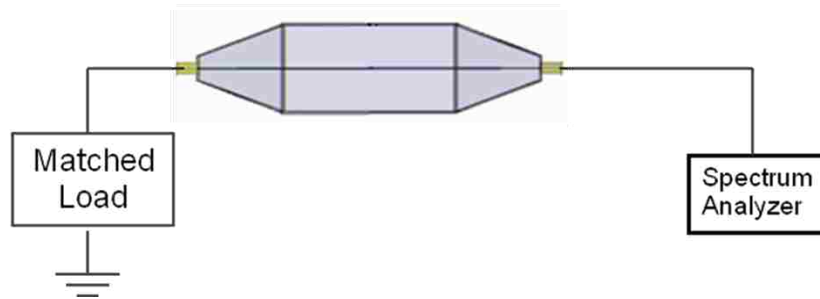


Fig. 3.5 TEM cell terminations.

The measured results of the output power for all three measurements using the spectrum analyser are shown in Fig. 3.6. The peaks correspond to the fundamental and harmonic frequencies of the clock. Then the equivalent electric and magnetic dipole moments were calculated based on the measured results using (2), and are shown in Fig. 3.7. Naturally, these dipole moments have peak values at the fundamental and harmonic frequencies.

To validate the extracted IC emission model, radiated fields can be calculated from the extracted dipole moments as sources, and compared with measurements. Closed-form expressions for the radiated fields generated by the known dipole sources can be derived for simple cases where Green's functions are available. One such case is to assume that the IC is placed on top of an infinitely large ground plane. The analytical expressions for the radiated fields from the dipole moments in this kind of half space can be easily obtained as in [33].

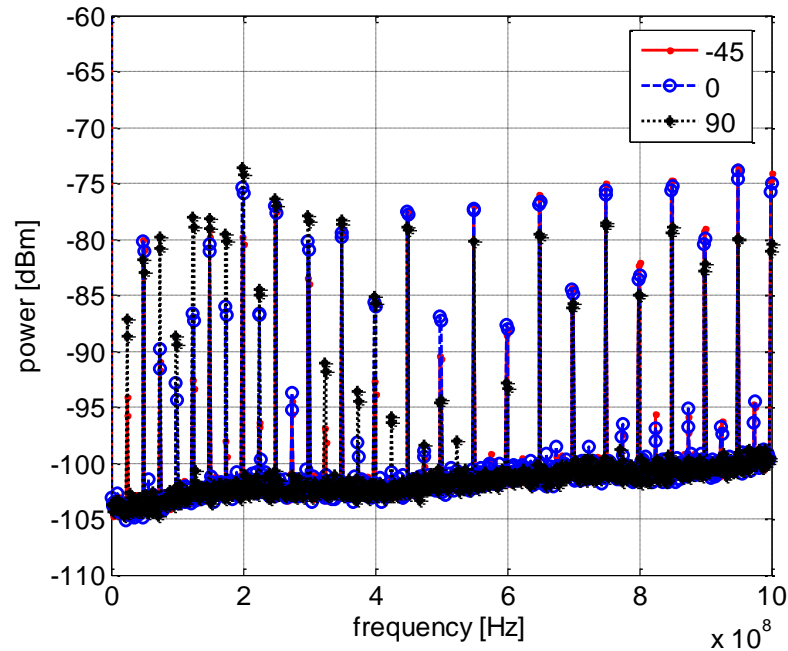


Fig. 3.6 Output power measured using a spectrum analyser for the test board placed in three different positions.

For validations, far-field measurements in a semi anechoic chamber were conducted to obtain the emissions from the IC chip in the half space. The experimental setup is shown in Fig. 3.8, where the setup of the DUT is different to the usual EMI testing. In this measurement, it is important to ensure that the IC is the only source of the radiated emission. Otherwise there's no apple-to-apple comparison with the analytical solution of the radiated fields from the extracted dipole moments. To remove the radiation from the test PCB as well as other components, the PCB was placed on the ground plane of the chamber with the side containing the PLL chip facing up. Then the board was completely covered using copper tape with only the test chip exposed, as shown in the Fig 3.8. The copper tape was connected to the ground plane of the chamber. Therefore, the test chip was equivalently placed on a very large ground plane. The radiated electric field was measured at 3.26 m away from the test board using a broadband antenna. To improve the signal to noise ratio, two amplifiers were used.

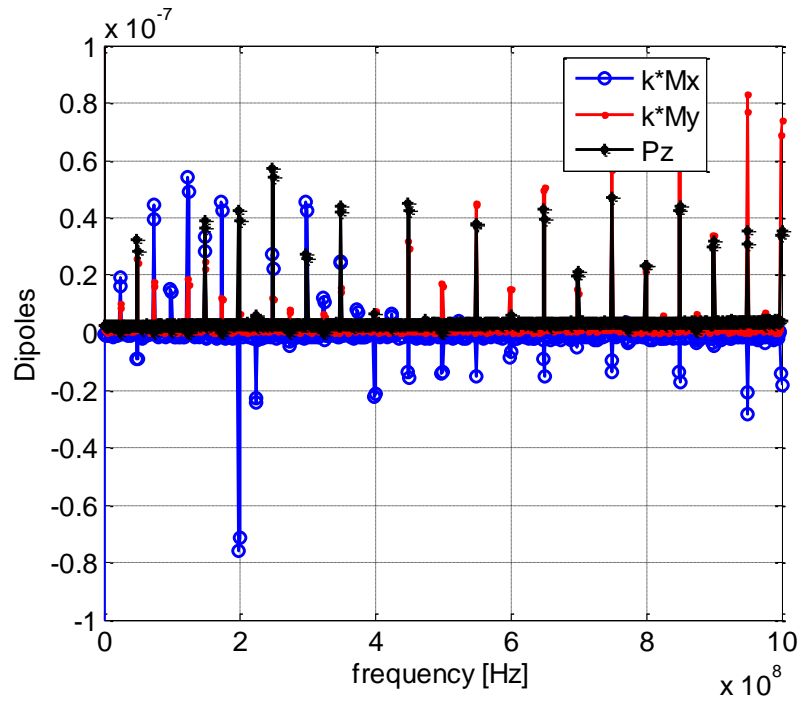


Fig. 3.7 Equivalent dipole moments extracted from the TEM cell measurements for the PLL chip under test.

For validations, far-field measurements in a semi anechoic chamber were conducted to obtain the emissions from the IC chip in the half space. The experimental setup is shown in Fig. 3.8, where the setup of the DUT is different to the usual EMI testing. In this measurement, it is important to ensure that the IC is the only source of the radiated emission. Otherwise there's no apple-to-apple comparison with the analytical solution of the radiated fields from the extracted dipole moments. To remove the radiation from the test PCB as well as other components, the PCB was placed on the ground plane of the chamber with the side containing the PLL chip facing up. Then the board was completely covered using copper tape with only the test chip exposed, as

shown in the Fig 3.8. The copper tape was connected to the ground plane of the chamber. Therefore, the test chip was equivalently placed on a very large ground plane. The radiated electric field was measured at 3.26 m away from the test board using a broadband antenna. To improve the signal to noise ratio, two amplifiers were used.

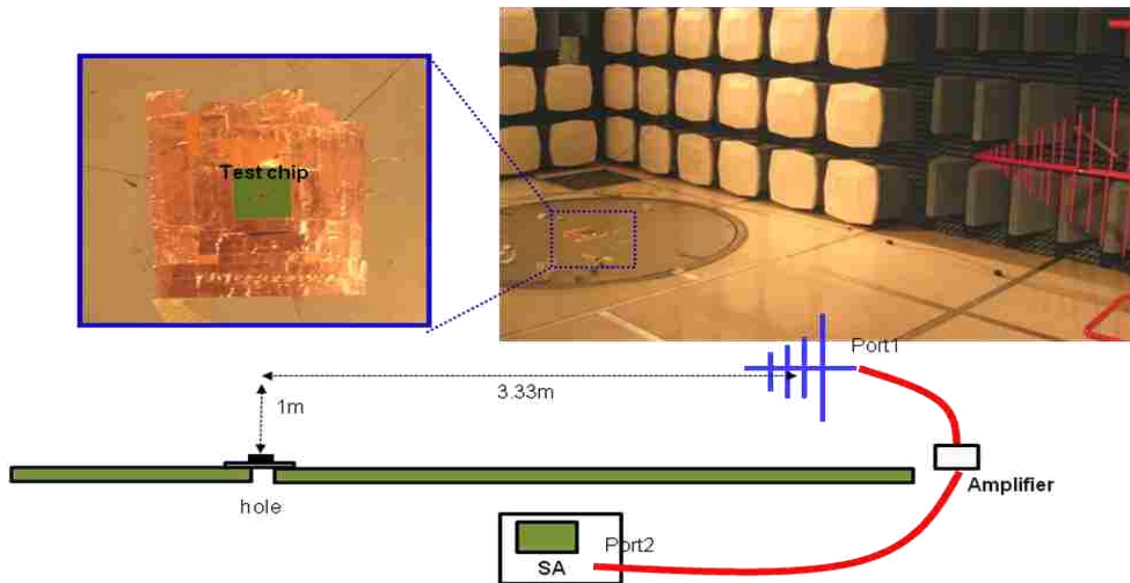


Fig. 3.8 Far-field measurement in a semi anechoic chamber.

The gain of the measurement setup including the gain of the amplifiers and the loss of the cables and the antenna factor are shown in Fig. 3.9, where the antenna factor was provided by the antenna manufacturer. Then, the radiated electric field can be calculated from the measured power at the spectrum analyzer as

$$E[dBuV / m] = (\text{Power}[dBm] + 107) - S_{21} + AF, \quad (3.5)$$

where  $S_{21}$  is the gain of the measurement setup; and,  $AF$  is the antenna factor.



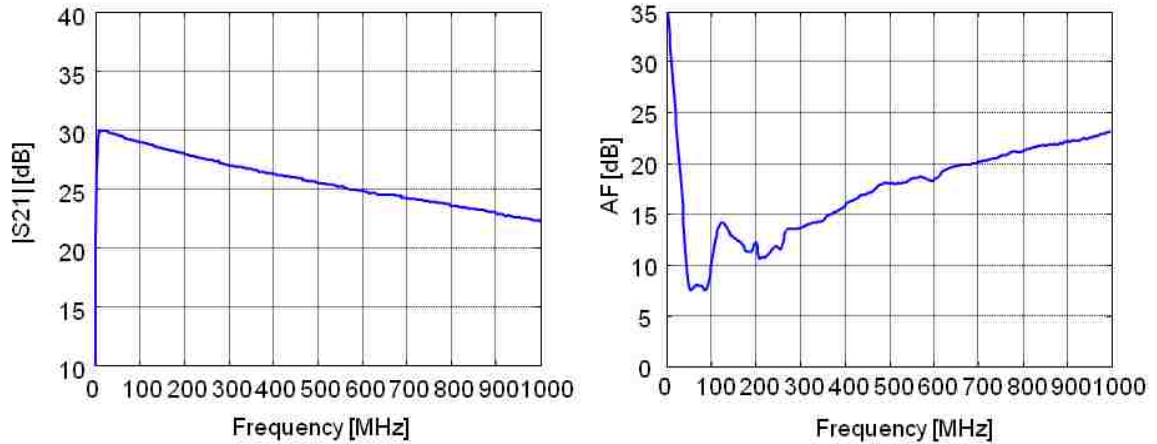


Fig. 3.9 Gain of the measurement setup and antenna factor.

The measured electric fields in both the y and z directions are compared with those calculated from the extracted dipole moments in Fig. 3.10. The peak values of the radiated fields at the harmonic clock frequencies match well for the electric field in the z direction. However, the values of the electric field in the y direction from the TEM cell measurements are smaller than the noise floor in the far-field measurements. When the radiated levels are low, there's no enough signal to noise ratio in the far-field measurements to achieve meaningful comparisons. Nevertheless, when the radiated levels exceed the noise floor of the far-field measurement, the obvious agreements at the peaks validate the proposed IC emission model.

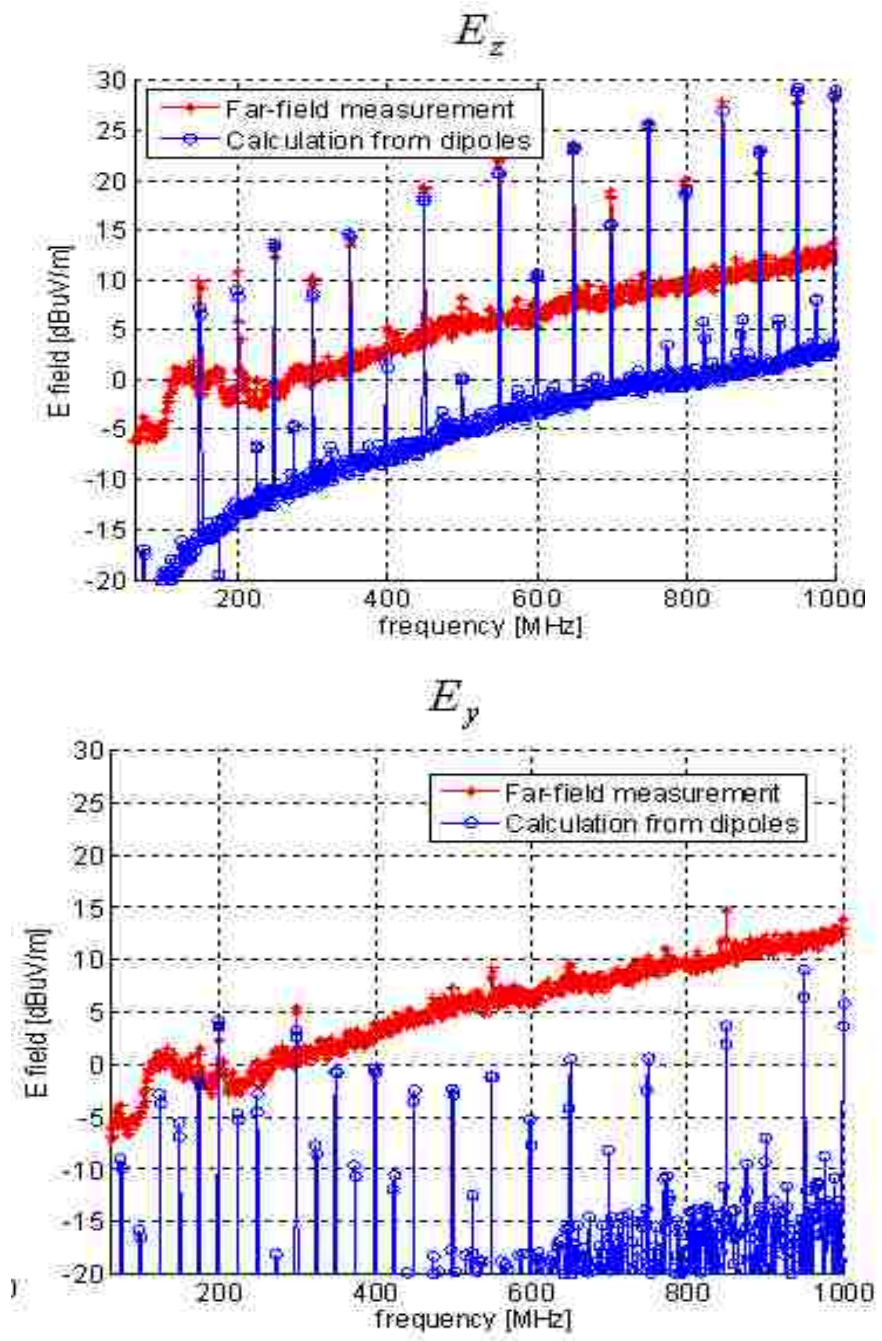


Fig. 3.10 Comparisons of the radiated fields from measurements with those calculated from the extract IC emission model.

**3.2.4. Incorporating Dipole Models into HFSS Modeling.** In complex geometries, analytical expressions of the radiated fields from the equivalent dipole moments may not be available. It is necessary to develop an approach to incorporate the extracted dipole moments as sources in common commercial full-wave electromagnetic tools so that system-level EMI problems can be investigated.

The ideal infinitesimal electric dipole can be approximated using a short wire antenna as shown in Fig. 3.11. The current excitation is at the middle of the wire. Since the current vanishes at the two ends of the wire, the electric dipole moment of this short wire antenna can be approximated as

$$P_z = \frac{1}{2} l * I_P , \quad (3.6)$$

where  $l$  is the length of the wire; and,  $I_P$  is the magnitude of the current excitation at the middle of the wire antenna.

For ideal infinitesimal magnetic dipoles, they can be approximated as loop antennas as shown in Fig. 3.12. The direction of the current in the loop and the direction of the magnetic dipole moment follow the right-hand rule. The magnetic dipole moment of the small loop antenna can be approximated as

$$M_x = A * I_M , \quad (3.7)$$

where  $A$  is the area of the loop; and,  $I_M$  is the magnitude of the current excitation in the loop.

The extracted dipole moments from the TEM cell measurements can then be incorporated in full-wave tools as the wire and loop antennas. One intuitive solution is to incorporate each dipole moment individually as an antenna source. Then the totally radiated fields generated from the IC can be calculated by adding the three sets of the simulated fields from the individual dipole moments, according to superposition. Using this approach, obviously three full-wave simulations are needed to get the total radiated fields, which is undesirable since typical system-level simulations could be complex and time-consuming.

An improved method is to combine the three antennas in one full-wave simulation as shown in Fig. 3.13. The trick is to assign two current sources to each antenna, forcing the exact current distributions so that the dipole moments can still be estimated using (6)

and (7). Notice that there exists multiple scattering among the antenna structures in this case, which could be a potential source of error.

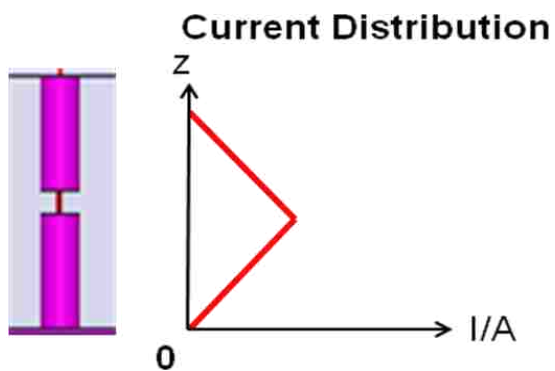


Fig. 3.11 Electric dipole approximated with a short wire antenna.



Fig. 3.12 Magnetic dipole approximated with a small loop antenna.

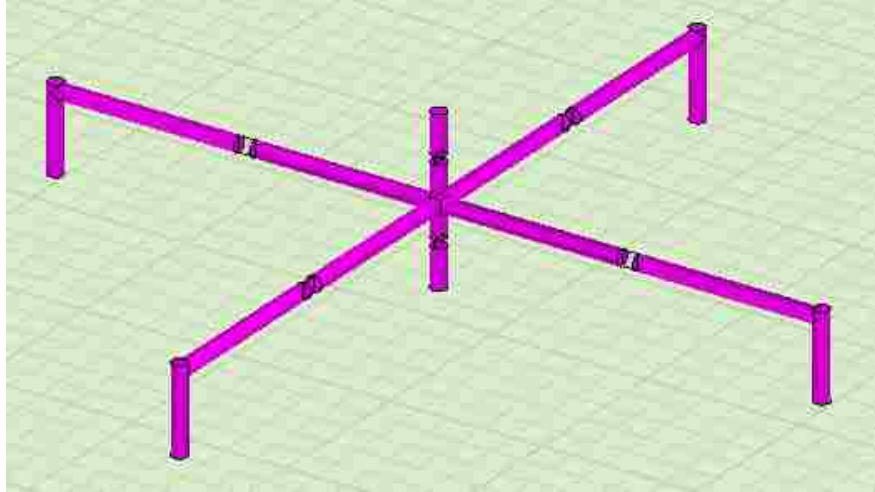


Fig. 3.13 A combined source with one wire antenna and two loop antennas.

To illustrate and validate the proposed method of using the combined antennas in full-wave electromagnetic tools, HFSS (High Frequency Structure Simulator) from Ansoft was used to show an example. Suppose the extracted dipole moments are  $M_x = 2.5e-6 \text{ Am}^2$ ,  $M_y = 2.5e-6 \text{ Am}^2$ , and  $P_z = 2.5e-4 \text{ Am}$ , and they are located on top of an infinitely-large ground plane. In the HFSS model, the areas of the loop antennas were chosen as  $2.5e-6 \text{ m}^2$ , and the length of the wire antenna as  $1e-3 \text{ m}$ . The current excitations were then  $1 \text{ A}$  in the loop antennas and  $0.5 \text{ A}$  in the wire antenna. The distance between the source and observation points was set to be  $145 \text{ mm}$ . The simulated electric field results in the  $x$  direction using the superposition approach, the combined antenna approach, and the analytic expressions are compared in Fig. 3.14. They agree very well in the frequency range of interest from  $10 \text{ MHz}$  to  $1 \text{ GHz}$ .

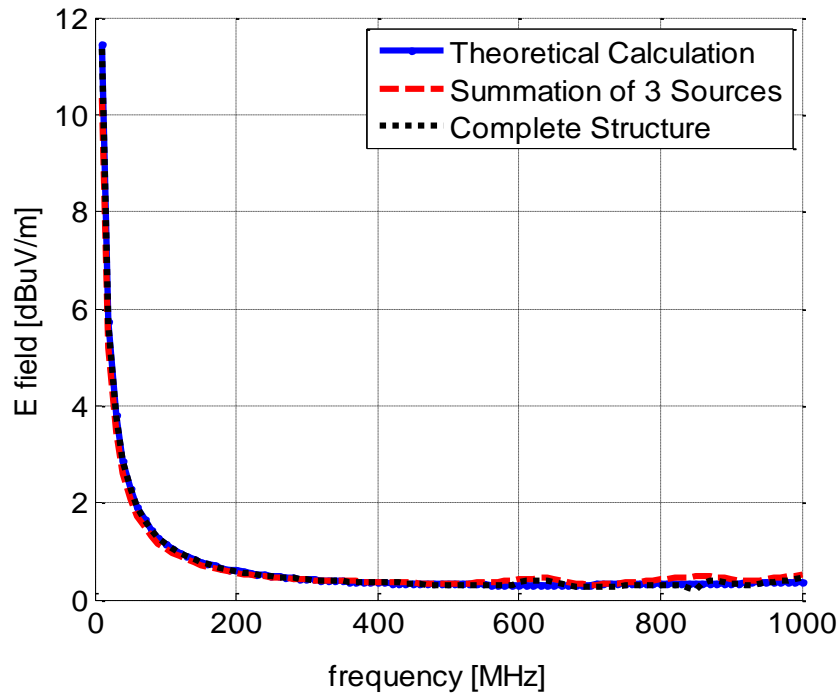


Fig. 3.14 Comparison of the radiated electric field results between analytical calculations and HFSS simulations.

### 3.3 CONDUCTED EMISSION MODEL FROM THE 1/150 OHM METHOD

In order to characterize the sources of conductive emission of an IC, two kinds of current are important to model or measure: 1) current at power supply and ground pins. 2) current at IC I/O pins. In Section 3.3, we first present two detailed methods to measure conductive current at power and ground pins. Then we proposed an equivalent circuit model for I/O current source. Validations and comparisons for the proposed methods have been done through a test board, with detailed information presented as the last portion of Section 3.3.

**3.3.1 Method Overview, Details, Key Issues.** This report focuses on two measurement methods employed in evaluating IC conductive current at power and ground pins. As shown in Fig. 3.15, in actual digital ICs, RF currents are represented by

pulsed currents absorbed by core circuits and by output driver circuits. The emission is due to the operation of ICs in a wide frequency range; therefore, the measurement methods adopted for the evaluation of IC conducted emission require the measurement of wideband RF currents.

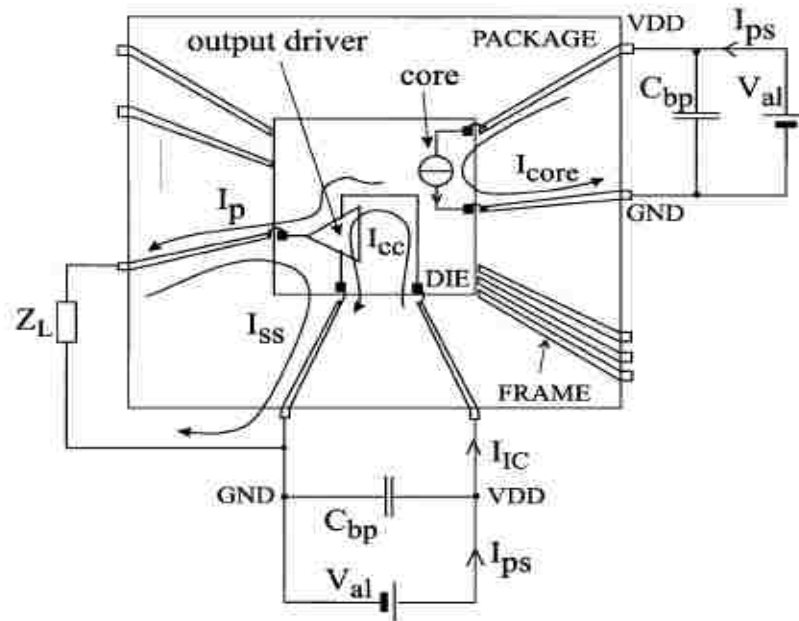


Fig. 3.15 Illustration of Power and GND current that needs to be measured.

In particular, two measurement methods, namely 1- $\Omega$  Method and Magnetic Probe Method, to estimate IC power supply conducted emissions are critically assessed and results of measurements carried out on a device under test (DUT) are compared.

IEC standard 61967-4 presents details about 1- $\Omega$  Method to measure the IC return current at GND pins. Basically, the 1- $\Omega$  method requires the spectral measurement of all ground currents, as shown in Fig. 3.15, flowing in PCB power supply network. To achieve this purpose, all IC ground pins are connected together by a low impedance metal

interconnection and the sum of all currents pushed by IC output drivers or flowing in PCB power supply networks is collected in a 1- resistive current probe.

Figure 3.16 shows the test setup employed to perform such a measurement. In particular, one terminal of the 1- $\Omega$  resistor of the current probe is connected to the IC-GND and the other terminal is connected to the test board ground net, i.e. peripheral ground. The measurement of the voltage drop across the 1- $\Omega$  resistor is performed by a spectrum analyzer connected as shown in Fig. 3.16 while a schematic description of the 1- $\Omega$  current probe is shown in Fig. 3.17. The values  $R_p$  and  $R_A$  in Fig. 3.17 are 1  $\Omega$  and 49  $\Omega$ , respectively. It also consists of a 50- $\Omega$  coaxial cable which is matched at one end by the input impedance of the spectrum analyzer and at the other end by 50- $\Omega$  resistance. The spectrum analyzer is protected against dc current by the decoupling capacitor  $C_{sa}$ . However, in reality, many instruments do not require a impedance matching network for measurement. For those cases, a resistor with value of 1  $\Omega$  inserted in the current return path is efficient.

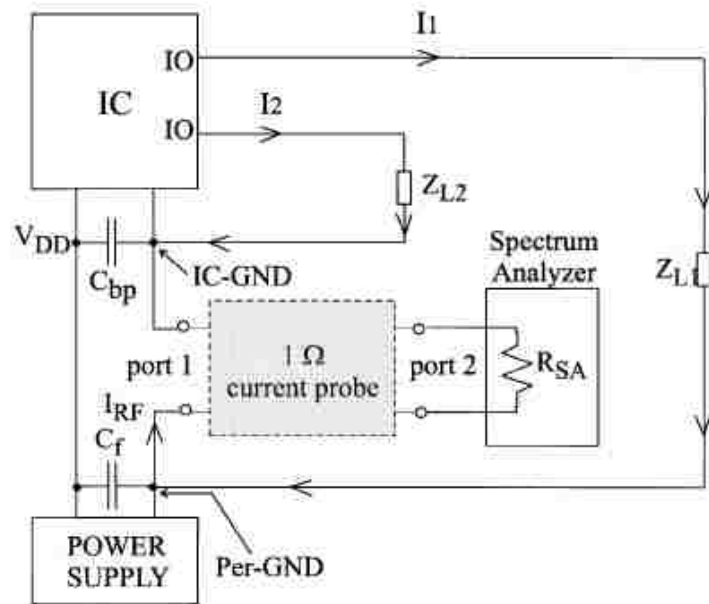


Fig. 3.16 Configuration of 1- $\Omega$  Probe Method.



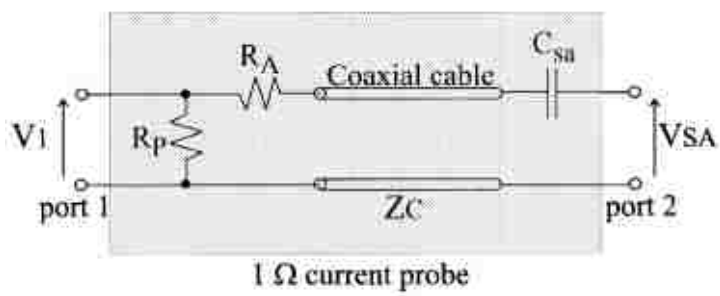


Fig. 3.17 Schematics of 1-Ω Probe in IEC 61967.

The most critical issue for design this kind of 1-Ω probe is to control its parasitic inductance. It is obvious that the large parasitic inductance will cause inaccurate measurement results when frequency is in the range of MHz. In order to minimize the parasitic inductance associated with loop of the probe, special circular-shape 1-Ω probes are designed, as shown in Fig. 3.18. There are 20 resistors in parallel. The resistance value for each resistor is 20 Ohms, so the total resistance value is 1 Ohm. The total parasitic inductance of the probe is also only 1/20 compared to a single 1-Ω resistor with the same package. The red pads on the right Fig. 3.18 are the footprints for surface-mount connectors.

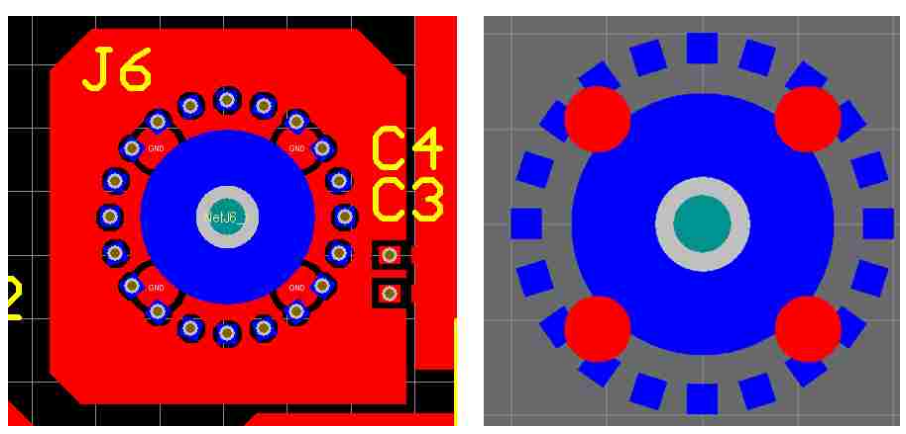


Fig. 3.18 Footprint of the 1-Ω probe with special circular-shape.

In practice, the overall structure composed by the magnetic probe and the PCB trace, behaves like an RF transformer. The primary winding of this RF transformer is the loop composed of a microstrip line driven by an IC port (a power supply pin or an output driver) and loaded by a filtering capacitor or a matching network, depending if a power supply or a signal line is considered. The secondary winding is the loop of the magnetic field probe. A schematic circuit of the test setup is shown in Fig. 3.19.

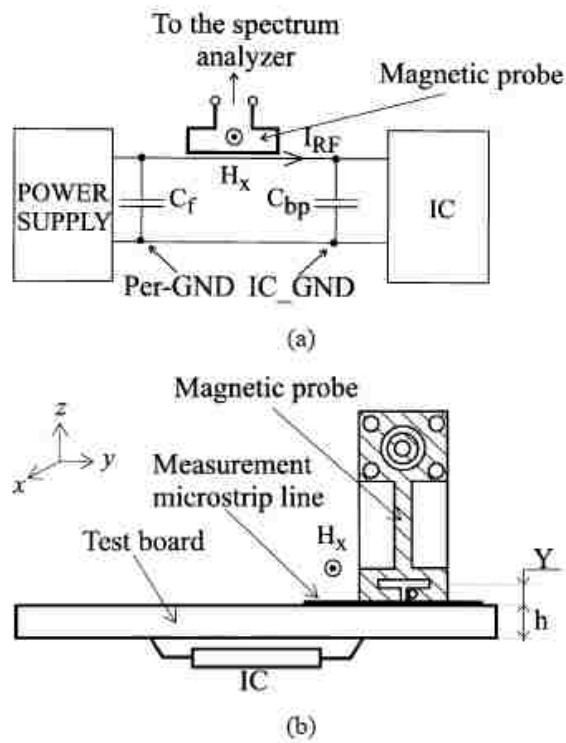


Fig. 3.19 Current probe with test board (a) test setup of the current probe (b) cross section

The magnitude of the current spectrum flowing in the primary winding is derived from the measurement of the voltage at the output port of the secondary winding, loaded by the input impedance of the spectrum analyzer. In practice, the magnetic probe output

signal is measured by the cascade of a wide bandwidth low noise amplifier and a spectrum analyzer.

In practice, the overall structure composed by the magnetic probe and the PCB trace, behaves like an RF transformer. The primary winding of this RF transformer is the loop composed of a microstrip line driven by an IC port (a power supply pin or an output driver) and loaded by a filtering capacitor or a matching network, depending if a power supply or a signal line is considered. The secondary winding is the loop of the magnetic field probe. A schematic circuit of the test setup is shown in Fig. 3.19. The magnitude of the current spectrum flowing in the primary winding is derived from the measurement of the voltage at the output port of the secondary winding, loaded by the input impedance of the spectrum analyzer. In practice, the magnetic probe output signal is measured by the cascade of a wide bandwidth low noise amplifier and a spectrum analyzer.

If time-domain signal is measured by oscilloscope connected with current probe, de-convolution technique is needed to calibrate the measured signal. The deconvolution function takes the induced probe voltage (V) as input data, and output the deconvoluted H-field strength (A/m) data.

The characteristics of the probe are captured by measuring the S11 and S21 parameters using a network analyzer. The S11 parameter shows the loss along the probe cable as a function of frequency. The cable loss is captured by the S11 parameter divided by two. One has to divide the linear S11 by two, as the wave has to travel along the cable twice to return to the NWA. The S21 parameter shows the sensitivity of the probe. Holding the probe on a 50 Ohm trace can give the effective frequency range of the probe. The frequency range is expected to go up to 3~5 GHz.

The setup that measures S11 of the probe is shown in Fig. 3.20.

The probe is placed in the air so that no H-field couples into it. The calibration is done on the SMA connector so that the S11 parameter only represents the cable loss effect of the probe and the inductance of the probe.

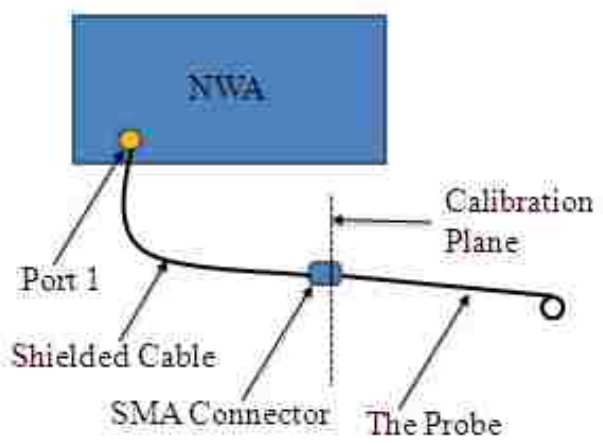


Fig. 3.20 Experimental setup for measuring  $S_{11}$  of the probe using a network analyzer.

The setup that measures  $S_{21}$  of the probe by holding the probe above a 50 Ohm trace is shown in Fig. 3.21.

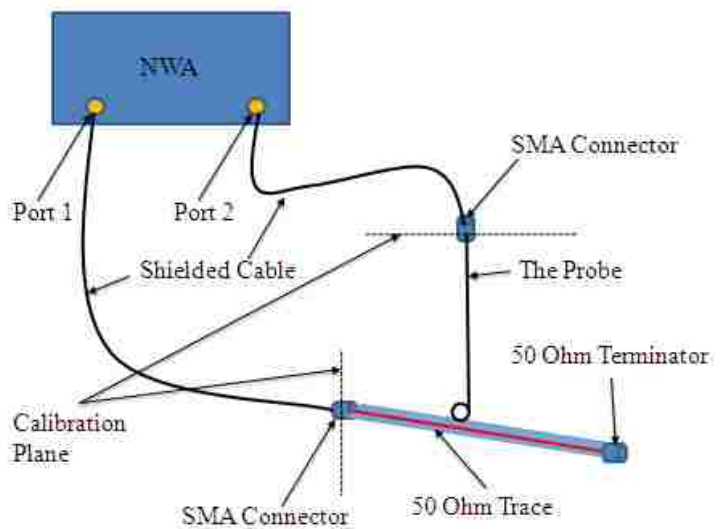


Fig. 3.21 Experimental setup for measuring  $S_{21}$  of the probe using a trace and a network analyzer.

This measurement result gives the effective frequency range of the probe. The calibration plane is shown in the Figure

The measured S11 result is shown in Fig. 3.22. We see that as the frequency goes up, the cable loss increases. The S11 should be divided by two to represent the cable loss as the signal travels through the cable twice.

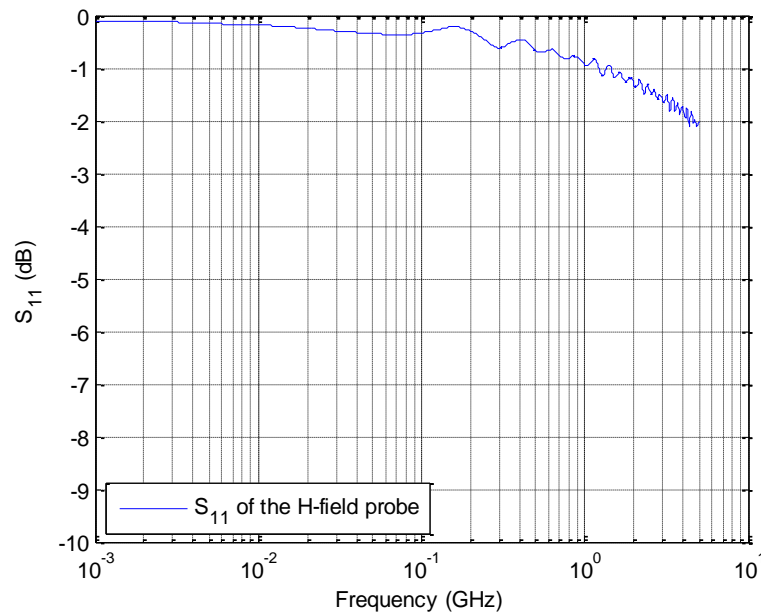


Fig. 3.22 Measured S11 result of the probe

The measured S21 result using a 50 Ohm trace is shown in Fig. 3.23.

Below 10 MHz the noise from the network analyzer couples into the signal. From 10 MHz to about 500 MHz of frequency is the linear range of the probe. The S21 follows a 20 dB/dec slope here. Above 500 MHz the effect of self-inductance and cable loss of the probe starts to be important. The S21 curve starts to bend and goes to flat. We can see that the frequency range of the probe goes up to about 5 GHz without any resonances.

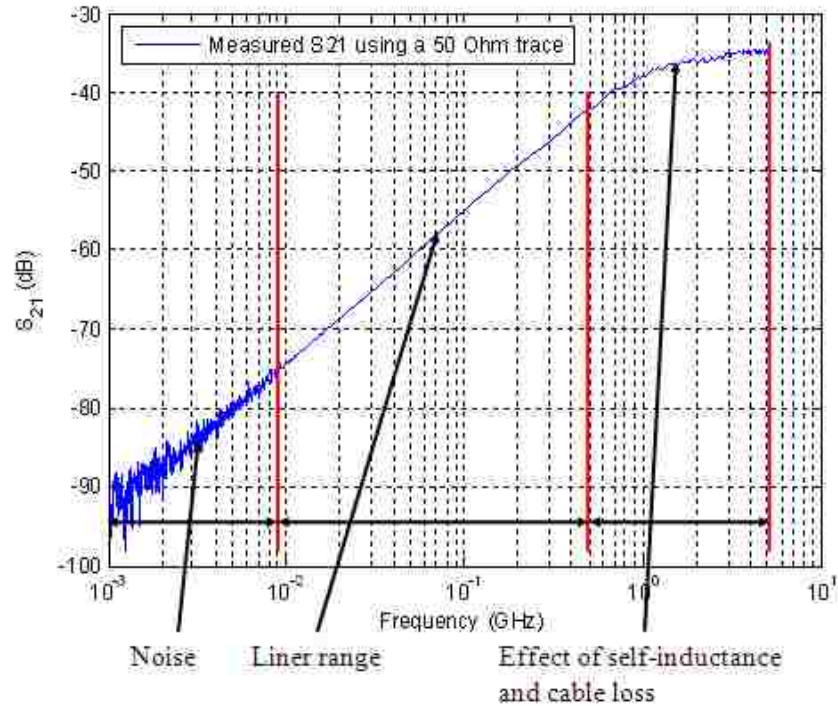


Fig. 3.23 Measured frequency response using a 50 Ohm trace

To fulfill the deconvolution function, a mathematical model that represents the measured frequency response of the probe is needed. A SPICE equivalent circuit that can represent the measured S21 is shown in Fig. 3.24.

The probe is made by soldering the inner conductor of a coax cable to its outer conductor. The inner wire forms a loop which can be modeled as an inductor. The diameter of the loop is about 3 mm, so the loop inductance is calculated as about 6 nH. The cable loss effect is not taken into account here. The 10 pF inductor and the 50 Ohm terminate represents the trace and the 50 Ohm terminator that we are using. The trace and the probe are coupled by mutual inductance.

Properly modifying the coupling parameter of the mutual inductance, this model can give the result of measurement setup “probe above trace”. The comparison between simulated S21 and measured S21 is shown in Fig. 3.25.

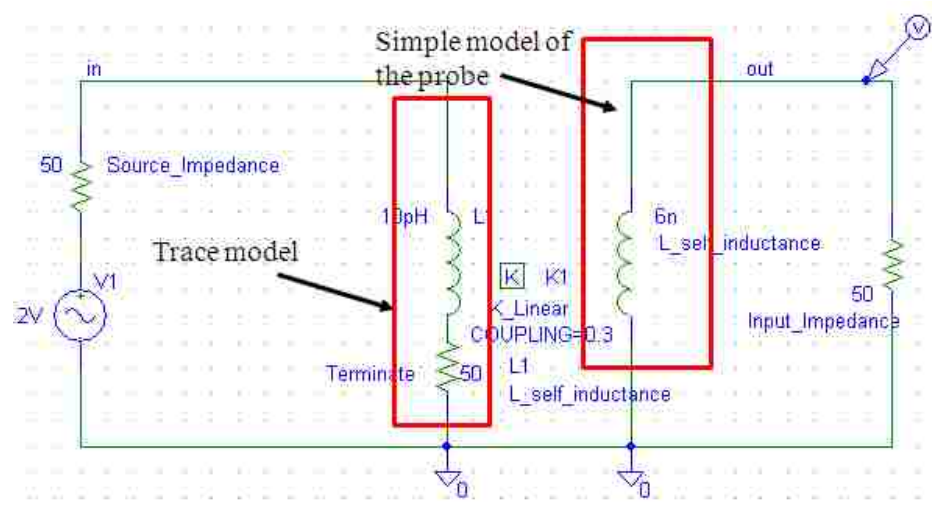


Fig. 3.24 An equivalent circuit of the H-field probe

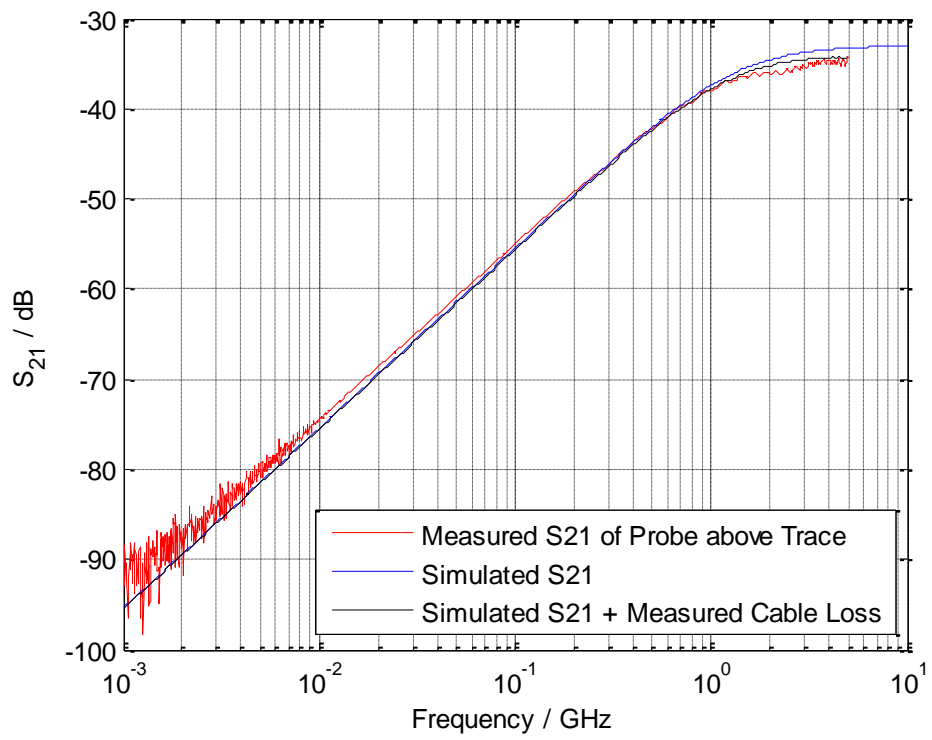


Fig. 3.25 Comparison of S21 between “probe above trace” measured result and SPICE model result

To fulfill the deconvolution function of the H-field probe, the process can be done in steps shown below.

Step 1: Perform data validity tests on the measured data by doing some checking on them (length of data, time step etc.).

Step 2: Re-map the time domain data onto a new time axis. Fill the original data with zeros in the end, make the length of data to be  $2^{18}$  for preparation of FFT. This is done for increasing the frequency resolution.

Step 3: FFT.

Step 4: Multiply with the inverse frequency response. Add a high pass filter at  $f_{\text{lower}}$  to avoid noise data from signals below  $f_{\text{lower}}$ . Here  $f_{\text{lower}}$  is the frequency below which the noise of NWA affects the measured signal significantly. The  $f_{\text{lower}}$  here is 5 MHz.

Step 5: Add a low pass filter at  $f_{\text{upper}}$  to avoid nonsense data from signals above  $f_{\text{upper}}$ . Here  $f_{\text{upper}}$  is the frequency above which the resonance occurs. The  $f_{\text{upper}}$  here is set as 5 GHz based on the probe characteristics.

Step 6: IFFT.

Step 7: remapping on original time axis.

Step 8: Conversion from de-convoluted voltage to field strength in [A/m].

A flow chart of this function is shown in Fig. 3.26.

The steps in the red block show how the compensation network was generated and how to get the impulse response from the compensation function. The step in the green block shows the deconvolution concept. The multiplication of two sets of frequency domain data equals to the convolution in time domain of these two sets of data.

If using current probe connecting with spectrum analyzer, calibration is still needed. All the procedures are the similar as the flow chart shown in Fig. 3.26. Using the same setup in Fig. 3.21,  $S_{21}$  of the probe in frequency domain is obtained, which is the probe factor between original and measured data.



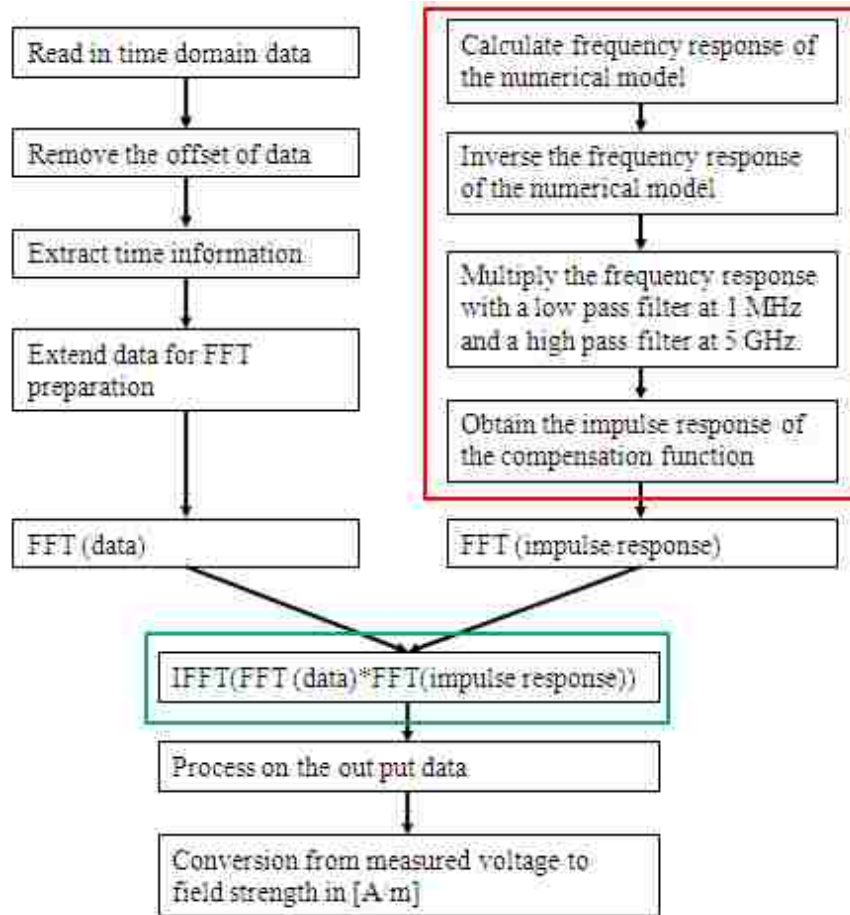


Fig. 3.26 Flow chart of the deconvolution function.

Noise at I/O pins of the IC is usually hard to model by analyzing the electric behavior of the circuit inside IC, due to the complexity and unknown characters. However, a Thevenin equivalent source model can be built by measuring the conductive current at I/O pins with different load conditions.

IEC 61967-6 shows the noise voltage at I/O pins can be replaced by the circuit model in Fig. 3.27. The cabling network can be represented in most cases by an antenna with an impedance of  $150\ \Omega$ . Most instruments has an input impedance of 50 Ohms, which will behave similarly as a receiver.

A Thevenin equivalent source model for noise voltage at I/O pins is shown in the Fig. 3.28.  $V(f)$  represents equivalent noise voltage and  $Z(f)$  represents source impedance. There are 3 unknown parameters in this equivalent circuit model: source voltage, real and

imaginary part of the source impedance. Therefore, 3 measurements are needed to solve the circuit parameters. If we measure the voltages at I/O pins with 3 different load condition, all the unknown circuit parameters can be solved, as

$$\begin{aligned}
 V_s &= V_{open} \\
 V_{l1} &= \frac{V_s}{\sqrt{(R_s^2 + L_s^2)}} * R_{l1} \\
 V_{l2} &= \frac{V_s}{\sqrt{(R_s^2 + L_s^2)}} * R_{l2}
 \end{aligned} \tag{3.9}$$

where  $V_{open}$  is the output voltage when the load is open.  $V_{l1}$  and  $V_{l2}$  are the voltages measured at output pin when the load is purely resistive and the value is  $R_{l1}$  and  $R_{l2}$ , respectively.

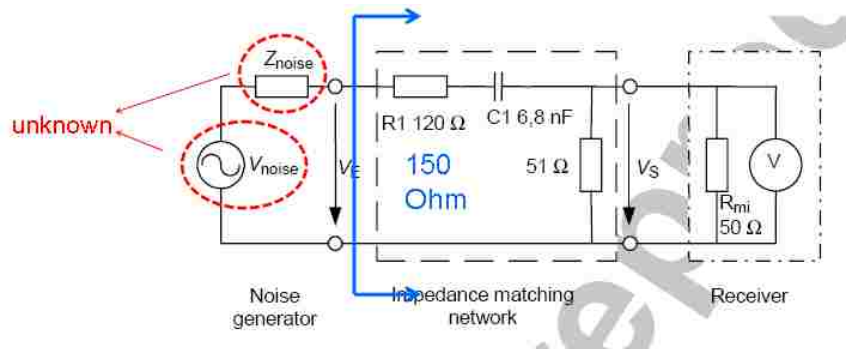


Fig. 3.27 Equivalent circuit model with cabling network.

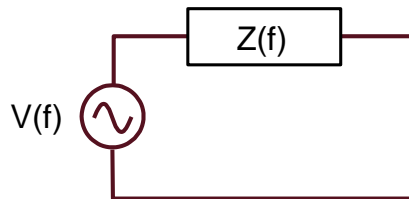


Fig. 3.28 Thevenin equivalent source model for noise voltage at I/O pins.

**3.3.2. Test Board Design.** A test board is designed to validate the models and measurement methods proposed previously. The IC we measured is a LOCO™ PLL Clock multiplier made by IDT. The schematics of the test board are shown in Fig. 3.29. The headers P1 and P2 are used to adjust the operational frequency of PLL. The PLL is driven by an oscillator (ECS-3951M) of 25 MHz. The output power for both PLL and oscillator is 5V. Pin 3 of PLL IC is its ground pin. We used 1- $\Omega$  method and current probe method to measure the return current at Pin 3. Meanwhile, we measured current I/O pin (Pin 5) using active probe with different loading conditions. Because in the equivalent circuit model, 3 unknowns need to be solved: source voltage, real and imaginary parts of the source impedance, the load needs to change 3 times with different value to construct I/O pin equivalent circuit model. Open, 11 ohm and 22 Ohms are used as three load conditions.

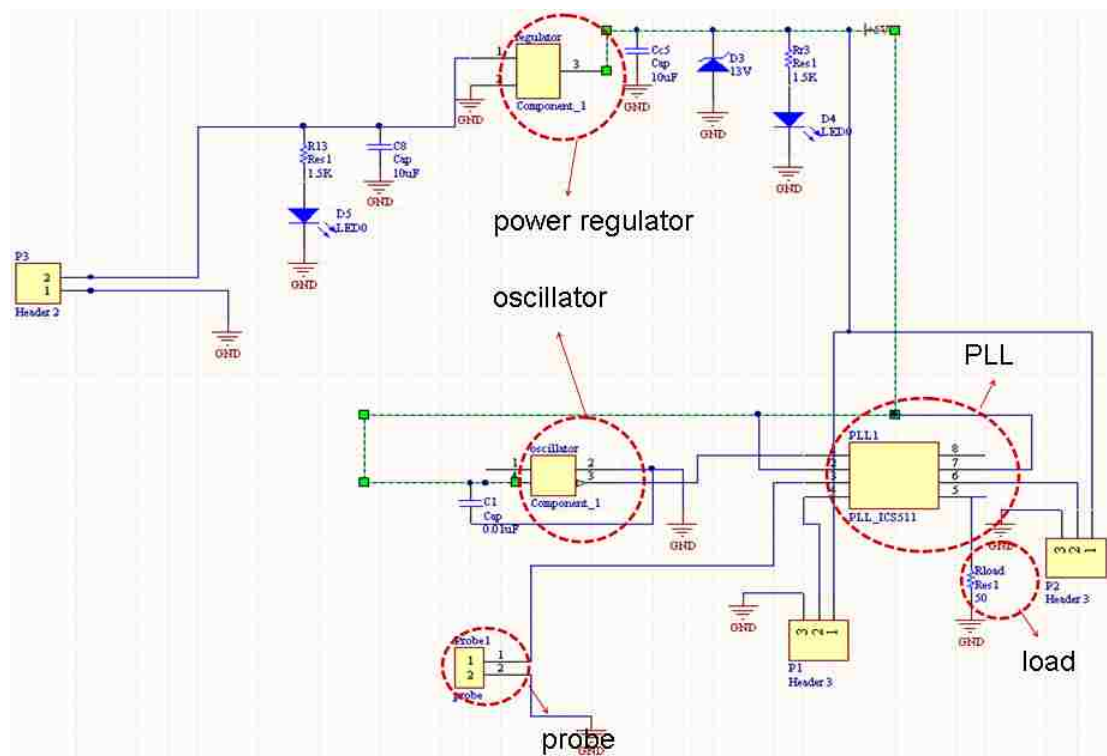


Fig. 3.29 Schematics of the test board for IC conductive emission model and measurement.

The layout of the test board is shown in Fig. 3.30. The circular-type pads are 1- $\Omega$  probe. We used current probe to measure the current above the trace between GND pin (Pin 3) of the PLL and the 1- $\Omega$  probe. The load at I/O pin can be changed.

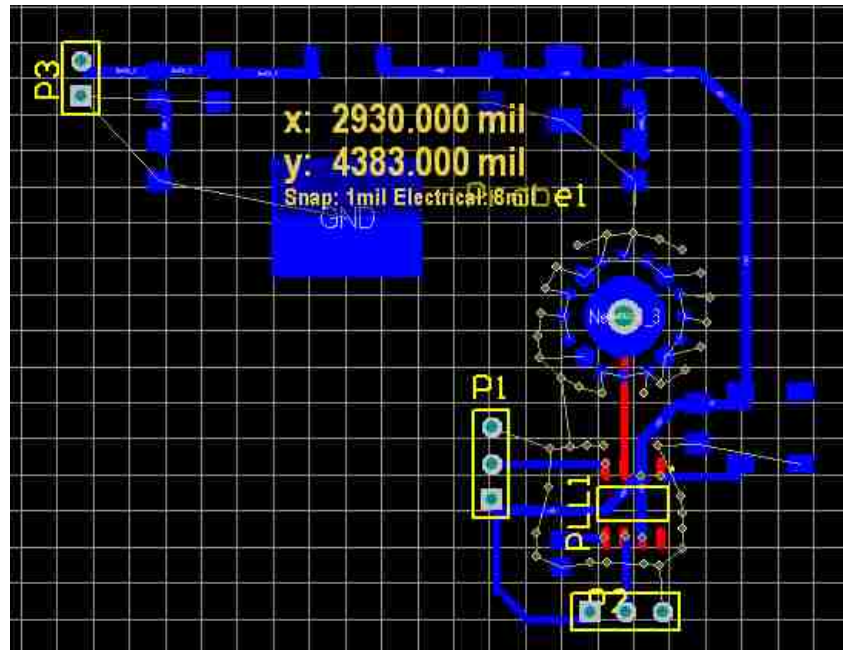


Fig. 3.30 Layout of the test board for IC conductive emission model and measurement.

**3.3.3. Test Board Measurement.** The test setup to measure the conductive current at GND pin using 1- $\Omega$  Probe Method is shown in Fig. 3.16. The current probe we use is a hand-made magnetic probe, as shown in Fig. 3.31. Ferrites are applied onto the coax cabled running inside the probe holder, but because of the space limitation, not enough ferrites were used, so external ferrites are recommended to be used too. First calibration is done by measuring the transfer impedance  $Z_{21}$  of this probe, and compared it with mutual inductive approximation of 5  $\mu\text{H}$ . The results are shown in Fig. 3.32.

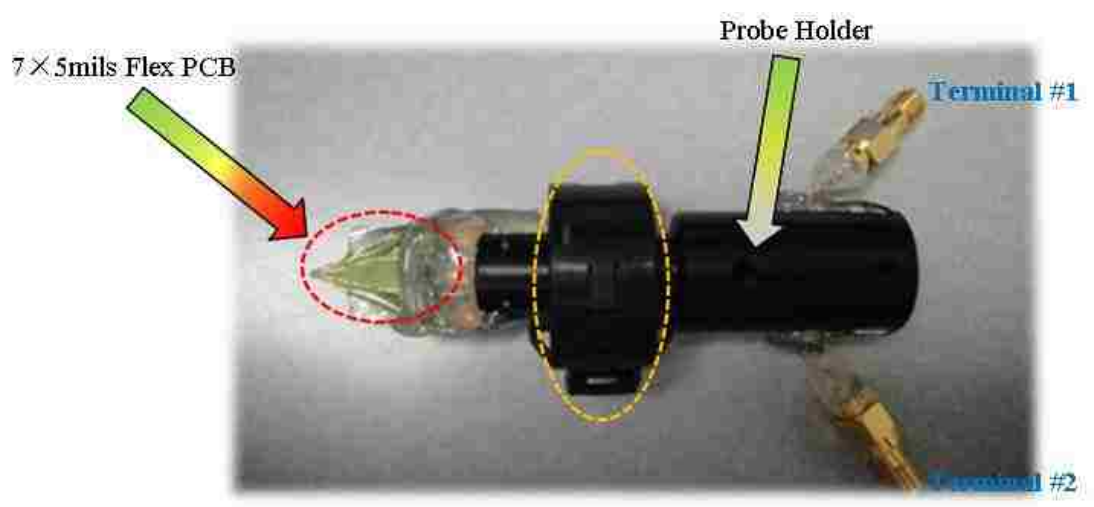


Fig. 3.31 Current probe used to measure IC conductive current.

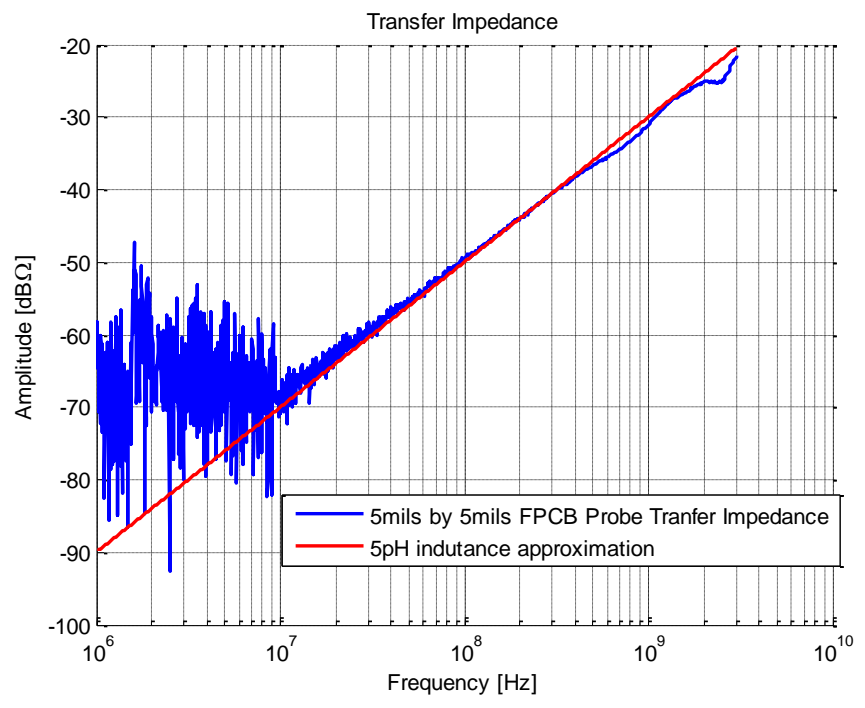


Fig. 3.32 Transfer impedance of the current probe shown in Fig. 3.31.

The results of measuring the return current at GND pin of the IC using both 1- $\Omega$  Probe and current Probe are shown in Fig. 3.33. The results of the conductive current measured by two methods agree well above -45 dBV. Because the resolution of 1- $\Omega$  Probe is low, the spectrum below -45 dBV hides into the noise.

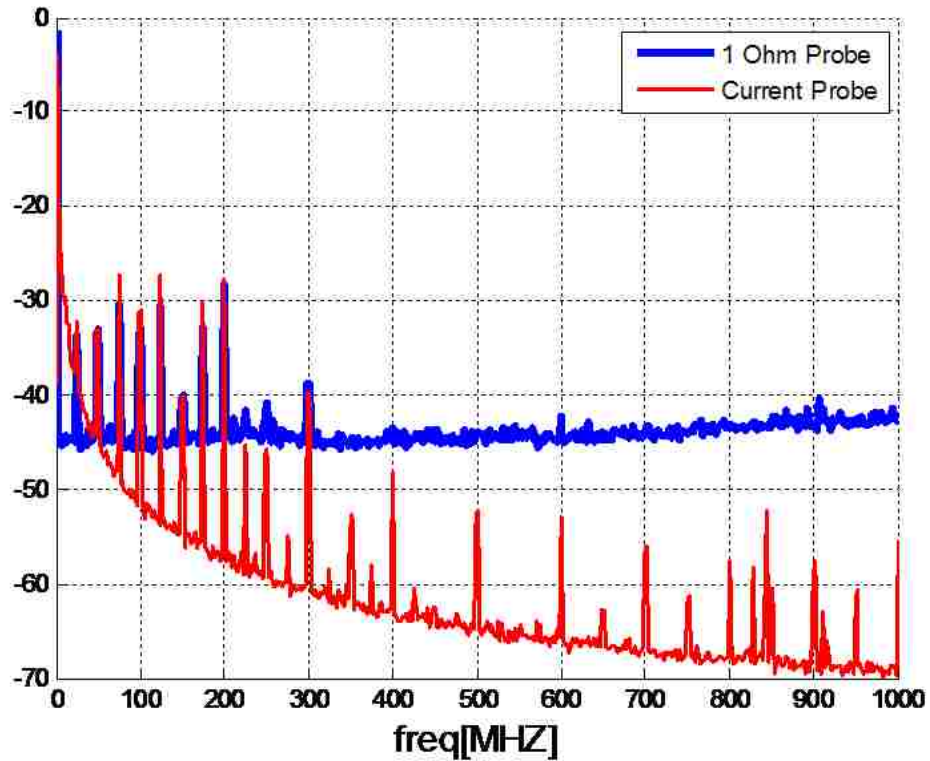


Fig. 3.33 Measurement results for the conductive current at GND pin using 1 Ohm probe and current probe.

Active probe is used to measure the current at I/O pins. The active probe we used is Agilent 1169A, with equivalent circuit model shown in Fig. 3.34.

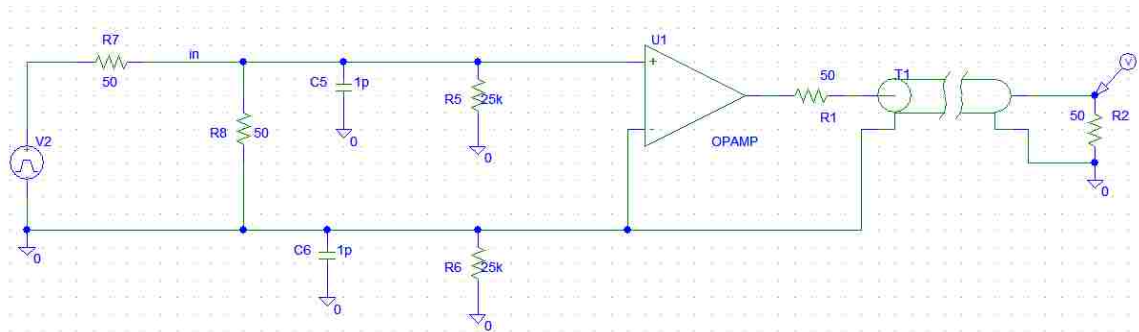


Fig. 3.34 Equivalent circuit model for active probe.

The test setup to calibrate the active probe is shown in Fig. 3.35. VNA are calibrated by thru between port 1 and 2. The frequency range is from 100 kHz to 3 GHz. Theoretically, the level of the probing results is 1/10 of the original signal. Therefore, S21 from VNA in the setup shown in Fig 3.35 should be expected to be a constant of -20dB. However, in reality, the scope that provides the power to the active probe will compensate to the probe to certain degree. The measured S21 is shown in Fig. 3.36.

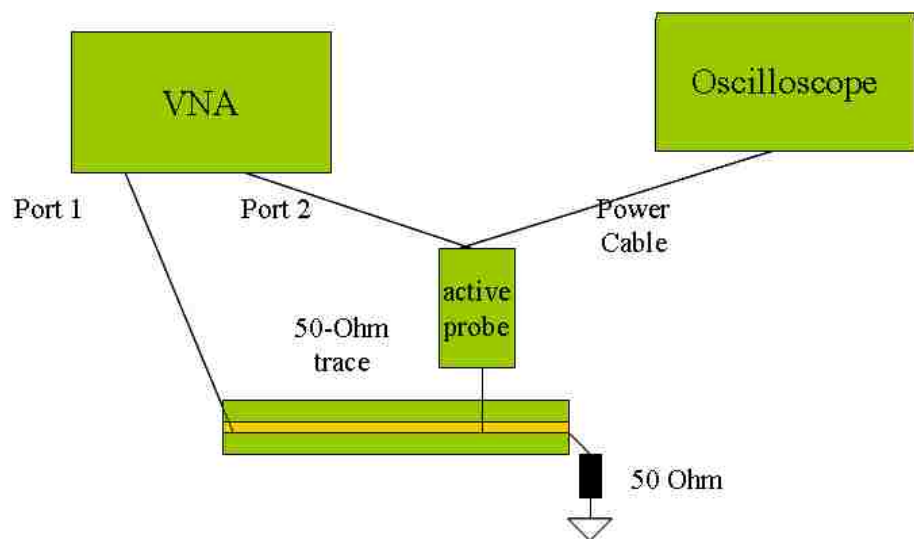


Fig. 3.35 Setup of the calibration for active probe.

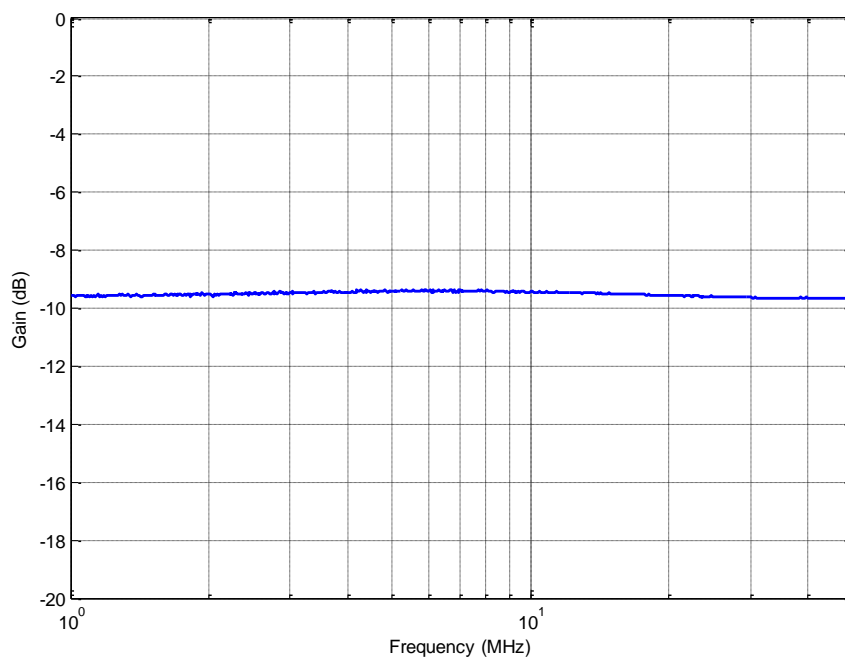


Fig. 3.36 Calibration factor (S21) of active probe.

To test the effectiveness of the active probe, a known time-domain signal was probed, and the setup is shown in Fig. 3.37.

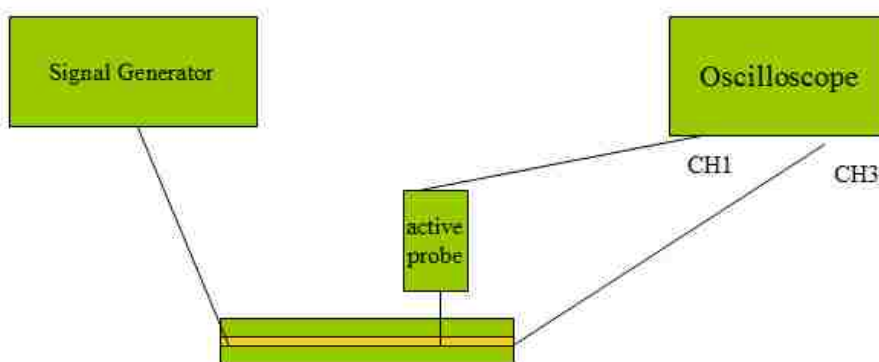


Fig. 3.37 Setup of time-domain measurement of active probe.



A signal with 30MHz periodicity is generated by signal generator. The red curve in Fig. 3.38 is the original signal directly measured from oscilloscope. And the blue curve is the measurement from active probe. The original signal is roughly 3.2 times larger than the signal from active probe. This factor (3.2) is approximately equal to the calibration factor provided from S21 shown in Fig. 3.36.

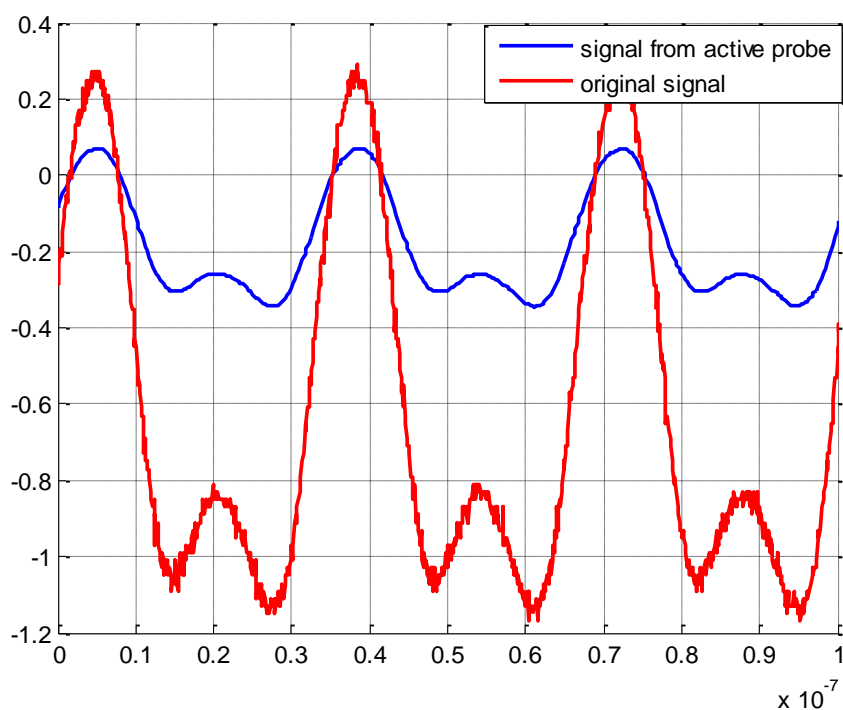


Fig. 3.38 Comparison between measured signal from active probe and original signal.

To measure the frequency-domain signal using an active probe, the setup is shown in Fig. 3.39.

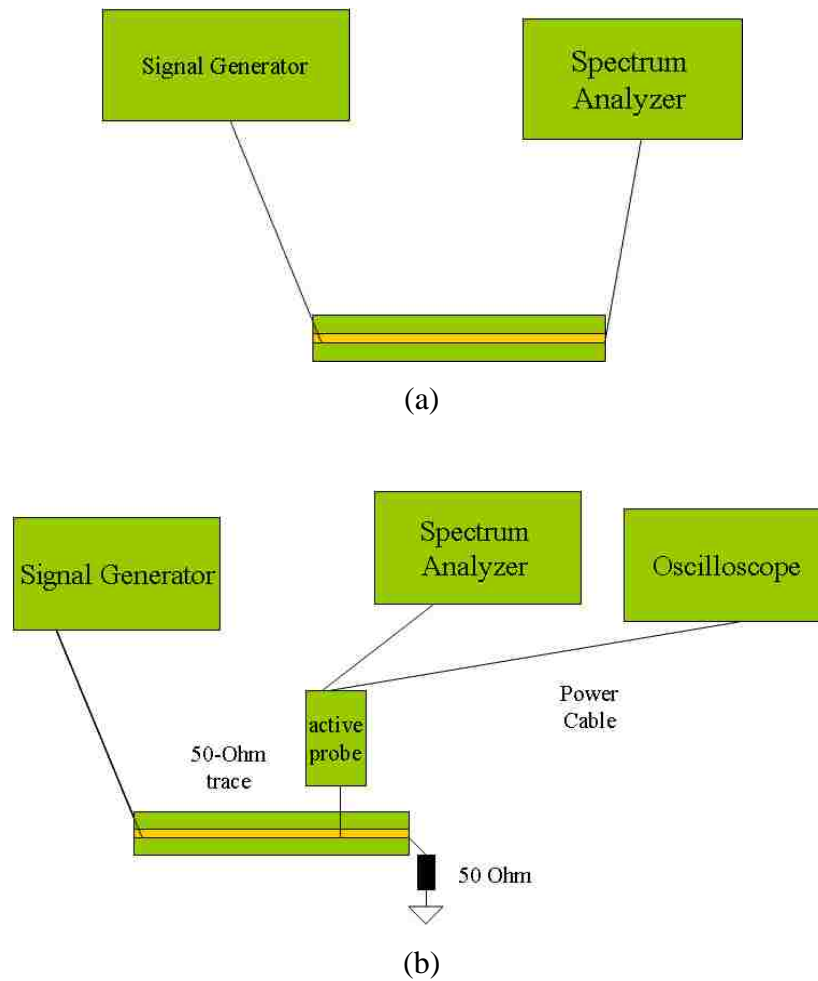


Fig. 3.39 Comparison between measured signal from active probe and original signal

The periodicity of the signal generated from signal generator is still 30MHz. Figure 3.40 shows the spectrum of the original data and data from probe. The frequency components appear at the harmonics of 30 Mhz. And the spectrum of the probed signal is approximately 10dB lower than the original signal, which validates the calibration process for the probe.

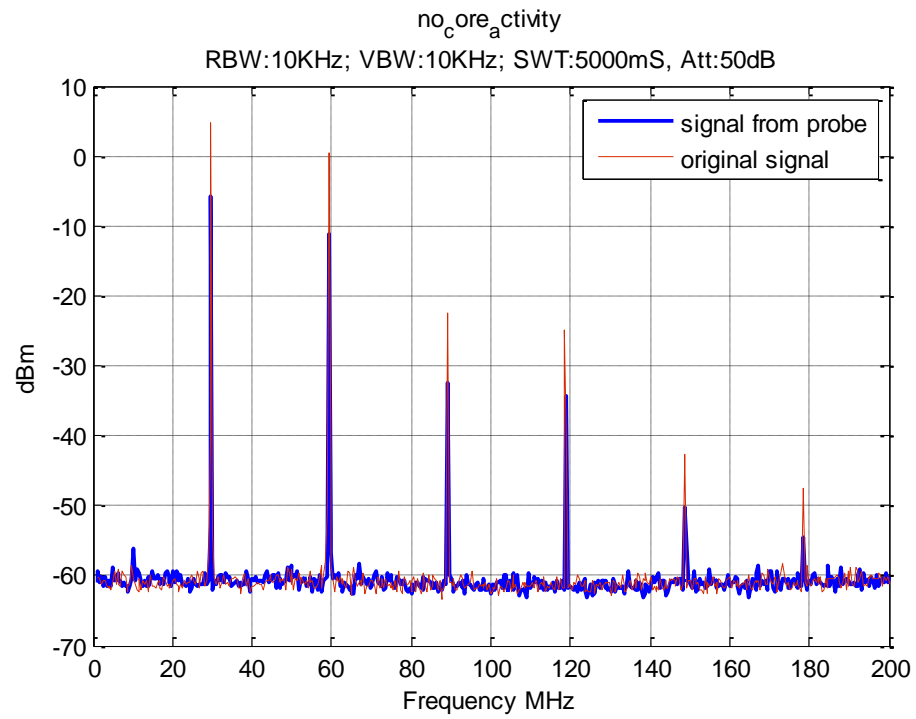


Fig. 3.40 Comparison between measured signal from active probe and original signal in frequency domain.

Active probe is used to measure the voltages at I/O pins, when the load conditions are open, 11 ohm and 22 Ohms. The voltage at I/O pin with 53-Ohm load is used for validation. The voltage waveforms measured by oscilloscope are shown in Fig. 3.41. The frequency components voltage at I/O pins are measured by a spectrum analyzer, shown in Fig. 3.42.

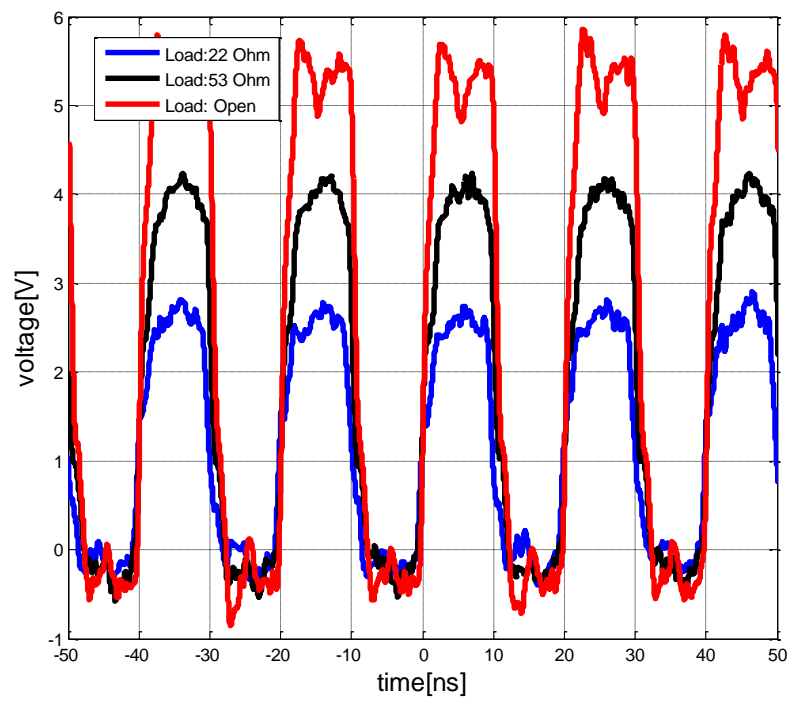


Fig. 3.41 Voltage waveform at output pin with 3 different loads.

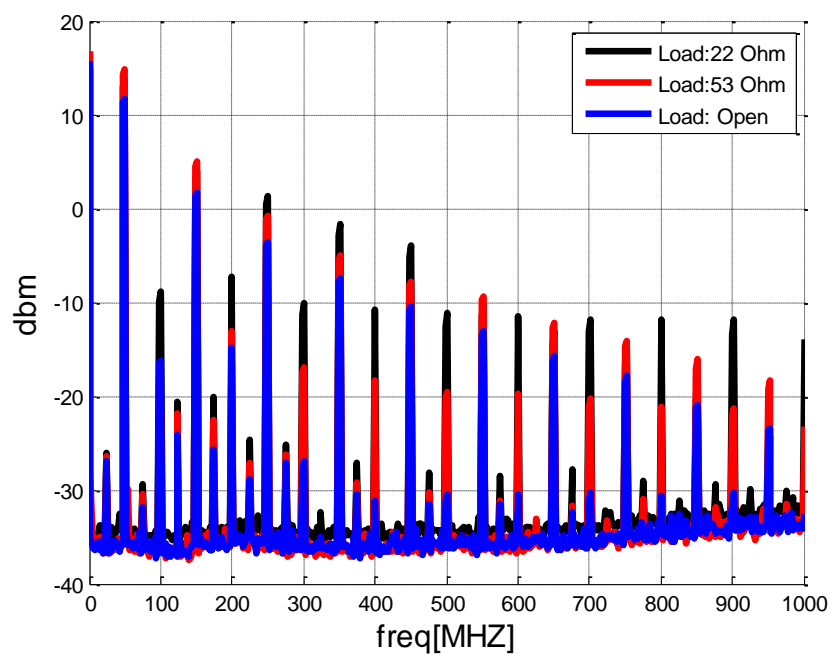


Fig. 3.42 Spectrum of the voltage at output pin with 3 different loads.

The source voltage, source resistance and inductance are calculated from equation (1) based on the measured voltages at I/O pins with 11-Ohm, 22-Ohm and open load condition. Fig. 3.43 shows the source voltage, resistance and inductance. The voltages at I/O pin are then calculated from the proposed I/O circuit model with 53-ohm load. The results from calculation and measurement are compared in Fig. 3.44.

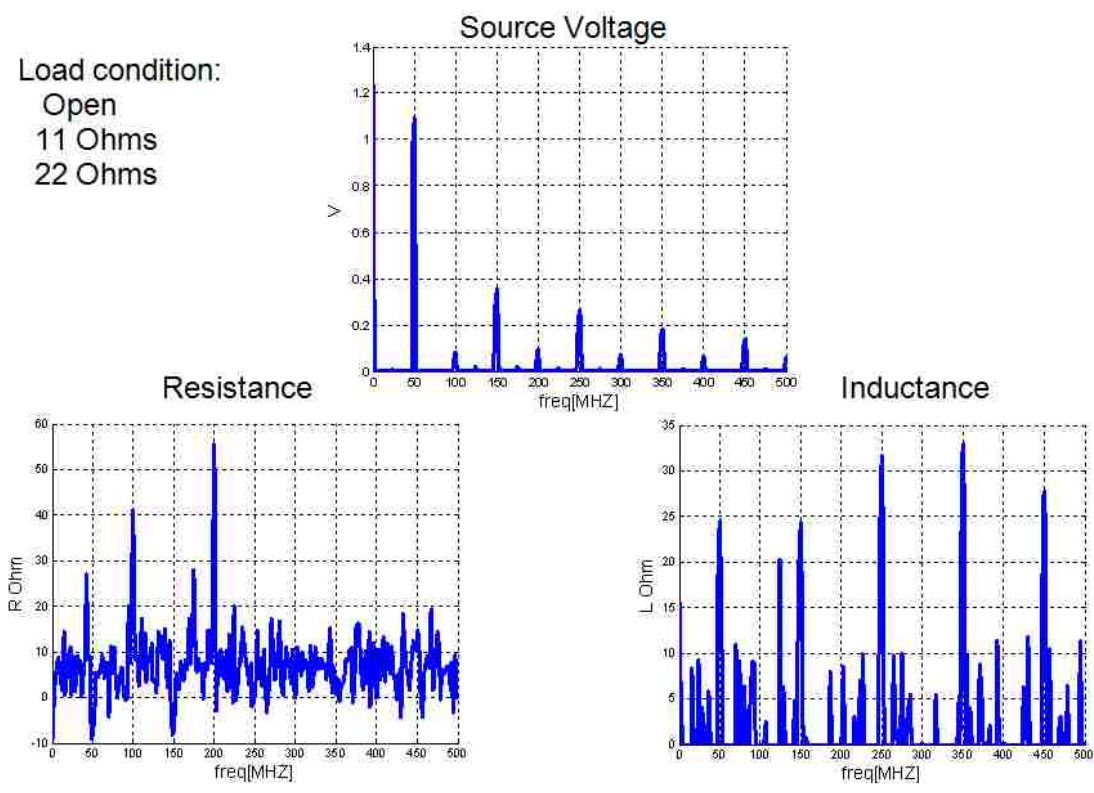


Fig. 3.43 Source voltage, resistance and inductance of the PLL IC.

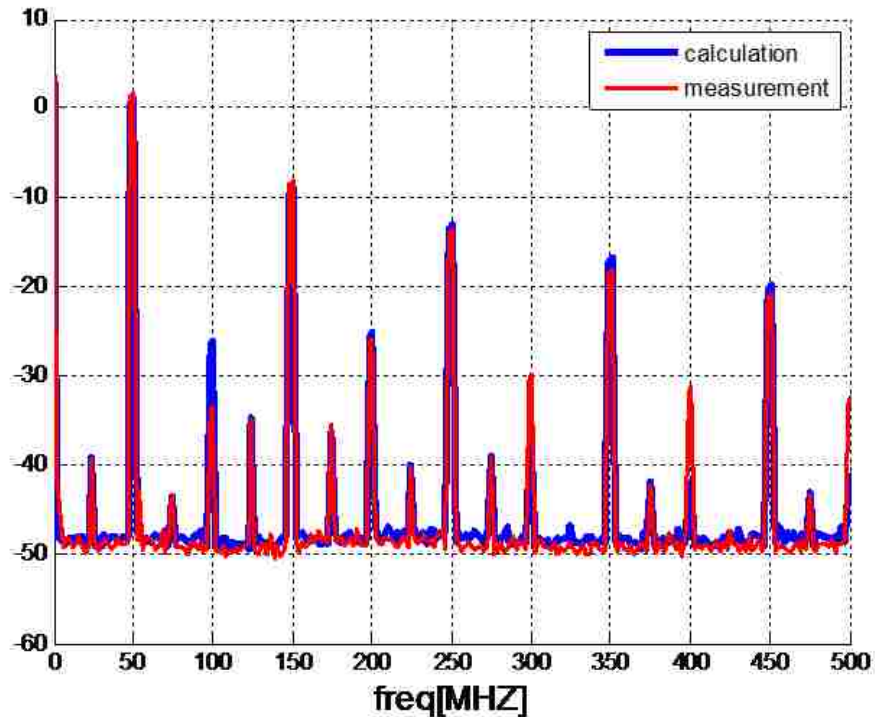


Fig. 3.44 Comparison of I/O pin voltages from calculation of the model and measurement.

### 3.4. SUMMARY AND CONCLUSIONS

1) In Section 3.2, an IC emission model has been proposed using three dipole moments ( $P_z$ ,  $M_x$ , and  $M_y$ ) extracted from TEM cell measurements. This model has been validated using the comparisons between the radiated fields calculated using the extracted dipole moments as equivalent sources and those obtained from the far-field measurements for a PLL test chip. An approach with combined loop and wire antennas to incorporate the dipole moments as sources in commercial full-wave EM tools has also been developed. The study reported in Section 3.2 has demonstrated that the radiated emissions from ICs can be well characterized using three dipole moments extracted from simple TEM cell measurements. The proposed model can accurately predict the emission level from a single isolated IC. For system-level EMI simulations, complex emission model, such as dipole arrays, need to be further studied by considering the near-field coupling in the system.

2) The sources of conductive emission of an IC are also characterized in Section 3.3. Two detailed methods to measure conductive current at power and ground pins are presented. Then we proposed an equivalent circuit model for I/O current source. Validations and comparisons for the proposed methods have been done through a test board.

## 4. LINK PATH ANALYSIS

### 4.1. INTRODUCTION OF LINK PATH ANALYSIS

To investigate a complex link path constituted by several different blocks, such as transmission lines (microstrips and striplines), via transitions, connectors, and physical discontinuities when unwanted effects are present along the path, great amount of work has been studied previously with the development of Link Path Analyzer (LPA) tool sets in the MS&T EMC lab. These individual blocks can be described in the frequency domain in terms of S-parameters. The S-parameter blocks should be checked and corrected for causality and passivity before time-domain simulations to ensure stability. These single networks also need be connected together to give the S-parameter of the overall link. The link path performances are analyzed by taking into account the signal that is going to be launched along the link; therefore the total S-parameter gives just the intrinsic properties of the medium and the characteristics of the input signal at the driver needs to be included. Some numerical procedures are developed for obtaining an eye diagram and jitter decompositions at the receiver starting from the S-parameter of the overall link path and the input signal at the driver.

This section shows the improvements of the algorithms used in the LPA tool for better generality, including cascade of S parameter blocks, causality and passivity check and enforcement for arbitrary network with any number of ports.

### 4.2. CASCADE OF S-PARAMETER BLOCKS

The cascading function used in the link path analyzer can cascade S- parameter blocks with arbitrary channel property, by adopting creative cascading algorithm. The algorithm here is different from the traditional cascading methods.

The standard employed procedure for cascading S-parameter blocks applies a conversion from S parameters to T parameters (or ABCD parameters), as shown in Fig. 4.1. However, when the channels are weakly coupled, the sub-matrices of T parameter will be small. After multiplication of T matrices, there may be problems of



singularity when converting cascaded T parameters back to S parameters. In other words, the commonly used S -T conversion always fails when the channels are weakly coupled.

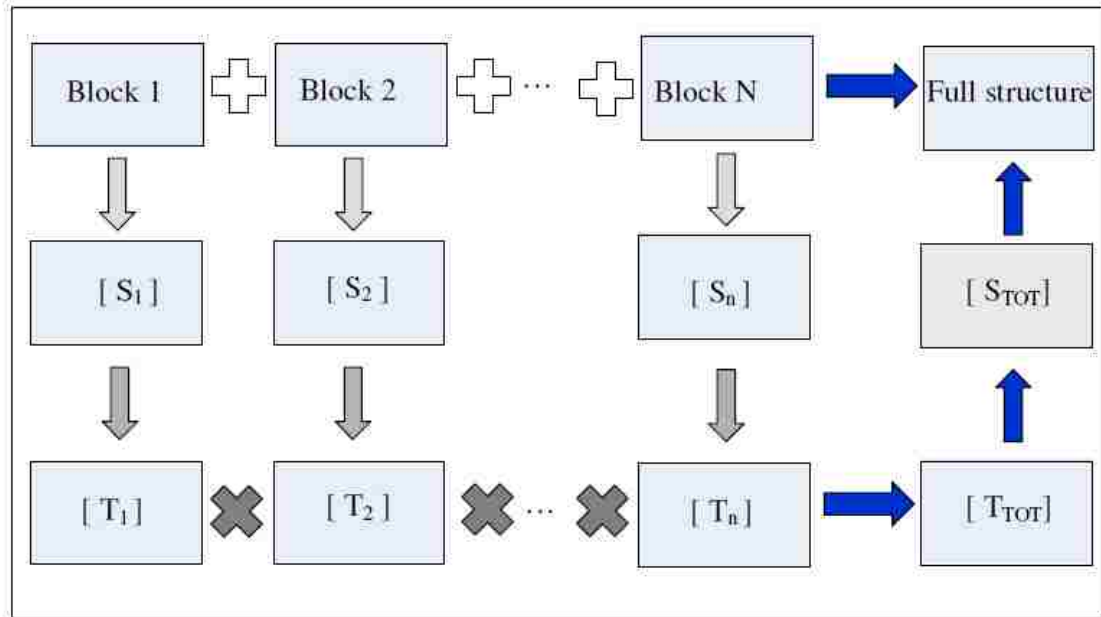


Fig. 4.1 Traditional methods for cascading S-parameter blocks.

An alternative method is proposed to cascade S-parameter blocks without S-T conversion. Suppose two n-port S-parameter blocks in Fig. 4.2 need to be cascaded. The first digit denotes the number of block, while the second digit denotes the number of its port. The S parameters for block 1 and 2 are denoted as S1 and S2, respectively.

S1 and S2 can be written as

$$\begin{bmatrix} b_{11} \\ b_{12} \\ \cdot \\ \cdot \\ \cdot \\ b_{1n} \end{bmatrix} = S_1 \begin{bmatrix} a_{11} \\ a_{12} \\ \cdot \\ \cdot \\ \cdot \\ a_{1n} \end{bmatrix} \quad \begin{bmatrix} b_{21} \\ b_{22} \\ \cdot \\ \cdot \\ \cdot \\ b_{2n} \end{bmatrix} = S_2 \begin{bmatrix} a_{21} \\ a_{22} \\ \cdot \\ \cdot \\ \cdot \\ a_{2n} \end{bmatrix} \quad (4.1)$$

The S parameter  $S_{total}$  after cascading can be written as

$$\begin{bmatrix} b_{11} \\ \cdot \\ \cdot \\ \cdot \\ b_{1(n/2)} \\ b_{2(n/2+1)} \\ \cdot \\ \cdot \\ \cdot \\ b_{2n} \end{bmatrix} = S_{total} \begin{bmatrix} a_{11} \\ \cdot \\ \cdot \\ \cdot \\ a_{1(n/2)} \\ a_{2(n/2+1)} \\ \cdot \\ \cdot \\ \cdot \\ a_{2n} \end{bmatrix} \quad (4.2)$$

Where S1 and S2 can be represented by four submatrices of  $(n/2)*(n/2)$  dimensions, as

$$S_1 = \begin{bmatrix} A_1 & B_1 \\ C_1 & D_1 \end{bmatrix} \quad S_2 = \begin{bmatrix} A_2 & B_2 \\ C_2 & D_2 \end{bmatrix} \quad (4.3)$$

It can be demonstrated (2) will be valid if  $S_{total}$  is written as

$$S_{total} = \begin{bmatrix} B_1 A_2 (I - D_1 A_2)^{-1} C_1 + A_1 & B_1 A_2 (I - D_1 A_2)^{-1} D_1 B_2 + B_1 B_2 \\ C_2 (I - D_1 A_2)^{-1} C_1 & C_2 (I - D_1 A_2)^{-1} D_1 B_2 + D_2 \end{bmatrix} \quad (4.4)$$

Equation (6) can be used to calculate S parameters after cascading two blocks. Compared to traditional methods, the conversion from S parameter to T parameter can be omitted. The new proposed method is more efficient in terms of computational time.

Moreover, when the channels are weakly coupled, the singular problems of the sub matrices can be ignored as the inversions for sub matrices are avoided.

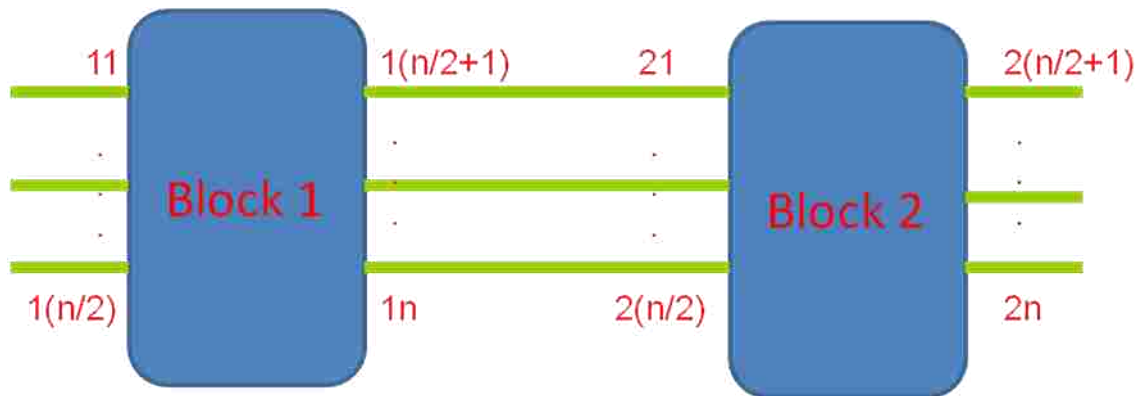


Fig. 4.2 Cascading two n-port S-parameter blocks.

An example to validate the proposed method is from cascading four 4-port networks. The channels in all networks are weakly coupled. Results from traditional method (LPA\_Matlab), proposed method (C++ Engine) and Advanced Design System (ADS) are compared in Fig. 4.3.

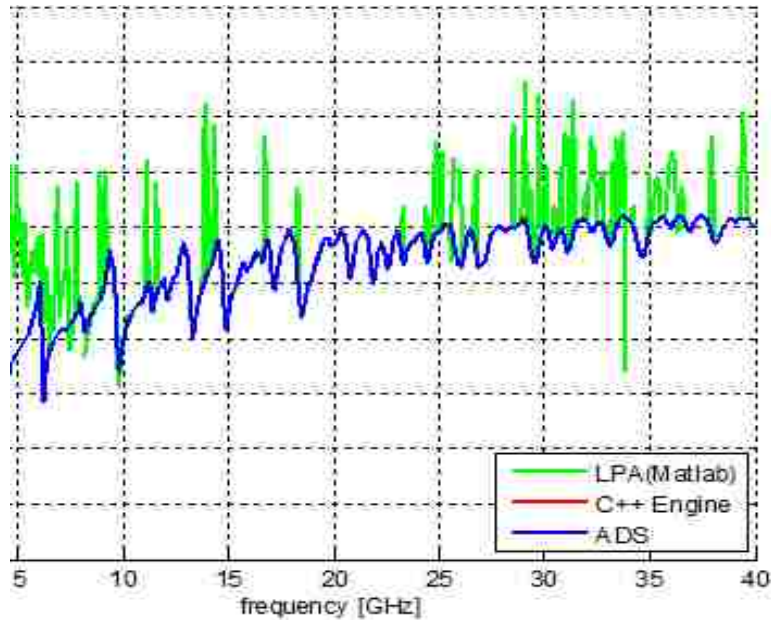


Fig. 4.3 Results comparison of cascaded methods.

#### 4.3. CAUSALITY CHECK AND ENFORCEMENT FOR S-PARAMETER DATA

Physical system should be casual, which means the response should not appear before the excitations. In the simulations of high-speed interconnects, the models for the components, subsystems and system are usually obtained from electromagnetic simulation or direct measurements. Either method cannot achieve perfectly accurate results. Especially, the violations of causality are important defects for the model, as non-causal system functions may lead to failure of time-domain simulations.

In frequency domain, if the real part and the imaginary part of the system function satisfy Hilbert Transform as shown in equation (4.5), the system function would be causal [40].

$$\text{Im}(S(j\omega)) = -\frac{1}{2\pi} \int_{-\pi}^{+\pi} \text{Re} |S(j\theta) \cdot \cot\left(\frac{\omega - \theta}{2}\right)| d\theta \quad (4.5)$$

However, when implementing Hilbert Transform of equation (4.5) directly, the integral is very difficult to calculate as the data usually are only limited up to certain frequency bandwidth while the integration is defined in the entire frequencies. And the data that are over the frequency limitations cannot be simply omitted as they may significantly contribute to the whole integrations. Different techniques are used to solve

this problem. However, technique used in [41] requires the original imaginary part of the system function pass zero point at least once. And data after the last zero point cannot be analyzed.

The Hilbert transform can be equivalent to Kramers-Krnig dispersion relations [42], as

$$\begin{aligned} U(\omega) &= \frac{1}{\pi} \int V(\omega') \frac{d\omega'}{\omega - \omega'} \\ V(\omega) &= -\frac{1}{\pi} \int U(\omega') \frac{d\omega'}{\omega - \omega'} \end{aligned} \quad (4.6)$$

U and V are the real and imaginary part of the system functions.  $\omega$  is the angle frequency and the integrals extends from  $-\infty$  to  $+\infty$ . From [43], the general dispersion relations can be further converted to dispersion relations with subtraction and Lagrange interpolation polynomials, as shown

$$\begin{aligned} U(\omega) &= \beta_U(\omega) + \frac{\prod_{q=1}^n (\omega - \bar{\omega}_q)}{\pi} \int \frac{V(\omega') - \beta_V(\omega')}{\prod_{q=1}^n (\omega' - \bar{\omega}_q)} \frac{d\omega'}{\omega - \omega'} \\ V(\omega) &= \beta_V(\omega) - \frac{\prod_{q=1}^n (\omega - \bar{\omega}_q)}{\pi} \int \frac{U(\omega') - \beta_U(\omega')}{\prod_{q=1}^n (\omega' - \bar{\omega}_q)} \frac{d\omega'}{\omega - \omega'} \end{aligned} \quad (4.7)$$

where

$$\begin{aligned} \beta_F(\omega) &= \sum_{q=1}^n l_q(\omega) F(\bar{\omega}_q) \text{ for } F = \{U, V\} \\ l_q(\omega) &= \prod_{\substack{p=1 \\ p \neq q}}^n \frac{\omega - \bar{\omega}_p}{\omega_q - \bar{\omega}_p} \end{aligned}$$

Equation (4.7) is approximately equivalent to Hilbert Transform, by adopting Lagrange interpolation polynomials. If the real and imaginary parts of the system function satisfy equation (4.7), the data will be causal. The equation (4.7) significantly reduces the sensitivity of high-frequency component, so the unknown high-frequency data can be ignored when calculating the integration. The truncation error will discuss later. However, the dispersion relation and Lagrange interpolation polynomials result in some singularities in the integration. The singularities caused by Lagrange interpolation polynomials can be avoided by wisely picking up the subtraction points  $\bar{\omega}_q$ .  $\bar{\omega}_q$  cannot

be very closed to the frequencies which are chosen as the discrete points in the numerical calculations. The error due to approximation of Lagrange interpolation polynomials can be reduced if the subtraction points  $\bar{\omega}_q$  satisfy

Chebyshev distribution, as

$$\bar{\omega}_q = -B(1-\varepsilon)\cos\frac{(q-1)\pi}{n-1}, q = 1, \dots, n \quad (4.8)$$

$n$  is the order of Lagrange interpolation polynomials.  $B$  is the bandwidth.  $\varepsilon$  is a small number which needs to be closed to one. It can become a changing variable if optimization is required for causality enforcement.

When the original imaginary (or real) part of the data doesn't satisfy equation (9), we simply substitute the original imaginary (or real) part by calculated one from left side of equation (4.7). This procedure is so-called causality enforcement. However, generally the calculated imaginary (or real) part still cannot pass the causality checking, as it is obvious the integrals in the equation (4.7) contain both real and imaginary part. When checking with the calculated imaginary (or real) part, the left side of equation (4.7) should also use the newly generated imaginary (or real) part. Thus, equation (4.7) cannot be satisfied.

To solve the problems mentioned above, special procedure should be taken when calculating the imaginary (or real) part at the subtraction points  $\bar{\omega}_q$ . As discussed before,  $\bar{\omega}_q$  cannot be selected to approach closely to the discrete frequency points in the numerical calculations. The casual imaginary parts at  $\bar{\omega}_q$  are obtained by linear interpolating the casual imaginary parts at their nearby frequency points  $\omega_{q_1}$  and  $\omega_{q_2}$ , as

$$V_{\bar{\omega}_q} = V_{\omega_{q_1}} * ((\omega_q - \omega_{q_2}) / (\omega_{q_1} - \omega_{q_2})) + V_{\omega_{q_2}} * ((\omega_{q_1} - \omega_q) / (\omega_{q_1} - \omega_{q_2})) \quad (4.9)$$

where  $\omega_{q_1}$  and  $\omega_{q_2}$  are the discrete frequency points in the original database.

$V_{q1}$  and  $V_{q2}$  are the casual imaginary parts at  $\omega_{q1}$  and  $\omega_{q2}$ .  $V_{q1}$ ,  $V_{q2}$  can be calculated according to the second equation in (4.7), as

$$V_{q1} = \beta_v(\omega_{q1}) - \frac{\Pi^{n_{q-1}}(\omega_{q1} - \bar{\omega}_q)}{\pi} \int \frac{U(\omega') - \beta_U(\omega')}{\Pi^{n_{q-1}}(\omega' - \bar{\omega}_q)} \frac{d\omega'}{\omega_{q1} - \omega'} \quad (4.10)$$

$$V_{q2} = \beta_v(\omega_{q2}) - \frac{\Pi^{n_{q-1}}(\omega_{q2} - \bar{\omega}_q)}{\pi} \int \frac{U(\omega') - \beta_U(\omega')}{\Pi^{n_{q-1}}(\omega' - \bar{\omega}_q)} \frac{d\omega'}{\omega_{q2} - \omega'} \quad (4.11)$$

Combined equation (4.9), (4.10) and (4.11), we can solve the  $3*n$  dimensional equation set to obtain the casual imaginary parts at  $\omega_{q1}$ ,  $\omega_{q2}$  and  $\bar{\omega}_q$  for different  $q$ .

As an example, the S parameters of a via structure in a typical print circuit board are obtained from a quasi-full-wave solver. A Gaussian pulse is applied at Port 1 starting at  $t = 0$  with a 50-Ohm source resistance. The other three ports are terminated with 50-Ohm loads. The detailed configuration is shown in Fig. 4.4. The time-domain voltage waveform at Port 2 is shown in Fig. 4.5. It can be clearly seen that this response with the original S parameters occurs before  $t = 0$ , which indicates that the original S parameters are non-casual. Thus, causality needs to be enforced to prevent this kind of unphysical response.

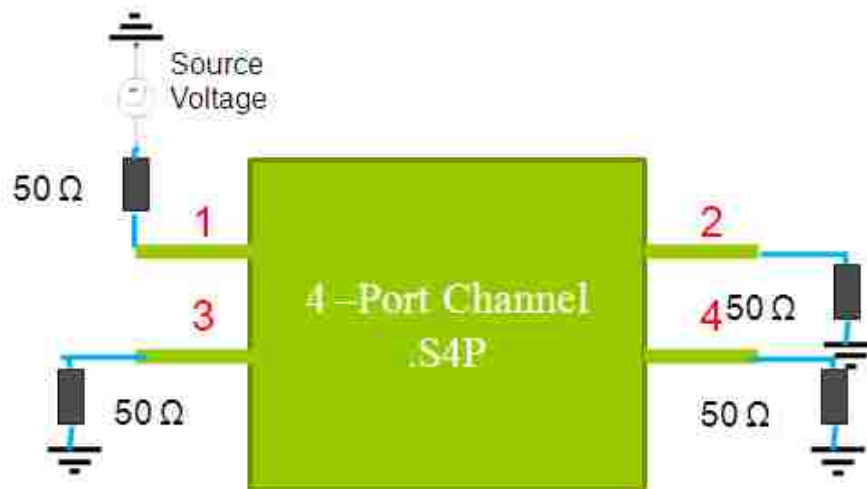


Fig. 4.4 Configuration of a 4-port network representing a via structure in a printed circuit board.

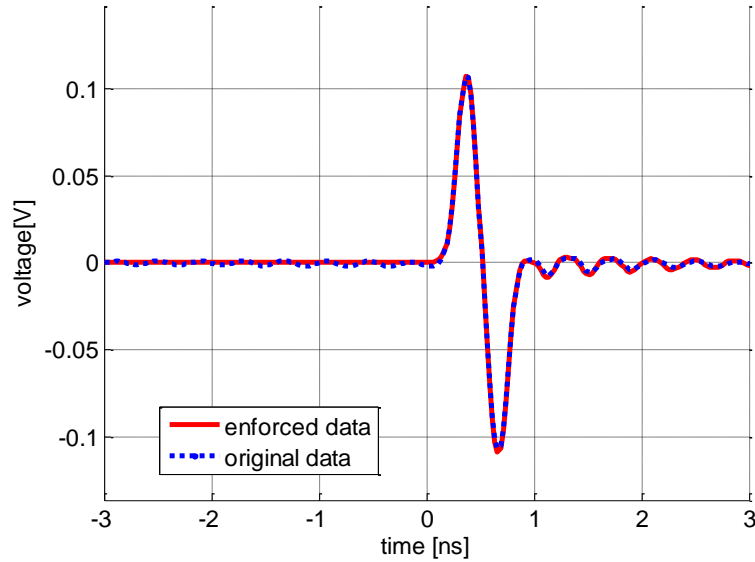


Fig. 4.5 Time-domain responses of the original non-causal data and the enforced causal data.

The S-parameter network after causality enforcement is inserted to the setup shown in Fig. 4.4 response at Port 2 was calculated again and is compared with the original response in Fig. 4.5. It can be seen that the new response is now causal since the voltage at Port 2 is always zero before  $t = 0$ .

#### 4.4. PASSIVITY CHECK AND ENFORCEMENT FOR S-PARAMETER DATA

During recent years, characterization and simulation models of high-speed microwave and electromagnetic device have been studied extensively, due to the continually increasing frequency, circuit density and complexity. S parameters are widely used to characterize high-frequency passive networks. S parameter can be obtained from either simulations or measurement. However, errors due to imperfection of simulation or



measurement methods are inevitable in reality. Passivity is one of the most important parameters to check the reliability of the  $S$  parameter data obtained. Particularly, transient simulations with circuit solvers may suffer major difficulties when the  $S$  parameters of the network are non-passivity in the frequency range of interests.

Since a passive system is necessarily stable and has a power gain less than one, the  $S$  parameter matrix of a passive system is bounded real. If the system function is bounded real, it will satisfy [44]

$$\| S \|_2 \leq 1 \quad (4.12)$$

where  $\| \cdot \|_2$  represents norm-2.

If small passivity violations were found, it is very possible to restore the passivity of the  $S$ -parameter data obtained from measurement or electromagnetic simulations. This section describes an efficient algorithm for restoring the passivity for  $N$ -port network based on the first-order matrix perturbation theory. Only small differences between the original and enforced data sets are acceptable, to ensure the enforced data do not lose fidelity. The data after passivity enforcement can be directly used for transient analysis for convolution techniques as well as passive macromodeling algorithms.

As discussed previously, a passive system requires the norm-2 of its system function less than one. In order to calculate norm-2 of a matrix, calculations of eigenvalue are needed. The norm-2 of a matrix is defined as its largest singular value. The singular value of a compact operator  $S$  acting on a Hilbert space are defined as the eigenvalues of the operator

$$Q = \sqrt{S^* S}, \quad (4.13)$$

where  $S^*$  denotes the adjoint of  $S$  and the square root is taken in the operator sense.

Define

$$T = I - S^* S, \quad (4.14)$$

where  $I$  is identity matrix.

When  $S$  is passive, it also implies that  $I - S^* S \succeq 0$ . In other words, if the norm-2 of  $S$  is smaller than 1, the maximum eigenvalue of  $T$  is positive.

If  $S$ -parameter matrix  $S$  is perturbed by a small amount  $\Delta S$ , then

$$T' = I - (S + \Delta S)^*(S + \Delta S), \quad (4.15)$$

by applying first order matrix perturbation theory, the changes in eigenvalues of  $T$  matrix is given as

$$\Delta\lambda = \frac{v'(-S^* \cdot \Delta S - S \cdot \Delta S^*)u}{v'u} \quad (4.16)$$

where  $v$  and  $u$  are the left and right eigenvectors of  $T$ . Only when  $\Delta\lambda$  is a small value, equation 18 is valid.

When the original S-parameter data is not passive, at least one eigenvalue of  $T$  is smaller than zero. Through perturbations to the original S matrix, we can force all eigenvalues of  $T$  larger than 0.

The extent of violation ( $\Delta\lambda$ ) is firstly set to be the smallest eigenvalue of  $T$  matrix obtained from original S parameters. Based on equation (4.16), we need to solve the perturbed amount for each element in S matrix. This problem becomes an linear optimization with constrains, as

$$\begin{aligned} \alpha_{11}\Delta S_{11real} + \alpha_{12}\Delta S_{12real} + \dots + \alpha_{nn}\Delta S_{nnreal} &= C_1 \\ \beta_{11}\Delta S_{11imag} + \beta_{12}\Delta S_{12imag} + \dots + \beta_{nn}\Delta S_{nnimag} &= C_2 \end{aligned} \quad (4.17)$$

while

$$\min(|\Delta S_{11}|^2 + |\Delta S_{12}|^2 + \dots + |\Delta S_{nn}|^2)$$

where  $\Delta S_{real}$ ,  $\Delta S_{imag}$ ,  $|\Delta S|$  are the real, imaginary and magnitude of the perturbation quantity  $\Delta S$  to the original S parameters.  $C_1$  and  $C_2$  are two constants.  $\alpha$   $\beta$  are the known coefficient sets.

Different optimization methods, such as conjugate gradient method, Frank-Wolfe method, genetic method and so on, can be applied to the optimization problem described by equation (4.17). However, usually the violation from the smallest eigenvalue to zero is much larger than the range within which equation (4.16) can apply. Thus, multiple steps need to be taken to increase the eigenvalues of  $T$  to be greater than 1. In this way, if optimization process in each step takes too much time, the entire calculation for passivity enforced could be unacceptably slow. Meanwhile, although the global optimized solutions for equation (4.17) are desired, they are not necessary. Thus, an optimization method based on weighted factors is applied to this specific problem.

In order to obtain both real and imaginary parts of  $\Delta S$ , following  $2*n^2-2$  equations are needed to add to (4.16)

$$\begin{aligned} \frac{\alpha_{ij}^2}{\sum \alpha_{ij}^2 + \sum \beta_{ij}^2} &= \frac{\Delta S_{ijreal}^2}{\sum \Delta S_{ijreal}^2 + \sum \Delta S_{ijimag}^2} \\ \frac{\beta_{ij}^2}{\sum \alpha_{ij}^2 + \sum \beta_{ij}^2} &= \frac{\Delta S_{ijimag}^2}{\sum \Delta S_{ijreal}^2 + \sum \Delta S_{ijimag}^2} \end{aligned} \quad (4.18)$$

Combined equation sets (4.17) and (4.18), we can solve both real and imaginary parts of perturbation quantity  $\Delta S$ .

Apply weighted factors to solve this optimization problem with constrains can efficiently improve the computational speed, because only a  $2*n^2$  dimensional equation set need to be solved. Although the solutions are not the global optimization points, they are relatively small perturbation to the original data.

Meanwhile, the perturbation quantities are also restricted by a checking step after solved each element in  $\Delta S$ . The S parameters after perturbations are obtained as

$$S_p = S + \Delta S \quad (4.19)$$

Next  $T_p$  matrix is recalculated using equation (4.19) with  $S_p$ . If the difference of the eigenvalue of  $T_p$  and  $T$  cannot be expressed by equation 18, that means the perturbation quantity  $\Delta S$  are out of the constrain within which matrix perturbation theory stands. In this case, the extent of violation ( $\Delta\lambda$ ) need to be smaller than the smallest eigenvalue of  $T$  matrix obtained from original S parameters. Adaptive coefficients can be applied here to find the proper value of violation  $\Delta\lambda$ . Thus, we compensate for the violation  $\Delta\lambda$  in steps and ensure equation (4.16) is valid in each step.

An example for passivity enforcement is illustrated below. The S parameters of differential-signal via structure were obtained from the equivalent transmission model noted above. The S-parameter data is from 10 MHz to 5 GHz. Passivity check was preceded before simulations. As shown in Fig. 4.6, the original data from the model was not passive at several frequency points, as their values of norm 2 were greater then 1. The algorithm of passivity enforcement discussed in this section was then applied to the S parameter data. Fig. 4.6 shows the norm 2 of the S parameters before and after passivity

enforcement. After passivity enforcement, the values of norm 2 at all the frequencies are not larger than 1, which means the S parameters became passive.

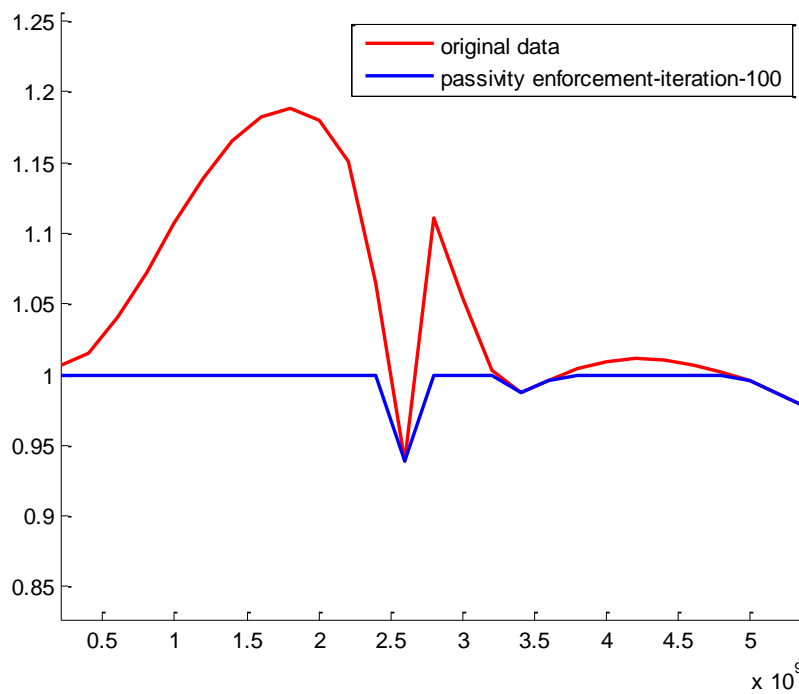


Fig. 4.6 Norm 2 of the S-parameter matrices before and after passivity enforcement.

## 5. APPLICATIONS OF FEATURE SELECTIVE VALIDATION TECHNIQUE

Feature Selective Validation (FSV) technique is expanded in this thesis to quantify the comparisons of data sets and provide quantitative standard for data optimization. In the S

Section 5.1, a new approach is proposed to validate different uncertain approaches without knowing a standard reference by applying the Feature Selective Validation (FSV) technique. New reference is established by the weighted average of the various approaches. Four via modeling methods including physics-based circuit model, equivalent transmission line model, multiple scattering model, and full wave model are compared and validated by the approach proposed in this section to illustrate the effectiveness of different via modeling techniques. In Section 5.2, the application of the FSV technique is extended to data optimization. The raw data obtained from simulations or measurements are often non-ideal for further processing. Several techniques, such as data perturbation, can be used to improve the data quality in certain aspects. However, after modifications the new data could be very different to the original one. Using FSV as an objective function for the optimization process is discussed in this paper, in an example of causality enforcement, to ensure the enforced casual data has the minimum deviations from the original data. The results demonstrate that the proposed approach is effective for data modification and optimization.

### 5.1. APPLY FSV TO COMPARE DATA SETS WITHOUT STANDARD

**5.1.1 Introduction.** Different computational electromagnetic modeling techniques are often used to simulate a specific model simultaneously. The preferred process for validation of one unknown modeling technique is to compare the unknown case with a known reference. A standard reference is always obtained from analytical solutions or experimental results. However, it is often the case that a suitable reference is difficult to obtain while validating several modeling techniques among themselves. In this situation, validation of each modeling technique needs to be quantified.

Recently, the Feature Selective Validation (FSV) procedure [45] is specified to judge the level of agreement between validation reference and unknown modeling result. The FSV technique shall be used to quantify the comparison data sets in order to minimize ambiguities of validation standards, which may be misled by subjectivity of individuals. The basis of the FSV approach is to decompose the original data sets into low-pass and high-pass components to filter out the amplitudes and features information. And then the two kinds of information are recombined to provide a global judgment for the entire pair of data set.

On the other hand, via models in print circuit board (PCB) have been extensively studied in the past years. Full-wave numerical computation is effective to model vias with small cavities. All the boundary conditions of the via structure are satisfied in full-wave methods, but rigorous 3-D electromagnetic modeling of full-wave methods requires the complete power and ground planes to be included in the computational domain, which may consume lots of computational resources.

Recently, there are three kinds of approaches in modeling the vias in a plane pair. One algorithm called the Foldy-Lax multiple scattering method is proposed for analysis of via arrays in a plane pair [46]-[48]. The method adopts magnetic frill current as the source. The via barrel is modeled as perfect electric conductor (PEC) boundary and the Green's function between two PEC planes is used to calculate the fields in the plane pair. By adopting addition theorem of the cylindrical waves, the multiple scattering effects among vias are considered.

On the other hand, a physics-based circuit model is proposed to characterize the via behaviors in circuit boards and packages [49]-[51]. As the via length is usually electrically small, the via can be modeled as a lumped circuit with two via-plane capacitances at the ends of the via barrel. The impedance of the parallel plane is used to represent the propagating parallel plane modes.

Different from the physics-based circuit model, an equivalent transmission line model for the via structure is developed by considering the distributed fields behavior along the via barrel.

However, all the via modeling techniques have its own approximations to simplify the complex electromagnetic environment in the cavity with vias. Thus, it is

difficult to determine the accuracy of each via model by analyzing the theoretical processes.

In this Section, Section 5.1.1 first discusses a general method to select a suitable reference from several unknown modeling techniques based on the FSV results. Then validation of each modeling technique is quantified by comparing with the established reference.

In Section 5.1.2, a specific via structure is simulated by several different modeling techniques. The simulation data is validated based on the algorithm developed in Section 5.1.1.

### 5.1.2. Comparison Among Data Sets Without a Known Standard Reference.

The FSV method can provide an effective approach to quantify the similarity of two data sets by decomposing the Global Difference Measure (GDM) to Amplitude Difference Measure (ADM) and Feature Difference Measure (FDM). All the ADM, FDM and GDM are usable as point-by-point analysis tools [52, 53].

The range of FSV values of ADM, FDM and GDM can be divided into six categories, each with a natural language descriptor: Excellent, Very Good, Good, Fair, Poor, and Very Poor.

For comparison among complex values, FSV decomposes the complex number to the real and imaginary part (or magnitude and phase) and compare them separately, then recombines them at the end. This way is similar as what engineers deal with complex values in reality. A weighted factor  $K$  is added for combination of compared results of the real and imaginary, or magnitude and phase parts, in the process of forming an overall opinion, as

$$xMD_{combined}(f) = \sqrt{K \cdot xMD_{real}(f) + (1 - K) \cdot xMD_{imag}(f)} \quad (5.1)$$

or

$$xMD_{combined}(f) = \sqrt{K \cdot xMD_{mag}(f) + (1 - K) \cdot xMD_{phase}(f)} \quad (5.2)$$

When  $n$  unknown methods need to be validated without an existing references, the standard reference needs to be determined as the first step. From  $n$  different uncertain modeling techniques,  $n$  separate data sets can be obtained.

Assume these  $n$  data sets share a common independent variable (plotted as an x-axis) and a common dependant variable (plotted as a y-axis) and have same data points. The dependant variable vector of  $n$  data sets can be denoted as:  $\mathbf{a}_1, \mathbf{a}_2, \dots, \mathbf{a}_n$ . The average variable vector of these  $n$  data sets can be written as:

$$\mathbf{a}_{ave} = \frac{1}{n} \sum_{i=1}^{i=n} \mathbf{a}_i \quad (5.3)$$

Applying the FSV techniques between each data set and the average variable vector  $\mathbf{a}_{ave}$ , a vector FSV values can be obtained as:

$$x\mathbf{MD}_{ave} = \{xMD_1, xMD_2, \dots, xMD_n\} \quad (5.4)$$

with  $x = A, F, G$ .

It is obvious that the larger  $xMD_i$  value indicates greater discrepancies between the  $i$ th modeling method and the other methods. Thus, the liability of  $i$ th modeling methods should be lower. To avoid the problem that the liability of each method is inverse proportional to its  $xMD_{ave}$  value, a new vector FSV value is defined as:

$$x\mathbf{MD}' = xMD_{max} \cdot \mathbf{ones} - \{xMD_1, xMD_2, \dots, xMD_n\} \quad (5.5)$$

where  $\mathbf{ones}$  is an  $n$ -by-1 matrix of 1s, and

$$xMD_{max} = \max\{1.6, \max(xMD_i)\} \quad (5.6)$$

1.6 is the FSV value from which the correlation of two data sets is considered as Very Poor. When  $xMD_{max}$  is smaller than 1.6, all the modeling techniques can be considered as meaningful methods. Thus, the results from all the methods generate weighted effects to the reference. However, when  $xMD_{max}$  is greater than 1.6, at least one modeling result is far away from the other results. In this situation, the effects of the method which deviates the most from others will be ignored.

To establish the standard reference for the validation procedure, the effects from each modeling technique should be considered unevenly according to the different liabilities of the methods. The weight coefficient of each modelling approaches for the reference can be written in term of  $x\mathbf{MD}'$  as:



$$w_i = xMD'_i / (\sum_{i=1}^n xMD'_i) \quad (5.7)$$

Thus, the reference for the validation for  $n$  separate data sets can be determined as:

$$\mathbf{a}_{ref} = \sum_{i=1}^{i=n} w_i \mathbf{a}_i \quad (5.8)$$

As long as the standard reference is obtained, the validation of each modeling technique can be easily achieved by calculating the vector FSV values between each method and the established reference.

**5.1.3 Applying FSV Techniques to Validate Different Via Modeling Approaches.** A typical differential via in multilayer structure is shown in Fig.5.1.

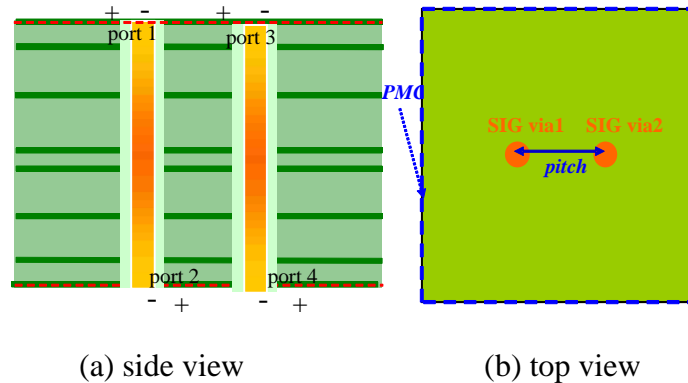


Fig. 5.1 Differential via in multilayer structure with four ground via

The board showing in Fig. 5.1 consists 8 full plane layers. The size of the board is 1"x1.5". Two differential signal vias are located right at the center of the board. The pitch size between the two vias is 50mils. The dielectric thickness between plane layers are 3.54mils, 16.27mils, 15.77mils, 3.32mils, 15.77mils, 16.27mils and 3.54mils from top to bottom respectively. Permittivity of the dielectric layers is 4.0 and loss tangent is 0.01.

The results of differential insertion loss ( $S_{DD21}$ ) are shown in Fig. 5.2 for both magnitude and phase. The results are obtained from the four different modeling methods including “physics-base”, “equivalent transmission line”, “Multiple scattering” and full wave method (HFSS). The average value of these results is also shown in the figure.

The result of each method is compared with the average result to get the combined FSV GDM value. The coefficient K used to combine the magnitude and phase results is assigned to be 0.5. These compared FSV values are presented in Table 5.1.

TABLE 5.1 FSV results using average value as reference

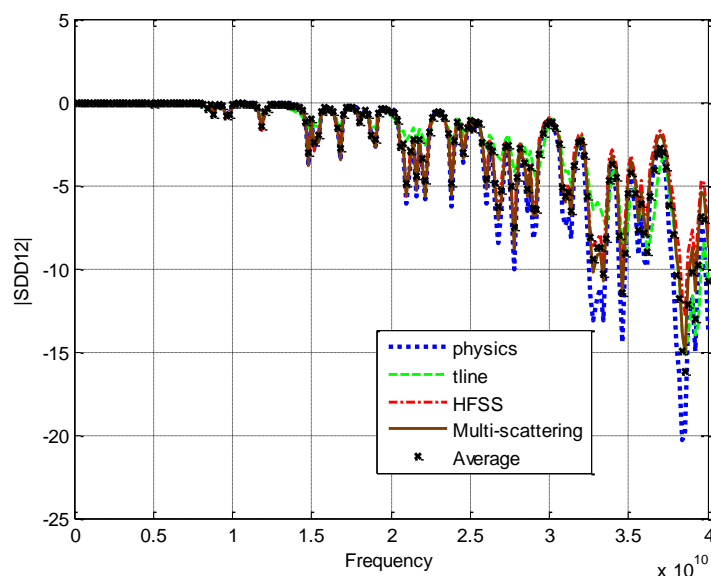
Physics-Based Circuit Model	Equivalent Transmission Line Model	Full Wave Model	Multiple Scattering Model
0.33758	0.43854	0.23082	0.14624

Based on these FSV values, the weight coefficient of each method can be calculated. The standard reference based on these weight coefficients can be obtained. The new FSV values of each method which uses this new weighted average value as reference can be easily obtained as in Table 5.2.

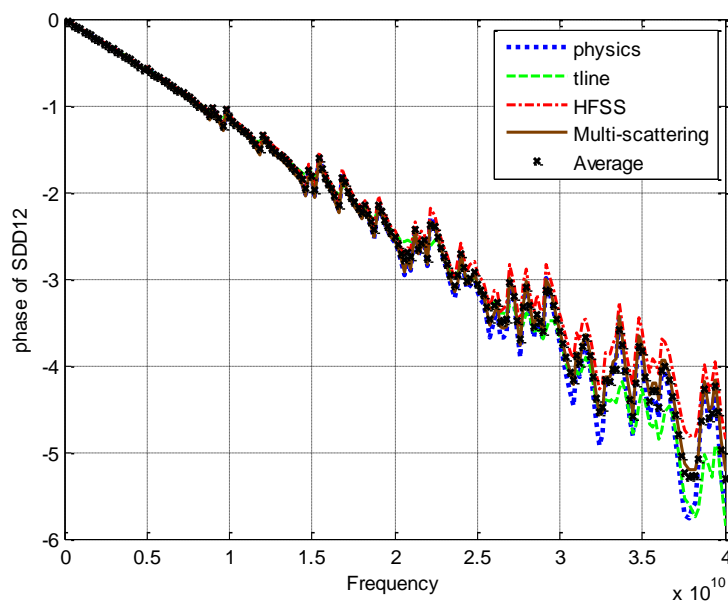
The comparison between the results of the four modeling methods and the new weighted average value is shown in Fig. 5.3.

The results of four model methods are already very close to each other. Therefore, the FSV results only change a little after the reference values are changed from the average to the weighted average. However, the difference shown between the two sets of FSV values still can indicate the influence of the weighting coefficients. The FSV results of multiple scattering model and full wave model become smaller when the weighted average reference is used while the FSV value of equivalent transmission line model increases. The FSV value of the physics-based circuit model becomes slightly smaller after using the weighted average method. This indicates that the equivalent transmission line model is a little far away from the other three results. The absolute FSV values of the

four modeling methods also show that the multiple scattering model is “very good”, the full wave model and the physics-based circuit model are “good”, and the equivalent transmission line model is “fair” based on the weighted average reference value.



(a)



(b)

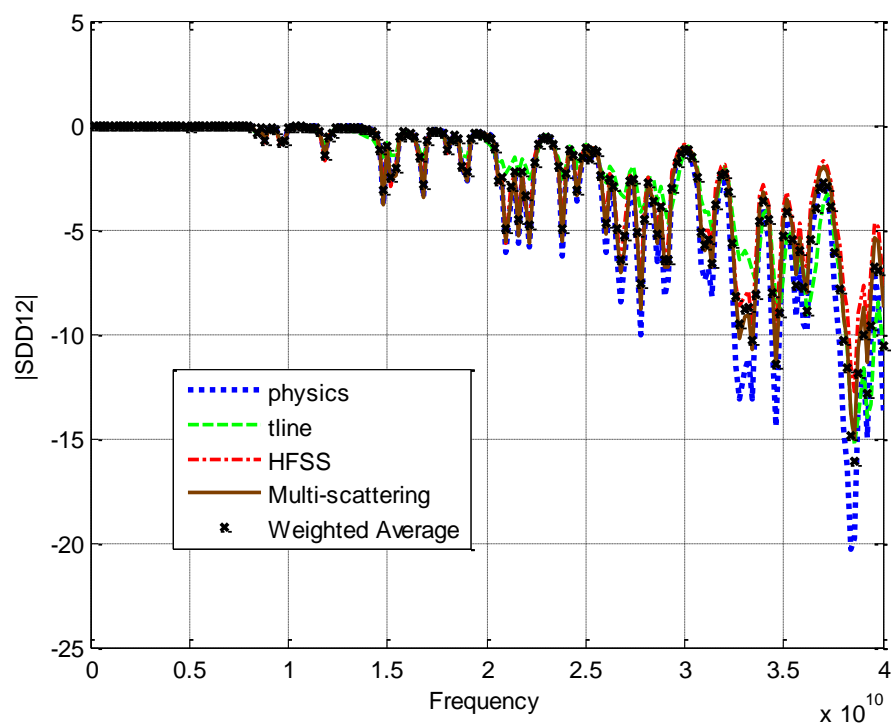
Fig. 5.2  $S_{DD21}$  (a) Magnitude (b) Phase

TABLE 5.2 FSV results using new weighted average value as reference

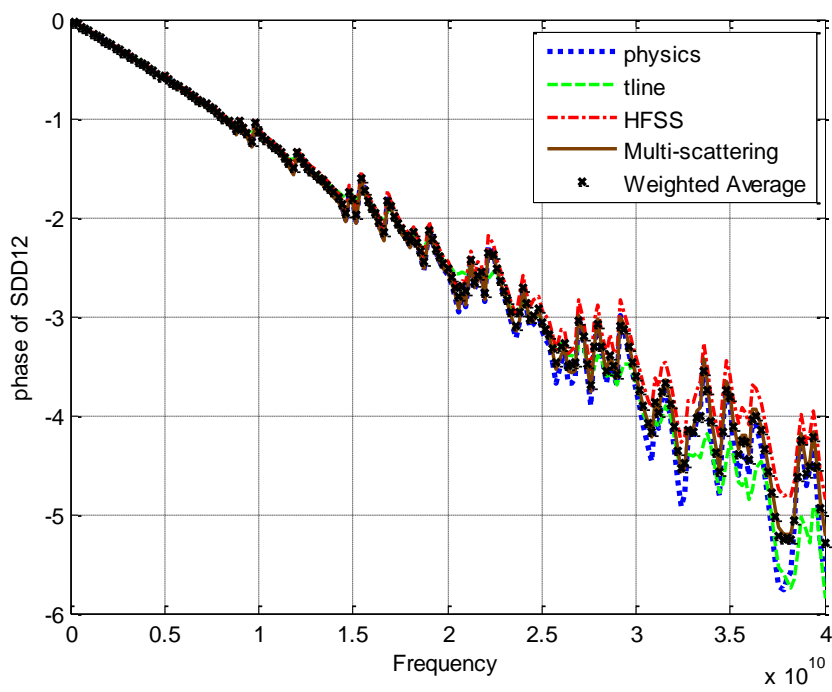
	Physics- Based Circuit Model	Equivalent Transmission Line Model	Full Wave Model	Multiple Scattering Model
Weight coefficient	0.2406	0.2214	0.2610	0.2771
FSV value	0.33361	0.45247	0.21844	0.13068

The comparison between the results of the four modeling methods and the new weighted average value is shown in Fig. 5.3.

The results of four model methods are already very close to each other. Therefore, the FSV results only change a little after the reference values are changed from the average to the weighted average. However, the difference shown between the two sets of FSV values still can indicate the influence of the weighting coefficients. The FSV results of multiple scattering model and full wave model become smaller when the weighted average reference is used while the FSV value of equivalent transmission line model increases. The FSV value of the physics-based circuit model becomes slightly smaller after using the weighted average method. This indicates that the equivalent transmission line model is a little far away from the other three results. The absolute FSV values of the four modeling methods also show that the multiple scattering model is “very good”, the full wave model and the physics-based circuit model are “good”, and the equivalent transmission line model is “fair” based on the weighted average reference value.



(a)



(b)

Fig. 5.3  $S_{DD21}$  (a) Magnitude (b) Phase

**5.1.4 Summary.** The weighted average method is introduced in this paper to compare results of different via modeling methods based on the FSV technique. The weighted coefficients are obtained from the FSV value of each method compared with the average value of all the modeling methods. Based on the weighted coefficients, a new standard reference value is obtained which can be used to run FSV simulations again. The result of the modeling methods which are far away from the other results can be selected out based on this weighted average method.

The new approach is applied to validate the results of four different methods in via modeling including physics-based circuit model, equivalent transmission line model, multiple scattering model and full wave model. The example shows that the result of the equivalent transmission line model is a little far away from the other three results. The multiple scattering model shows a “very good” FSV result, while the full wave model and the physics-based model show “good” FSV results and the equivalent transmission line model shows a “fair” FSV result.

## **5.2. APPLY FSV TO DATA OPTIMIZATION**

**5.2.1. Introduction.** In high-speed link path or channel modeling, channel components and the entire passive link are usually characterized using electromagnetic simulations or direct measurements. In most practical cases, models from measurements or simulations inevitably show discrepancies and often have non-ideal properties. The raw responses may be affected by noise in case of measurements, or by numerical errors when obtained from simulations.

Thus, models obtained from measurements or simulations may need to be corrected using certain methods to minimize the errors in practical signal integrity investigations. For example, causality and passivity are the two important properties of a model. It is highly desirable that a model is casual and passive in the frequency range of interest, to avoid unstable and unphysical response in the time-domain simulations of the model. When a model is not causal or passive, data perturbation methods can be used to enforce passivity and causality by modifying the original data/response of the model. The data after perturbation need to satisfy causality and passivity while they should also be

close to the original data. In this situation, the differences between the data sets need to be evaluated to ensure the enforced data has the minimum deviation from the original one.

The traditional way to measure the differences between two data sets is the least square method, which can give a single value as an objective function in the process of data optimization. However, errors caused by simulations or measurements not only appear in the form of magnitude variations, but also show up as timing jitter or frequency shift. The least square method is unable to distinguish the magnitude and the frequency/time variations.

Recently, the Feature Select Validation (FSV) method has been introduced as a validation method to quantitatively compare different data sets. FSV has its unique advantage of categorizing the differences between data sets as magnitude variations and feature variations [45], [46]. The FSV technique was originally proposed to quantify the comparisons between different data sets in order to minimize the ambiguities caused by subjectivity of individuals. The basis of the FSV approach is to decompose the original data sets into low-pass and high-pass components to filter out the amplitude and feature information.

In this paper, the specific procedure of applying the FSV method as an objective function in the example of causality enforcement will be discussed, to obtain the enforced data with the minimum discrepancy from the original data set.

**5.2.2. Applying FSV as an Objective Function in Causality Enforcement.** As noted in Section 4.3, a physical system should be casual, which means its response should not appear before the excitation. Section 4.3 introduced the specific procedures to check and enforce causality for the S-parameters of a network.

However, only minimum perturbations are allowed between the enforced and the original imaginary parts, as data could lose fidelity after enforcement if the discrepancies are too large. In other words, correction becomes meaningless if the original data are significantly distorted. Therefore, causality enforcement shall include a data optimization procedure with an objective function taking into consideration of the differences between the enforced and the original data.

The FSV method can provide an effective approach to quantify the similarity of two data sets by decomposing the Global Difference Measure (GDM) to Amplitude Difference Measure (ADM) and Feature Difference Measure (FDM). In this way, unlike the least square method, differences between each data set in both magnitudes and features can be taken into account in the algorithm of FSV. Therefore, GDM could be a suitable value to illustrate the differences between the enforced and the original data to optimize  $\varepsilon$  in equation (4.8).

**5.2.3. Genetic Algorithm and Data Optimize for Causality Enforcement.** The S parameters can describe the electrical behaviors of linear electrical networks with steady state stimuli. For a casual system, the real and imaginary parts of the S parameters should satisfy (4.5).

Genetic algorithm (GA) is applied to optimize the GDM value between the original and the enforced data to achieve the minimized perturbations. GA is a stochastic search method based on the concepts of natural selection and evolution [48]. In this case, the objective function  $F(x)$  is not analytically related to the variable  $x$ . Therefore, it is not possible to get the minimum of  $F(x)$  using some hill-climbing optimization methods, and GA is thus adopted. The GA procedures are illustrated in Fig. 5.4.

In the procedures, an 8-bit binary coding is used for the parameter  $x$ . Totally 8 individuals are included and the population remains constant in each generation. Tournament selection is adopted as the selection method, and point crossover with a probability of 0.7 is used. In addition, one bit mutation with a probability of 0.05 is used, and the elitist strategy is applied at the end of each reproduction cycle to ensure that the minimum value of the objective function is preserved to next generation [54].



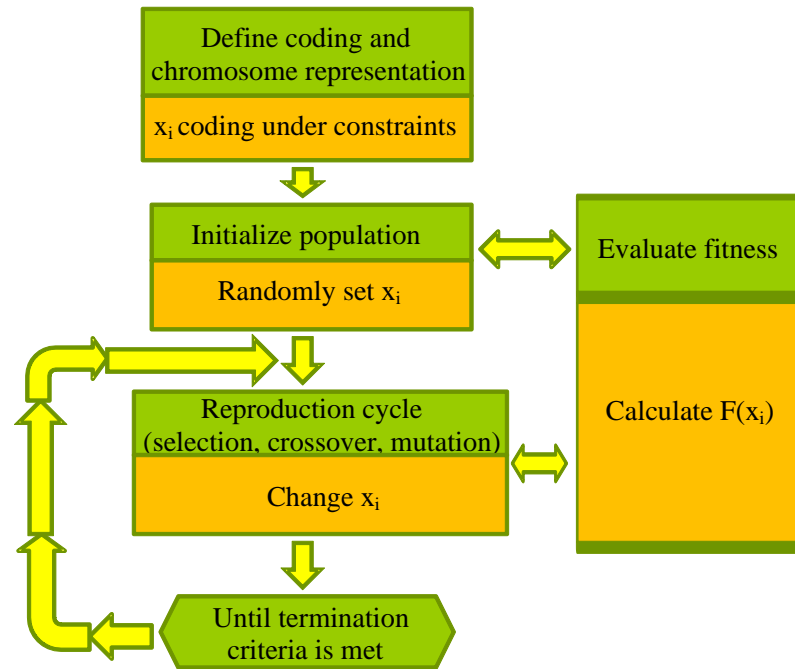


Fig. 5.4 The GA optimization procedures for causality enforcement.

Define the deviation among individuals in each generation as

$$\frac{\max(F(x_i)) - \min(F(x_i))}{|\sum_i^n (F(x_i))/n|} \quad (5.9)$$

where  $F(x_i)$  is the objective function for each individual  $x_i$  in each generation;  $n$  is the number of the individuals in each generation. This deviation in (5.9) indicates the convergence of the GA. If the deviation becomes close to 0, it means that all the individuals  $x_i$  converge to the optimized value that leads to the end of the optimization.

S-parameters of via structures in Fig. 4.4 is used again as an example to validate the algorithm. The deviation value defined in (5.9) as a function of the number of generations is shown in Fig. 5.5. From (5.9), it is obvious that the value of the GDM for

individuals is convergent to 0. At the 6<sup>th</sup> generation, the deviation is already small enough as shown in Fig. 5.5. So the optimization process stops and the minimum GDM value in the 6<sup>th</sup> generation becomes the optimized FSV value between the enforced and the original data.

The original imaginary part of the S parameters and the imaginary part after causality enforcement with FSV optimization are both plotted in Fig. 5.6. The FSV values of the two curves in Fig. 5.6 are shown in Fig. 5.7. The total GDM has achieved its optimized value of 0.0741 and the data comparisons for 80% of the frequency points appear in the category of “Excellent”, which indicates the data after causality enforce only have very small distortions compared to the original data set.

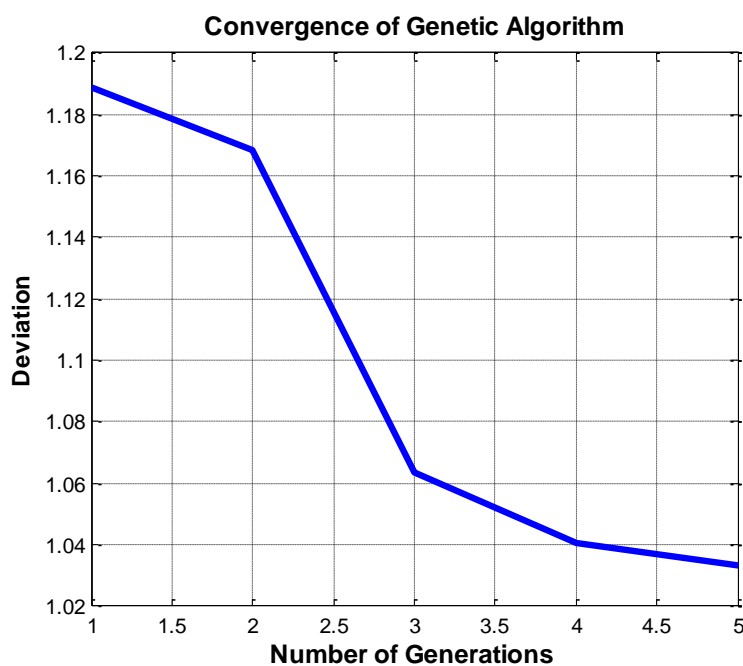


Fig. 5.5 Deviation among individuals in each generation.

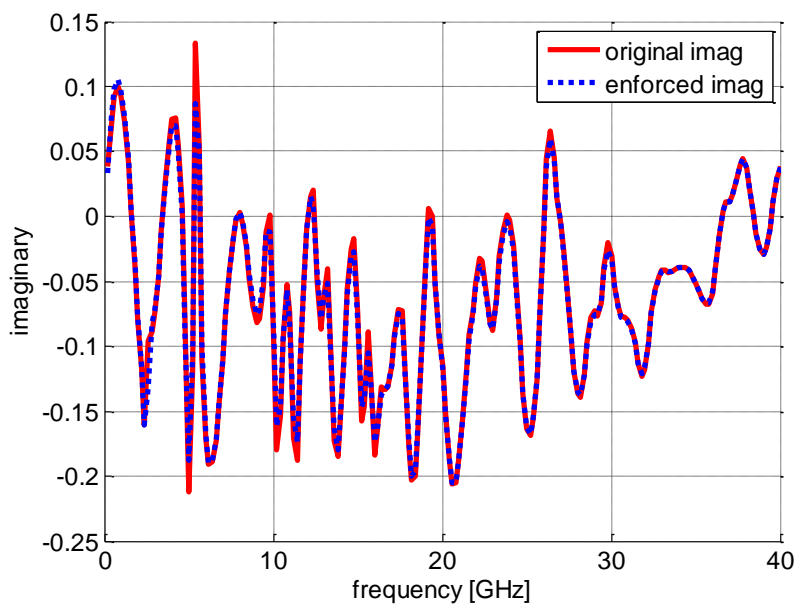


Fig. 5.6 Comparison between the original and the enforced imaginary parts of the S parameters.

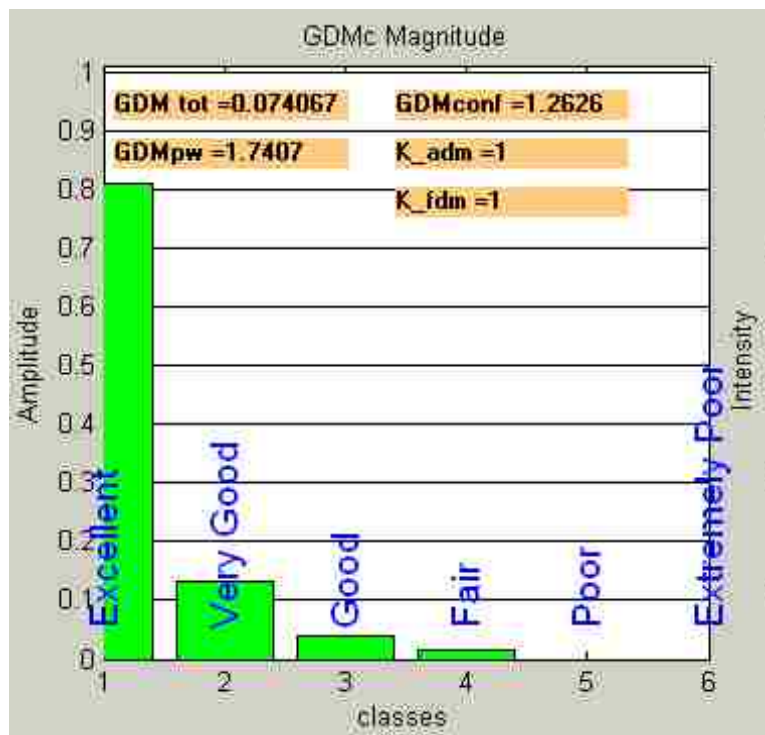


Fig. 5.7 FSV results of the original and the enforced data shown in Fig. 5.6.

**5.2.4. Summary.** In this paper, the application of the FSV technique is extended to optimize data sets through perturbations. Instead of using the least square method, the GDM value from the FSV approach can be used as an objective function to minimize the differences of data sets in terms of both magnitude and feature variations. In order to obtain a set of data with the minimum derivations from the original data set after perturbations, the GDM value between the two data sets is minimized.

The optimization procedure using the FSV method has been successfully applied to causality enforcement for S parameters. The real and imaginary parts of the S parameters after enforcement should satisfy the Hilbert transform. Besides, the enforced S parameters should not deviate too much from the original data. The optimization based on the GDM value ensures that the minimum deviations have been achieved in the process of causality enforcement.

**BIBLIOGRAPHY**

- [1] P. Kok, and D. D. Zutter, "Capacitance of a circular symmetric model of a via hole including finite ground plane thickness," *IEEE Trans. Microwave Theory Tech.*, vol. 39, no. 7, pp. 1229-1234, July 1991.
- [2] K.S. Oh, J.E. Schutt-Aine, R. Mittra, and W. Bu, "Computation of the equivalent capacitance of a via in a multilayered board using the closed form Green's function," *IEEE Trans. Microwave Theory Tech.*, vol. 44, no. 2, pp. 347-349, Feb. 1996.
- [3] T. Wang, R. F. Harington, and J. R. Mautz, "Quasi-Static analysis of a microstrip via through a hole in a ground plane," *IEEE trans. Microwave Theory Tech.*, vol. 36, no. 6, pp.1008-1013, Jun 1988.
- [4] A.C. Cangellaris, J.L. Prince, L.P. Vakanas, "Frequency-dependent inductance and resistance calculation for three-dimensional structures in high-speed interconnect systems" *IEEE trans. on Components, Hybrids, and Manufacturing Technology*, vol.13, no. 1, pp. 154-159, March 1990.
- [5] S. Maeda, T. Kashiwa and I. Fukai "Full wave analysis of propagation characteristics of a through hole using the finite-difference time-domain method," *IEEE Trans. Microw. Theory Tech.*, vol. 39, pp. 2154, Dec. 1991.
- [6] S.-G. Hsu and R.-B. Wu "Full-wave characterization of a through hole via in multilayered packaging," *IEEE Trans. Microw. Theory Tech.*, vol. 43, pp. 1073, May 1995.
- [7] H. Chen, Q. Lin, L. Tsang, C.-C. Huang, and V. Jandhyala, "Analysis of a large number of vias and differential signaling in multilayered structures," *IEEE Trans. Microwave Theory Tech.*, vol. 51, no. 3, pp. 818-829, Mar. 2003.
- [8] L. Tsang, and D. Miller, "Coupling of vias in electronic packaging and printed circuit board structures with finite ground plane," *IEEE Trans. Adv. Packag.*, vol. 26, no. 4, pp. 375-384, Nov. 2003
- [9] X. Gu and M. B. Ritter, "Application of Foldy-Lax Multiple Scattering Method To Via Analysis in Multi-layered Printed Circuit Board," *DesignCon 2008*, Santa Clara, CA USA, Feb. 4 - Feb. 7, 2008.
- [10] C. Schuster, Y. Kwark, G.Selli, and P. Muthana, "Developing a 'Physical' Model for Vias," *DesignCon 2006*, Santa Clara, CA USA, Feb.6-9, 2006.

- [11] G. Selli, C. Schuster, and Y. Kwark, M. B. Ritter, and J.L DREWNIAK, "Developing a Physical Via Model for Vias – Part II: Coupled and Ground Return Vias," DesignCon 2007, Santa Clara, CA USA, Jan.29-Feb 1, 2007.
- [12] G. Selli, C. Schuster, Y. Kwark, J. DREWNIAK, "Model-to-Hardware Correlation of Physics Based Via Models With the Parallel Plate Impedance Included," IEEE Symposium on Electromagnetic Compatibility, Portland, OR, USA, August 2006.
- [13] Renato Rimolo-Donadio, Xiaoxiong Gu, Young H. Kwark, Mark B. Ritter, Bruce Archambeault, Francesco de Paulis, Yaojiang Zhang, Jun Fan, Heinz-Dietrich Brüns, and Christian Schuster, "Physics-Based Via and Trace Models for Efficient Link Simulation on Multilayer Structures Up to 40 GHz," IEEE TRANSACTIONS ON MICROWAVE THEORY AND TECHNIQUES, VOL. 57, NO. 8, AUGUST 2009
- [14] G.T. Lei, R. W. Techentin, P. R. Hayes, D. J. Schwab, B. K. Gilbert, "Wave Model Solution to the Ground/Power Plane Noise Problem," IEEE Transactions on Instrumentation and Measurement, Vol. 44, No. 2, April 1995.
- [15] R. Chadha, K.C. Gupta, "Segmentation Method Using Impedance Matrices for Analysis of Planar Microwave Circuits," IEEE Transactions on Microwave Techniques, Vol. MTT-29, No.1, January 1981.
- [16] M. Xu, Y. Ji, T. H. Hubing, T. P. Van Doren, and J. L. DREWNIAK, "Development of a closed-form expression for the input impedance of power-ground plane structure," in Proc. IEEE Int. Symp. Electromagn. Compat. Washington, DC, Aug. 2000, pp. 77-82.
- [17] S. Ramo and J. R.J. R. Whinnery, Fields and Waves in Modern Radio, 2nd ed. New York: Wiley, 1953, ch. 8.
- [18] Y. Zhang, J. Fan, G. Selli, M. Cocchini, D. P. Francesco, "Analytical Evaluation of Via-Plate Capacitance for Multilayer Printed Circuit Boards and Packages," IEEE Trans. Microwave Theory Tech., vol. 56, no. 9, pp. 2118-2128, Sep. 2008.
- [19] X. Gu, A. Ruehli, M. Ritter, "Impedance Design for Multi-layered Vias," Electrical Performance of Electronic Packaging, 2008 IEEE-EPEP, pp. 317-320.
- [20] C. R. Paul, "Analysis of Multiconductor Transmission Lines," New York: Wiley-Intersciences, 1994, pp. 195-224.
- [21] C. R. Paul, "Introduction to Electromagnetic Compatibility," New York: Wiley-Intersciences, 2006, pp. 595-612.
- [22] S. Wu, J. Fan, "Investigation of Crosstalk Among Vias," submitted to the IEEE International Symposium on Electromagnetic Compatibility, Austin, TX, 2009

- [23] M. Cocchini, W. Cheng, J. Zhang, J. Fisher, J. Fan, J. Drewniak and Y. Zhang, "Differential vias transition modeling in a multilayer printed circuit board," IEEE International Symposium 2006, Detroit, MI. August 2008
- [24] H. Wang, W. Cheng, J. Zhang, J. Fisher, L. Zhu, J. L. Drewniak, and J. Fan, "Investigation of mixed-mode input impedance of multi-layer differential vias for impedance matching with traces," in Proc. IEEE International Symposium on Electromagnetic Compatibility, Austin, USA, Aug. 2009, pp.203-207
- [25] IEC 61967-2:2005, "Integrated circuits – Measurement of electromagnetic emissions, 150 kHz to 1 GHz – Part 2: Measurement of radiated emissions, TEM cell and wideband TEM-cell method," First edition, Sep. 2005.
- [26] V. Kasturi, S. Deng, T. Hubing and D. Beetner, "Quantifying electric and magnetic field coupling from integrated circuits with TEM cell measurements," Proc. 2006 IEEE Symposium on Electromagnet. Compatibility, Portland, Oregon, 14-18 Aug. 2006.
- [27] Goulette, R.R., "The Measurement of Radiated Emissions from Integrated Circuits," IEEE Symposium on Electromagnet. Compatibility, 17-21 Aug. 1992.
- [28] Weiping He, Dr. Richard E DuBroff, "Modeling Radiated Emissions of Electronic Circuits with a set of Electric Dipoles," MST EMC Laboratory Technical Brief, Third Quarter 2008.
- [29] R. M. Gulrajani, "The forward and inverse problems of electrocardiography," IEEE Engineering in Medicine and Biology Magazine, vol. 17, pp. 84-101, Sept 1998.
- [30] P. Wilson, "On correlating TEM cell and OATS emission measurements," IEEE Transactions on Electromagnetic Compatibility, Volume 37, Issue 1, Page(s):1 – 16, Feb. 1995.
- [31] A. Tsaliovich, "Modelling electronic system radiated field patterns," in Proc. 8th Int. Zurich Symp. and Techn. Exhb. on Electromugn. Comput., Zurich, Switzerland, Mar. 1989, pp. 323-328.
- [32] R. E. Collin, Field Theory of Guided Waves. New York, NY: McGraw-Hill, 1960.
- [33] R. Johnson and H. Jasik, Eds., Anrennu Engineering Handbook, 2nd ed. New York McGraw-Hill, 1984, ch. 2.
- [34] H. Weng, D. G. Beetner, R. E. DuBroff, J. Shi, "Estimation of current from near-field measurement," IEEE Trans. Electromagn. Compat., pp 222-227, Aug 2005.

- [35] Y. Vives, C. Arcambal, A. Louis, F. de Daran, P. Eudeline, and B. Mazari, "Modeling Magnetic Radiations of Electronic Circuits using Near-Field Scanning Method," *IEEE Trans. Electromagn. Compat.*, vol. 49, no. 2, pp. 391-400, May 2007.
- [36] R. D. Throne and L. G. Olson, "A Generalized Eigensystem Approach to the Inverse Problem of Electrocardiography," *IEEE Trans. Biomedical engineering*, vol. 41, no.6, pp. 592-600, June 1994.
- [37] D. G. Beetner and R. M. Arthur, "Direct Inference of the Spectra of Pericardial Potentials Using the Boundary-Element Method," *Annals of Biomedical Engineering*, vol. 27, pp. 498-507, 1999.
- [38] C. A. Balanis, *Antenna Theory: Analysis and Design*, 3rd ed., Hoboken, New Jersey, USA: John Wiley & Sons, Inc., 2005.
- [39] "Integrated Circuits, Measurements of Electromagnetic Emission 150 kHz–1GHz," International Electrotechnical Commission, Geneva, Switzerland, IEC 61967, 2000.
- [40] J. R. James, G. Andrasic, "Assessing the accuracy of wideband electrical data using Hilbert transforms," *IEE Proc.*, vol. 137, pp. 184-188, 1990.
- [41] F. Paulis, "Block level link path design and multilayer via transition model assembly using S-parameters," M.S. Thesis, Missouri University of Science and Technology, 2008.
- [42] S. L. Hahn, "Hilbert transforms," in *The Transforms and Applications Handbook*, A. D. Poularikas, Ed. CRC and IEEE, 2000.
- [43] P. Triverio and S. Grivet-Talocia, "A robust causality verification tool for tabulated frequency data," in *10th IEEE Workshop on Signal Propagation on Interconnects*, Berlin, Germany, May 9–12, 2006
- [44] Miguel Silveira Carlos , Carlos P. Coelho , Joel R. Phillips , L. Miguel Silveira, "Passive Constrained Rational Approximation Algorithm using Nevanlinna-Pick Interpolation," *Proceedings of the conference on Design, automation and test in Europe*, p. 923, 2002.
- [45] G. Antonini, A. Scogna, A. Orlandi, C. Ritota, and A. Duffy, *Applications of FSV to EMC and SI data*, IEEE International Symposium on EMC, Chicago, August 2005.
- [46] H. Chen, Q. Lin, L. Tsang, C.-C. Huang, and V. Jandhyala, "Analysis of a large number of vias and differential signaling in multilayered structures," *IEEE Trans. Microwave Theory Tech.*, vol. 51, no. 3, pp. 818-829, Mar. 2003.



- [47] L. Tsang, and D. Miller, "Coupling of vias in electronic packaging and printed circuit board structures with finite ground plane," *IEEE Trans. Adv. Packag.*, vol. 26, no. 4, pp. 375-384, Nov. 2003
- [48] X. Gu and M. B. Ritter, "Application of Foldy-Lax Multiple Scattering Method To Via Analysis in Multi-layered Printed Circuit Board," *DesignCon 2008*, Santa Clara, CA USA, Feb. 4 - Feb. 7, 2008.
- [49] C. Schuster, Y. Kwark, G. Selli, and P. Muthana, "Developing a 'Physical' Model for Vias," *DesignCon 2006*, Santa Clara, CA USA, Feb.6-9, 2006.
- [50] G. Selli, C. Schuster, and Y. Kwark, M. B. Ritter, and J. Drewniak, "Developing a Physical Via Model for Vias – Part II: Coupled and Ground Return Vias," *DesignCon 2007*, Santa Clara, CA USA, Jan.29-Feb 1, 2007.
- [51] G. Selli, C. Schuster, Y. Kwark, J. Drewniak, "Model-to-Hardware Correlation of Physics Based Via Models With the Parallel Plate Impedance Included," *IEEE Symposium on Electromagnetic Compatibility*, Portland, OR, USA, August 2006.
- [52] A Duffy, A Martin, G Antonini, A Orlandi and C Ritota, "The feature selective validation (FSV) method," in *Proc. of IEEE 2005 EMC Int Symp*, Chicago, USA, 8-12 August, 2005.
- [53] A. Martin (1999) "Feature Selective Validation," Thesis for Doctor of Philosophy. De Montfort University, Leicester.
- [54] Y. Rahmat-Samii and E. Michielssen, *Electromagnetic Optimization by Genetic Algorithms*. New York: Wiley, 1999, pp. 1–93.

## VITA

Siming Pan was born on April 8<sup>th</sup>, 1986 in Lanzhou, China. In August 2008, he obtained his Bachelor's Degree from Tsinghua University in Electrical Engineering, Beijing, China.

In August 2008, he enrolled at the Missouri University of Science and Technology to pursue his Master's Degree in Electrical Engineering, during which time he was a graduate research assistant in Electromagnetic Compatibility Laboratory. From October 2009 to January 2010, and from May 2010 to August 2010, he did internships at Cisco Systems., San Jose, California. He received President's Memorial Award from IEEE Electromagnetic Compatibility Society in 2009. He received his Master's Degree in December 2010.